Cold Trapped Positrons and Progress to Cold Antihydrogen

by

John Karl Estrada

Submitted to the Department of Physics
in partial fulfillment of the requirements for the degree of

Doctor of Philosophy

at the

MASSACHUSETTS INSTITUTE OF TECHNOLOGY

January 2002

Author .....
Department of Physics
January 31, 2002

Certified by .....
Gerald Gabrielse
Professor of Physics, Harvard University
Thesis Supervisor

Certified by .....
Daniel Kleppner
Lester Wolfe Professor of Physics
Thesis Supervisor

Accepted by .....
Thomas J. Greytak
Chairman, Department of Physics Graduate Committee

Cold Trapped Positrons and Progress to Cold Antihydrogen

by

John Karl Estrada

Submitted to the Department of Physics
on January 31, 2002, in partial fulfillment of the
requirements for the degree of
Doctor of Philosophy

Abstract

A new physical mechanism for positron accumulation is explained and demonstrated. Strongly magnetized Rydberg positronium is formed and then ionized, allowing us to trap equal numbers of either positrons or electrons over a wide range of conditions. Antiprotons are trapped, cooled, and stacked from the new Antiproton Decelerator facility for the first time. Combining positrons and antiprotons, we have demonstrated the first positron cooling of antiprotons. The cooling takes place in a 4.2 K, nested Penning trap where conditions are ideal for the eventual goal of the formation of antihydrogen.

Thesis Supervisor: Gerald Gabrielse
Title: Professor of Physics, Harvard University

Thesis Supervisor: Daniel Kleppner
Title: Lester Wolfe Professor of Physics

Acknowledgments

I am grateful to have worked on an exciting and interesting research project. At Harvard, I was responsible for understanding the new positronium approach to positron accumulation and using this knowledge to scale up the positron loading rate. Later at CERN, I worked on getting the software and support hardware in place to trap antiprotons and positrons in a single apparatus. I would not have been succesful at this task, without the help and support of many people.

My adviser, Gerald Gabrielse, deserves special thanks for having an interesting project ready for me to join. Gerry has been a great mentor and was never too busy to answer a question. I hope for the sake of future students that his ability to work all-nighters at CERN will diminish, but I doubt it will happen.

Joining a lab before having much experience, I have been fortunate to work alongside graduate students with the patience to explain the finer details of experimental physics. David Hall left me an experimental apparatus that I was fortunate not to have to build myself. He was also responsible for the initial data for the positronium experiment. Peter Yesley was the master builder who took requests like, "and lets stick a moderator on there too!" and made them a reality. In addition to having a large role in every apparatus I ever laid my hands on, he made the work environment into a better place. Timothy Roach, Joseph Tan, and Cody Storry were all postdocs with whom I had the joy of working. All three were always around to answer questions and help keep me motivated. I hope their futures are as promising as they deserve. Working with Joseph during almost four years, I have seen his skill in making things work. His work in keeping the positron and antihydrogen experiments has many experimental failures only a memory. With Joseph's skill, he actually made getting a fiber optic into the trap enclosure seem easy.

Working on other experiments in the lab, I enjoyed working with Steve Peil, Lisa Lapidus, Carla Levy, Brian Odom, and Brian D'Urso. This group helped me integrate myself into the lab environment both in a science and social perspective. Graduate students starting after I was in the lab have helped me also. Paul Oxley helped with the positron experiment, Nathaniel Bowden made the CERN blockhouse a reality, and Melissa Wessels built numerous electronics to our delight.

As part of the larger ATRAP collaboration, I would like to thank the various groups with whom I was fortunate to interact during my time at CERN. Walter Oelert, Georg Schepers, and Dieter Grzonka kept the annihilation detectors running and taught me enough about their operation that I may know a bit. Hannes Zmeskal, Hermann Fuhrmann, and Rupert Ursin got the PPAC running and let me watch. Hartmut Kalinowsky, Cees Wesdorp, and Joechen Walz were always ready to give a hand and help out, even if they were working on the own projects.

Contents

List of Figures

List of Tables

Chapter 1

Introduction

This work reports on the progress made in the accumulation of cold positrons, antiprotons, and their interactions. This chapter lists the advances made and the motivation for this work. The following chapter presents a brief explanation of Penning traps for the new reader. In chapter three, we discuss the methods for particle (and antiparticle) detection. Chapter four explains the mechanism for trapping positrons via positronium. Chapter five shows the progress with antiproton trapping at a new facility. Chapter six contains the experiments done combining cold trapped positrons and antiprotons.

A new physical mechanism for the accumulation of cold (4.2 K) positrons, orders of magnitude more efficient than previous methods, is explained and demonstrated [1]. Highly excited positronium is formed as positrons pass through a moderating tungsten crystal in a high magnetic field. This positronium is ionized by the electric field of a trapping well, which accumulates either positrons or electrons, depending on the polarity of the well. The accumulation of positrons by this method has been previously postulated [2]. The clear symmetry we observed between positron and electron accumulation established the central role of strongly magnetized Rydberg positronium.

An understanding of the positron accumulation process allowed us to make two improvements to the absolute loading rate. First, we incorporated a second moderating tungsten crystal. This dual-moderator technique improved the rate by 250%. The use of two moderators also allowed us to study the energy distribution of moderated positrons. The second gain in accumulation rate was achieved through the installation of a new 150 mCi ^{22}Na source replacing the 2.5 mCi source used during beginning studies. The maximum rate now observed, benefiting from both improvements, is more than 1000 times greater than the previous electronic dampening method.

We have also demonstrated the crucial role of adsorbed gas on the surface of the thin transmission moderator. The inadvertent removal of this gas layer occurred when cold positrons and antiprotons were first made to interact [2]. The role of this gas layer in the formation of positronium remains to be understood. Further work in this area may result in improved rates, if the properties of the gas layer are optimized for positronium production.

To protect this adsorbed gas layer, we installed a rotary electrode into the 4.2 K, 6

T, vacuum environment of the Penning trap. This electrode separates the antiproton and positron trapping regions, keeping the antiprotons from acting on the moderators. Extended use of this rotary electrode has shown that we are now able to protect the adsorbed layer.

As part of the ATRAP collaboration, we have trapped, cooled, and stacked antiprotons from CERN's new Antiproton Decelerator (AD) for the first time. This work built upon the techniques developed by the TRAP collaboration which pioneered antiproton trapping [3, 4, 5, 2]. Bunched 5 MeV antiprotons are ejected from the AD. Using energy degraders, we reduce a fraction of the antiprotons to under 3 keV. These antiprotons are captured in our Penning trap and cooled via collisions with electrons to sub-eV energies. We trap and combine antiprotons from multiple ejections, increasing the total number accumulated.

Antiproton trapping occurs in a new Penning trap [6] designed to accumulate positrons and antiprotons. This trap is capable of capturing positrons and antiprotons in a single, cryogenic, vacuum space. The 35 electrode Penning trap has incorporated two positron-moderating crystals, a field emission point (FEP) for electron production, and an energy degrader for antiproton trapping. As this trap is able to simultaneously trap positrons and antiprotons, we were able to experiment with the particles together.

Our most interesting use of our trapped antiprotons and positrons has been the demonstration of the first positron cooling of antiprotons [7]. While we have not yet observed a clear signature of cold antihydrogen, we have demonstrated the feasibility of accumulating and manipulating the cold positrons and antiprotons that are required.

Looking forward to this long-term goal of antihydrogen production, we have initially investigated two recombination techniques. The first technique, three-body recombination, has been theoretically investigated by others [8, 9] with more recent work investigating rates in high magnetic fields [10, 11, 12]. The second technique, pulsed field recombination, has been demonstrated with rubidium [13]. This scheme incorporates pulsed electric fields ($\nu \sim 0.1$ GHz) to trap the positron inside the Coulomb potential of the antiproton.

The eventual goal of this work is the formation of cold, trapped, antihydrogen atoms. Antihydrogen has already been made in high-energy experiments [14, 15], but would be interesting if done in an environment suitable for precision measurements. Cold trapped antihydrogen would allow for many types of experiments not available antihydrogen at high energies. Two experiments involving tests of fundamental physics are the possibility of CPT violation [16] and verifying the weak equivalence principal in neutral antimatter [17].

Historically discrete symmetry invariance began with parity conservation. The parity operator (P) inverts the coordinate system producing a mirror image of the original axis. For many years physicists had believed that the laws of physics are the same in a parity inverted space. In 1956 Lee and Yang pointed out [18], "for the weak interaction ... parity conservation is so far only an extrapolated hypothesis unsupported by experimental evidence" and then suggested possible experiments which would determine if parity is a conserved quantity in beta decay. An experiment was

soon carried out to test this hypothesis.

A sample of ^{60}Co was placed in a magnetic field and cooled, aligning the nuclear spins. Electrons are emitted as ^{60}Co decays. The parity complement experiment has the nuclear spins aligned in the opposite direction, but with the original distribution of electrons. If parity is conserved, then the electron distribution should be equal in both the direction aligned and the direction anti-aligned to the nuclear spin. In Wu's experiment [19], there was a non-symmetric distribution. This result showed that parity was not conserved in this system.

Replacing the parity conservation theory, Landau proposed that the combination of P and C might indeed be conserved [20]. C, the charge conjugation operator, exchanges a particle with its antiparticle. The combined charge conjugation and parity operators would act to change a particle to its antiparticle and change the sign of its coordinates. The hope was that nature followed the same physical laws on systems and their CP counterparts.

In 1964 Cronin and Fitch investigated the decay of K_2. K_2 is an eigenstate of CP with eigenvalue -1. Their apparatus was designed to look for transitions of K_2 into two pions. As the two pion state is also an eigenstate of CP but with eigenvalue +1, this should be a forbidden transition. To the surprise of many, observed transitions to the "forbidden" state [21] showed that CP is not an invariant.

Currently it is believed that CPT, where T represents time reversal, is an invariant. As finding a CPT violation would require new physics, it is difficult to speculate on the possible size of expected violations. CPT conservation requires that hydrogen and antihydrogen should have the same energy levels and therefore any difference would be important.

In addition to interesting internal energy levels, the gravitational properties of antihydrogen will be interesting to study. Einstein's theory of general relativity rests on the assumption that gravitational and inertial masses are equivalent. After many years of tests this assumption seems to hold true. Physicists, who generally look for the simplest set of laws possible, often believe that this should hold true both for matter (which has been experimentally verified) and for antimatter (for which this has never been experimentally verified in a direct manner.) Since this test only requires antimatter of some form, it might seem easier with a collection of elementary particles, e.g. positrons. Unfortunately doing gravitational measurements on charged particles is extremely difficult due to the ratio of gravitational to electric field strength. A review of the problems in performing gravitational measurements on charged particles [22] has been done and points to the extreme difficulties with controlling "small" electrical effects which can mask gravitational effects. It is with this in mind that antimatter gravity experiments seem more likely to produce meaningful results with neutral samples. There remain difficulties [17] to overcome, yet the possibility to perform these experiments still exists.

Although our long-term goals still hold many interesting and difficulties to overcome, the short-term goal of cold antihydrogen seems attainable on a short-time scale. Positrons, accumulated at a high rate using the interesting new method, are trapped simultaneously with antiprotons in a new apparatus. As both particles are accumulated in a single space, their manipulations is simple and holds no new difficulties.

The ingredients of cold antihydrogen are now available and able to be combined. Hopefully, signals from cold antihydrogen will be observed soon and spectroscopy on these atoms will follow.

Chapter 2

Penning trap

A Penning trap is a particular combination of electric and magnetic fields which provides the ability to trap charged particles. The range of both particle number and type held in a Penning trap is amazingly large. As these traps use electromagnetic fields for containment, they have the ability to hold antimatter particles which annihilate when held with others methods. Antiprotons have even been trapped for two months without loss [23]. Examples of trapped species include a single electron [24] and 6×10^5 antiprotons [2].

This chapter will present an overview of the Penning trap including the electrostatics involved, particle motion, and relevant energy levels. A more complete presentation upon which this work is heavily based can be found elsewhere [25].

2.1 Electrostatics in a Penning trap

An ideal Penning trap consists of a electrostatic quadrupole potential aligned in a homogeneous magnetic field. A mathematical representation of the fields is

$$V = \frac{V_o}{2}\left(\frac{r}{d}\right)^2 \mathrm{P}_2(\cos\theta) \tag{2.1}$$

$$\boldsymbol{B} = B_o\hat{\boldsymbol{k}} \tag{2.2}$$

where $\mathrm{P}_n(x)$ is the Legendre polynomial of order n, and d is a so far undefined characteristic length.

The magnetic field can be produced with a solenoid of such dimensions as to provide an adequate interior volume and acceptable homogeneity. One way to generate the quadrupole potential is with electrodes having surfaces which are hyperboles of revolution. Figure 2-1 shows a section of a hyperbolic trap with truncated electrodes. Extra compensation electrodes [26] are often introduced in the gaps between the ring and endcap electrodes. Hyperbolic electrodes benefit from the uniformity of the quadrupole potential. Perfect hyperbolic electrodes produce the potential given in (2.1) anywhere within the electrodes. Since Penning trap experiments often need access for particles or light, other geometries have been investigated of which the

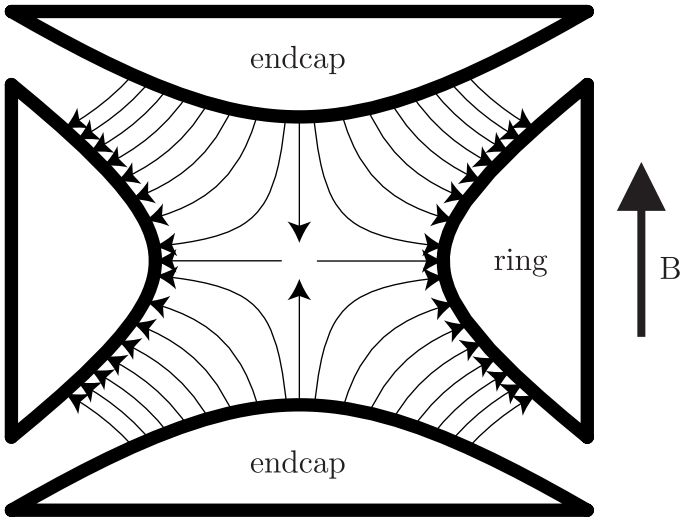

Figure 2-1: Electric field lines in a hyperbolic Penning trap with truncated electrodes.

open-access cylindrical trap [27] is an example. This trap is built with coaxial cylindrical electrodes. Although this type of trap does not produce a pure quadrupole potential over as large a volume, the electrode dimensions are chosen to produce a near quadrupole field within the center of the trap.

Although all work done in this thesis used open-access cylindrical traps, it is instructive to first work out the electrostatics of the hyperbolic trap. In this way one can see the perturbations to the field in using an open-access cylindrical trap.

2.1.1 Hyperbolic trap

A hyperbolic trap has electrodes which follow one of two equations. The inner surface of the ring electrode obeys

$$r^2 \, \mathrm{P}_2(\cos\theta) = -\rho_o^2/2 \tag{2.3}$$

while the endcap electrodes follow

$$r^2 \, \mathrm{P}_2(\cos\theta) = z_o^2 \tag{2.4}$$

with ρ_o and z_o being the shortest distances from the center to the electrodes in the radial and axial directions, respectively.

If the electrodes are biased such that $V_{ring} = -V_o$ and $V_{endcap} = 0$, which would trap positive particles when $V_o > 0$, then the electrostatic potential inside the trap

can be solved as a boundary value problem satisfying the following

$$V(r,\theta) = \begin{cases} -V_o & r^2\,\mathrm{P}_2(\cos\theta) = -\rho_o^2/2 \\ 0 & r^2\,\mathrm{P}_2(\cos\theta) = z_o^2 \end{cases} \tag{2.5}$$

The general solution in spherical coordinates, neglecting terms which do not converge at the origin, are antisymmetric in z, or have azimuthal dependence, is

$$\Phi = \frac{\Phi_o}{2}\sum_{k=0}^{\infty} C_{2k}\left(\frac{r}{d}\right)^{2k} P_{2k}(\cos\theta) \tag{2.6}$$

Applying this general solution to the given boundary conditions gives

$$C_0 = -\frac{z_o^2}{d^2} \tag{2.7}$$

$$C_2 = 1 \tag{2.8}$$

$$C_{i>2} = 0 \tag{2.9}$$

with the following definitions

$$d^2 \equiv \frac{1}{2}(z_o^2 + \rho_o^2/2) \tag{2.10}$$

$$\Phi_o \equiv V_o \tag{2.11}$$

Since the constant term does not trap, the trapping potential within the electrodes can be rewritten as

$$V_{trap} = \frac{V_o}{2}\left(\frac{r}{d}\right)^2 \mathrm{P}_2(\cos\theta) \tag{2.12}$$

which is identical to (2.1) showing that hyperbolic electrodes can be used to generate the electrostatic field of a Penning trap. (As the constant term of the potential effects the trap operation, for example when loading the trap, it can not be generally ignored.)

2.1.2 Three electrode cylindrical trap

Now that a hyperbolic trap has been presented the next step is the three electrode cylindrical trap. Because there are less degrees of freedom than that of a five electrode cylindrical trap this trap is simpler to intuitively understand. Also, all mathematical results of this trap can be used in the five electrode case after being suitably rescaled. A three electrode cylindrical trap can be seen in Fig. 2-2. One should note that this trap as drawn is in fact not an open-access trap. The reason for the inclusion of end-plates has been to simplify the mathematics and it will be shown that near the center of the trap the movement of these plates will not drastically affect the results.

Biasing this trap with the same values as that of the hyperbolic trap, $V_{ring} = -V_o$

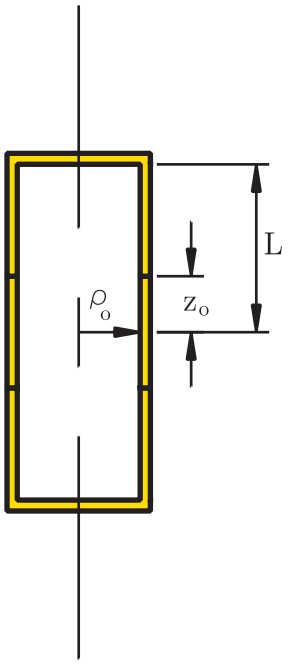

Figure 2-2: Cross section of a cylindrical three electrode Penning trap

and $V_{endcap} = 0$, gives the following boundary conditions

$$V(\rho = \rho_o) = \begin{cases} -V_o & |z| < z_o \\ 0 & |z| > z_o \end{cases} \tag{2.13}$$

and

$$V(z = \pm L) = 0 \tag{2.14}$$

Since the boundary conditions are naturally expressed in cylindrical coordinates this trapping configuration will be solved using them. The general expansion of the electrostatic potential in cylindrical coordinates, neglecting terms which diverge at the origin, are antisymmetric in z, or have an azimuthal dependence, is

$$\Phi = \Phi_o \sum_{n=0}^{\infty} A_n I_0(k_n \rho) \cos(k_n z) \tag{2.15}$$

where I_n is the modified Bessel function of the first kind of order n. Using the given boundary conditions gives the following expansion [28]

$$A_n = -\frac{2}{k_n L} \frac{\sin(k_n z_o)}{I_0(k_n \rho_o)} \tag{2.16}$$

	$L_{endcap} = 2z_o$	$L_{endcap} = 4z_o$	$L_{endcap} = 20z_o$
C_2	0.5736	0.5734	0.5734
C_4	0.01356	0.01350	0.01350
C_6	-0.04858	-0.04859	-0.04859
$\rho_o = .6$cm		$z_o = .512$cm	

Table 2.1: C_k values for various endcap lengths in 3 electrode cylindrical trap

with

$$k_n = \frac{(n + \frac{1}{2})\pi}{L} \tag{2.17}$$

with $2L$ as the total axial length of the trap. Writing out the potential for completeness gives

$$V = V_o \sum_{n=0}^{\infty} \frac{2}{k_n L} \frac{\sin(k_n z_o)}{I_0(k_n \rho_o)} I_0(k_n \rho) \cos(k_n z) \tag{2.18}$$

To convert this series into spherical coordinates one simply has to equate this series with the general expansion (2.6) along the z-axis near the trap center.

$$\frac{1}{2} \sum_{k=0}^{\infty} C_{2k} \left(\frac{z}{d}\right)^{2k} = \sum_{n=0}^{\infty} A_n I_0(k_n \rho) \cos(k_n z) \tag{2.19}$$

Rewriting the cos term as a power series and using the fact that $I_0(0) = 1$ gives

$$\frac{1}{2} \sum_{k=0}^{\infty} C_{2k} \left(\frac{z}{d}\right)^{2k} = \sum_{n=0}^{\infty} A_n \sum_{m=0}^{\infty} \frac{(-1)^m (k_n z)^{2m}}{(2m)!} \tag{2.20}$$

In order for each of these series to be equal, each term in z must be separately equal.

$$C_{2k} = 2 \frac{(-1)^k}{(2k)!} \sum_{n=0}^{\infty} (k_n d)^{2k} A_n \tag{2.21}$$

Since $\frac{r}{d} \ll 1$ for particles in thermal equilibrium, only the leading C_n's will affect the results. A table of the leading C_n values for different lengths of endcaps is shown in Table 2.1.

2.1.3 Five electrode cylindrical trap

Ideal open-access traps should be designed to duplicate the pure quadrupole electrostatic field of the hyperbolic trap inside the region of interest as closely as possible. Open-access traps can be made with as little as three electrodes similar to the hyperbolic traps but five electrode traps have the ability to tune out the leading term of the non-quadrupole expansion. The geometry of a five electrode or compensated

open access trap can be seen in Fig. 2-3.

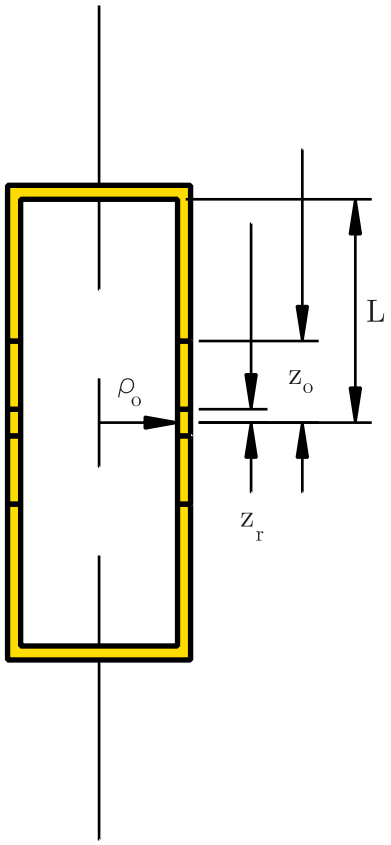

Figure 2-3: Cross section of a cylindrical five electrode Penning trap

The set of boundary conditions for this trap is given as

$$V_1(\rho = \rho_o) = \begin{cases} V_o - V_c & |z| < z_r \\ 0 & |z| > z_r \end{cases} \tag{2.22}$$

$$V_2(\rho = \rho_o) = \begin{cases} V_c & |z| < z_o \\ 0 & |z| > z_o \end{cases} \tag{2.23}$$

where

$$V = V_1 + V_2 \tag{2.24}$$

In order to reuse the results from the previous subsection, the potential will be defined as

$$\Phi = \Phi_1 + \Phi_2 \tag{2.25}$$

with

$$\Phi_1 = \Phi_o^{(1)} \sum_{n=0}^{\infty} A_n^{(1)} I_0(k_n \rho) \cos(k_n z) \tag{2.26}$$

	$L_{endcap} = z_e$	$L_{endcap} = 2z_e$	$L_{endcap} = 10z_e$
C_2	0.5450	0.5448	0.5448
C_4	-0.00001265	-0.00007030	-0.00007031
C_6	-0.0003413	-0.0003494	-0.0003494
$z_r = .096\,\text{cm}$ $z_o = .585\,\text{cm}$ $z_e = 1.016\,\text{cm}$			
$\rho_o = .600\,\text{cm}$ $V_c/V_o = .8810$			

Table 2.2: C_k values for various endcap lengths in 5 electrode cylindrical trap

$$\Phi_2 = \Phi_o^{(2)} \sum_{n=0}^{\infty} A_n^{(2)} I_0(k_n \rho) \cos(k_n z) \tag{2.27}$$

The solution is trivially seen to be

$$A_n^{(1)} = \frac{2}{k_n L} \frac{\sin(k_n z_r)}{I_0(k_n \rho_o)} \tag{2.28}$$

$$A_n^{(2)} = \frac{2}{k_n L} \frac{\sin(k_n z_o)}{I_0(k_n \rho_o)} \tag{2.29}$$

$$k_n = \frac{(n + \frac{1}{2})\pi}{L} \tag{2.30}$$

Again the potential will be included for completeness

$$V = \sum_{n=0}^{\infty} \frac{2}{k_n L} \frac{I_0(k_n \rho) \cos(k_n z)}{I_0(k_n \rho_o)} \left[(V_o - V_c) \sin(k_n z_r) + V_c \sin(k_n z_o) \right] \tag{2.31}$$

Transforming this representation to spherical coordinates gives

$$C_{2k} = 2 \frac{(-1)^k}{(2k)!} \sum_{n=0}^{\infty} (k_n d)^{2k} \left[\left(\frac{V_o - V_c}{V_o} \right) A_n^1 + \left(\frac{V_c}{V_o} \right) A_n^2 \right] \tag{2.32}$$

The numerical values are given in Table 2.2

Since the potential of this trap is dominated by the quadrupole term it will be rewritten as

$$V = \frac{C_2 V_o}{2} \left(\frac{r}{d} \right)^2 \mathrm{P}_2(\cos\theta) \tag{2.33}$$

where it is clearly seen that this trap produces the same type of potential as an ideal Penning trap but rescaled by a numerical factor C_2.

2.2 Electrostatic solution of a charged particle in a Penning trap

In order to complete the electrostatic solutions of the ideal Penning trap the problem of a charged particle in the trap will now be solved, see Fig. 2-4. For simplicity the limit of infinite endcap electrodes will be used here. Although this differs in reality since finite endcap electrodes must be used the error will be seen to be small since the potential drops off exponentially in the axial direction.

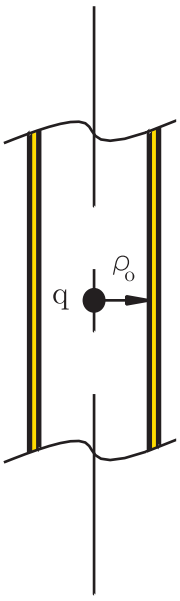

Figure 2-4: Point charge in a infinite conducting cylinder.

This calculation follows previous work [25, 28] where the amount of charge induced on an electrode by a trapped particle is computed. It will be shown that this approach agrees with the previous solution.

Because of the different boundary conditions of this problem the electrostatic potential will be expanded as follows

$$\Phi_{z>0} = \Phi_o \sum_{n=1}^{\infty} A_n J_0(k_n \rho) e^{-k_n z} \tag{2.34}$$

$$\Phi_{z<0} = \Phi_o \sum_{n=1}^{\infty} A_n J_0(k_n \rho) e^{k_n z} \tag{2.35}$$

Crossing over a layer of charge the potential is a continuous function but not its first derivative. The potentials given are continuous as required and have derivatives

which must satisfy

$$\frac{q\delta(\rho)}{\epsilon_o} = \left[\frac{\partial\Phi_{\rm II}}{\partial z} - \frac{\partial\Phi_{\rm I}}{\partial z}\right]_{z=0} \tag{2.36}$$

where $\delta(\rho)$ is the 2-d delta function defined as

$$2\pi\int_0^{\rho_o}\delta(\rho)\rho\,d\rho = 1 \tag{2.37}$$

The solution of this problem is shown in Panofsky [29] and is

$$A_n = \frac{2/(k_n\rho_o)}{J_1^2(k_n\rho_o)} \tag{2.38}$$

with

$$\Phi_o = \frac{q}{4\pi\epsilon_o\rho_o} \tag{2.39}$$

and $k_n\rho_o$ being the n^{th} zero of the Bessel function.

The induced surface charge density on the cylinder is

$$\sigma(z) = -\left[\frac{\partial\Phi}{\partial\rho}\right]_{\rho=\rho_o} \tag{2.40}$$

which becomes

$$\sigma(z) = -\sigma_o\sum_{n=1}^{\infty}\frac{e^{\pm k_n z}}{J_1(k_n\rho_o)} \tag{2.41}$$

with

$$\sigma_o = \frac{q}{2\pi\rho_o^2} \tag{2.42}$$

Performing the trivial integral over the azimuthal angle gives the linear charge density as

$$\lambda(z) = -\frac{q}{\rho_o}\sum_{n=1}^{\infty}\frac{e^{\pm k_n z}}{J_1(k_n\rho_o)} \tag{2.43}$$

which is shown in Fig. 2-5.

To determine the signal induced on an arbitrary electrode, one integrates over that electrode to find the total charge induced. The axial motion of a particle is monitored via a compensation electrode therefore the induced charge produced by a particle of charge q at the origin is

$$Q_{comp} = -\frac{q}{\rho_o}\int_{z_r}^{z_o}\sum_{n=1}^{\infty}\frac{e^{\pm k_n z}}{J_1(k_n\rho_o)}dz \tag{2.44}$$

Performing the integral gives

$$Q_{comp} = -q\sum_{n=1}^{\infty}\frac{e^{-k_n z_r} - e^{-k_n z_o}}{(k_n\rho_o)J_1(k_n\rho_o)} \tag{2.45}$$

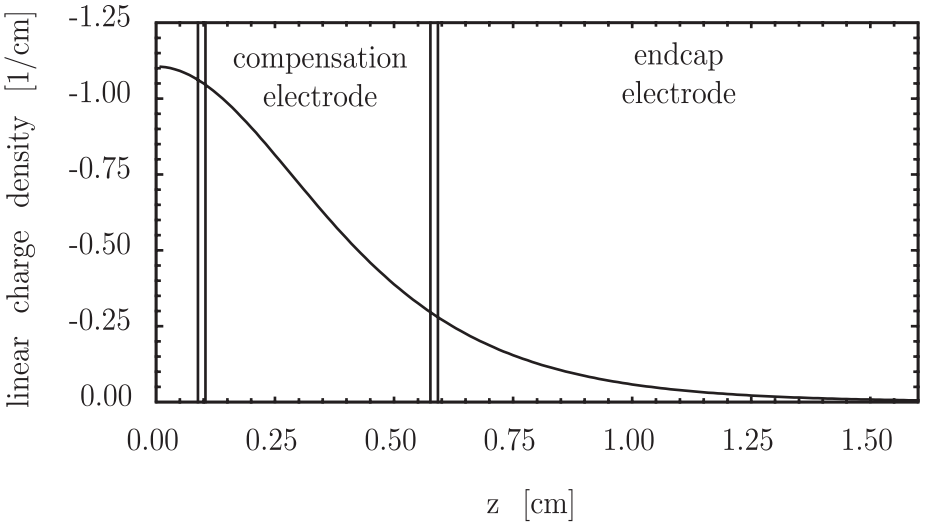

Figure 2-5: Normalized linear charge density along trap

Because the cylindrical cylinder is infinite in length, motion of the particle is equivalent to a change in the limits of integration. Therefore the induced signal of a charge axially displaced z_a from the origin is

$$Q_{comp} = -q \sum_{n=1}^{\infty} \frac{e^{-k_n(z_r - z_a)} - e^{-k_n(z_o - z_a)}}{(k_n \rho_o) J_1(k_n \rho_o)} \tag{2.46}$$

Performing a sum over leading terms and then integrating with the limits taken as the charge oscillates in the axial direction gives the following signal per unit charge

$$Q_{comp} = -0.32 - 0.767 \left(\frac{z_a}{\text{cm}} \right) \tag{2.47}$$

for small oscillations, $k_0 z_a \ll 1$.

As the position dependent term will be used in following sections it will be labeled as

$$\kappa = \frac{dQ_{comp}}{dz_a} = -.767\,\text{cm}^{-1} \tag{2.48}$$

As stated earlier κ can be related to an equal quantity from previous work [25, 28] with the two related via

$$\kappa = -\frac{d_1}{2z_o} \tag{2.49}$$

For five electrode traps of the type considered $d_1 = 0.8994$ and $z_o = 0.586\,\text{cm}$ giving $\kappa = -0.767\,\text{cm}^{-1}$ in agreement to the results of this approach.

Assuming that the charge is that of a single positron with axial oscillation fre-

quency of $f = 28\,\mathrm{MHz}$ and amplitude $z = 60\,\mu\mathrm{m}$, gives the RF signal

$$I_{comp} = \omega e \kappa z \cos(\omega t) = 130 \cos(\omega t)\,\mathrm{fA} \tag{2.50}$$

2.3 Particle in E and B fields

Classically, a charged particle in a uniform magnetic field will execute circular motion in a plane perpendicular to the magnetic field. This motion is known as cyclotron motion and has a frequency

$$\omega_c = \frac{\mid eB \mid}{m} \tag{2.51}$$

Defining the direction of the magnetic field to be the positive z direction it is seen that the particle is bound in the x-y plane in its circular motion. A Penning trap superimposes an electric field onto this magnetic field, trapping the particle in three dimensions. The potential of the electric field is

$$V = C_2 V_o \frac{z^2 - \rho^2/2}{2d^2} \tag{2.52}$$

where $C_2 = 1$ for hyperbolic traps and is listed in Tables 2.1 and 2.2 for other geometries. Since the magnetic field does not affect the motion of the particle along its axis, the particle's axial motion is determined by the z component of the electric field whose force is

$$F_z = \frac{eC_2V_o}{d^2} z \tag{2.53}$$

This is clearly seen to be the force producing simple harmonic motion. Solving for the motion of the particle shows its fundamental frequency to be

$$\omega_z = \sqrt{\frac{eC_2V_o}{md^2}} \tag{2.54}$$

Since the electric field must have a zero divergence the axial component of this field brings with it a radial part. Writing the radial portion of the Lorenz force equation with $\boldsymbol{\rho}$ denoting the 2-d radial position vector and $\hat{\boldsymbol{k}}$ representing the axial unit vector

$$\boldsymbol{F}_{2d}(\boldsymbol{\rho}) = \frac{eV_o}{2d^2}\boldsymbol{\rho} + eB_o(\dot{\boldsymbol{\rho}} \times \hat{\boldsymbol{k}}) \tag{2.55}$$

Using Newton's equation to determine the particles motion gives upon substitution of axial and cyclotron frequencies

$$\ddot{\boldsymbol{\rho}} - \omega_c \dot{\boldsymbol{\rho}} \times \hat{\boldsymbol{z}} - \frac{\omega_z^2}{2}\boldsymbol{\rho} = 0 \tag{2.56}$$

This second order differential equation exhibits the contributions of two effects. The term with ω_c is from the particles cyclotron motion and the term with ω_z is from the electric field. From the azimuthal symmetry one might propose a circular motion of

	e	P
f_{mag}[Hz]	2.65k	17.5k
f_{axial}[Hz]	28.3M	1.70M
$f_{cyclotron}$[Hz]	151G	82.4M
V_o[V]	8.8	52.0
B_o[T]	5.4	5.4

Table 2.3: Typical particle frequencies.

the following form

$$\boldsymbol{\rho}(t) = \boldsymbol{\rho}_1(t) + \boldsymbol{\rho}_2(t) \tag{2.57}$$

with the individual motions being given as

$$\boldsymbol{\rho}_n(t) = \rho_n \sin(\omega_n t)\hat{\boldsymbol{x}} + \rho_n \cos(\omega_n t)\hat{\boldsymbol{y}} \tag{2.58}$$

Upon substituting $\vec{\boldsymbol{\rho}}(t)$ into the equation of motion one finds

$$\omega_{1,2} = \frac{1}{2}\left(\omega_c \pm \sqrt{\omega_c^2 - 2\omega_z^2}\right) \tag{2.59}$$

In the case that $\omega_c^2 \gg 2\omega_z^2$, which is the normal experimental case, the above frequencies can be approximated by the more simple

$$\omega_m = \frac{\omega_z^2}{2\omega_c} \tag{2.60}$$

$$\omega_{c'} = \omega_c - \omega_m \tag{2.61}$$

where the frequencies are now labeled ω_m to represent the magnetron frequency and $\omega_{c'}$ for the modified cyclotron frequency.

With the characteristic frequencies now defined and the individual motions described one can see how the particle moves within the fields. From the above treatment one can see that the particle's motion is a sum of three motions each with their own characteristic time scales. The sum motion is fast, $\omega_{c'}^{-1}$ and slow, ω_m^{-1}, radial circular motions imposed on a moderate, ω_z^{-1}, oscillatory axial motion which can be seen in Fig. 2-6. Typical frequencies are shown in Table 2.3, with $f = \omega/2\pi$.

2.4 Energy levels and decay rates

Now that the particle's motion has been investigated, the energy of the particle can be determined. The total non-relativistic energy of a particle is given by

$$E = \frac{1}{2}mv^2 + e\Phi \tag{2.62}$$

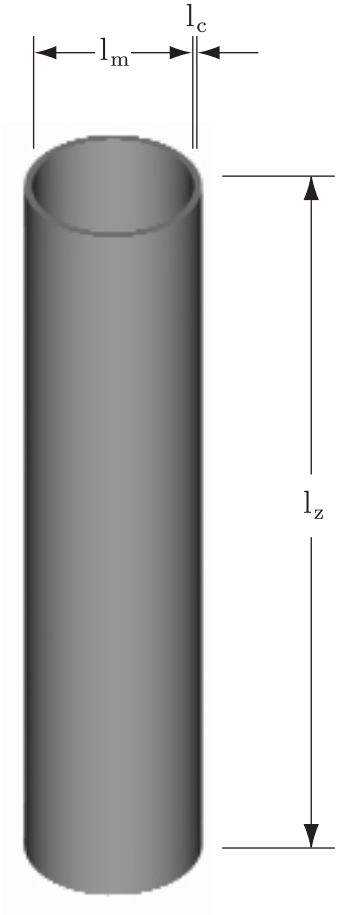

Figure 2-6: The volume space of the motion of a single positron in the Penning trap. The cylinder is dimensioned to represent the three characteristic motions (axial, magnetron, and cyclotron) with the axial dimension reduced by a factor of 20.

	e			P		
	magnetron	axial	cyclotron	magnetron	axial	cyclotron
E[μeV]	-0.034	360	360	-3.7	360	360
n	3100	3100	.076	51000	51000	1000
$l_o[\mu\text{m}]$	0.87	63	0.012	0.34	24	0.50
v/c	4.8×10^{-11}	3.7×10^{-5}	3.7×10^{-5}	1.2×10^{-7}	8.6×10^{-7}	8.6×10^{-7}

Table 2.4: Equilibrium particle energies and quantum numbers

Solving for the energy of each motion gives

$$E_{cyc} = \frac{1}{2} m \rho_{c'}^2 \left(\omega_{c'}^2 - \frac{\omega_z^2}{2} \right) \simeq \frac{1}{2} m \rho_{c'}^2 \omega_{c'}^2 \tag{2.63}$$

$$E_{ax} = \frac{1}{2} m z_a^2 \omega_z^2 \tag{2.64}$$

$$E_{mag} = \frac{1}{2} m \rho_m^2 \left(\omega_m^2 - \frac{\omega_z^2}{2} \right) \simeq -\frac{1}{2} m \rho_m^2 \frac{\omega_z^2}{2} \tag{2.65}$$

From the exact forms of the energies it is seen that the cyclotron energy is nearly all kinetic, the axial energy oscillates between kinetic and potential, and the magnetron energy almost entirely potential.

It has been shown [25] that when the Penning trap particle dynamics are solved as a quantum system that each motion behaves as a quantum harmonic oscillator with the following energy levels

$$E_c = \hbar \omega_c \left(n_c + \frac{1}{2} \right) \tag{2.66}$$

$$E_z = \hbar \omega_z \left(n_z + \frac{1}{2} \right) \tag{2.67}$$

$$E_m = -\hbar \omega_m \left(n_m + \frac{1}{2} \right) \tag{2.68}$$

Determining the expectation values of the quantum states is trivial when the average energies are known. It will be assumed that both the cyclotron and axial motion are at equilibrium with a 4 K environment and that the magnetron quantum number is the same as that of the axial. The justifications of the assumptions are shown in the following subsections. Table 2.4 shows the expected particle data including amplitude of oscillations and velocities.

	e	P
γ_{mag}^{-1}[s]	6 x 10^{14}	2 x 10^{15}
γ_{axial}^{-1}[s]	5 x 10^{6}	3 x 10^{12}
$\gamma_{cyclotron}^{-1}$[s]	0.2	1 x 10^{9}

Table 2.5: Typical uncoupled radiative decay times for particles

2.4.1 Radiative damping

Particles executing simple harmonic motion radiate their energy [29] as given by

$$\dot{E} = -\frac{e^2 w^2}{6\pi\epsilon_o mc^3} E \tag{2.69}$$

which is exponential decay with time constant

$$\gamma^{-1} = \frac{2\pi e^2 f^2}{3\epsilon_o mc^3} \tag{2.70}$$

Given typical experimental parameters, the decay constants for each of the motions of both positrons and anti-protons are given in Table 2.5. Looking at the decay times it is clear that only positron cyclotron energy will be able to appreciatively radiate without extra coupling. This extra coupling is in fact applied and its application is explained in the following section.

2.4.2 Electronic damping

As has already been shown in a previous section, a charge oscillating in a Penning trap induces currents in the electrodes. By placing a resistive element between two electrodes which are not symmetric in the particles movement, the particle will be able to dissipate power and thus cool. A drawing of the dampening mechanism is shown in Fig. 2-7 with the equivalent electronic circuit shown in Fig. 2-8.

The capacitance shown in Fig. 2-8 is a combination of two different effects. C_1 represents the capacitance between the electrodes. This capacitance is necessary since the induced signal must have a grounded electrode to return the current. The other capacitance C_2 is the unavoidable capacitance which comes from the placement of the inductor, L, at a distance away from the electrode; in practice this is the dominant capacitance.

The equivalent series resistance and inductance come from a single coil. This coil is normally a single metal wire wound on a form although in the case of the antiproton axial dampening coil it is fabricated from a Type-II superconductor to reduce the resistance.

Combining the various passive elements in Fig. 2-8 with C being the sum of C_1

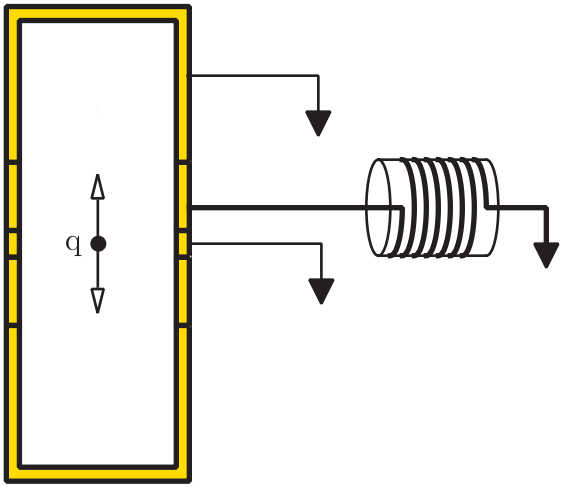

Figure 2-7: Cartoon of the electronic dampening mechanism

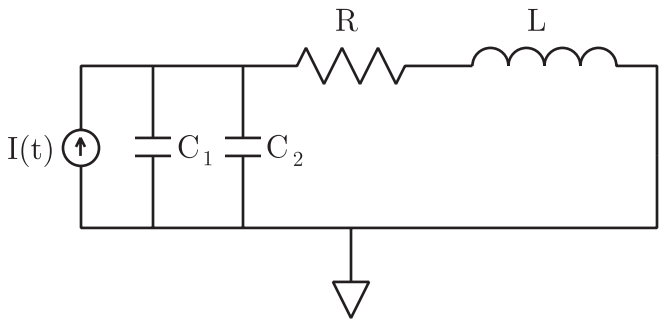

Figure 2-8: Equivalent circuit of electronic dampening mechanism

and C_2 lead to a combined impedance of

$$Z_{eff}(\omega) = \frac{R + i[\omega L(1 - \omega^2 LC) - \omega R^2 C]}{(1 - \omega^2 LC)^2 + (\omega RC)^2} \tag{2.71}$$

which simplifies on resonance, $\omega_o^2 = \frac{1}{LC}$, to

$$Z_{eff}(\omega_o) = \frac{1}{\omega^2 RC^2} - i\frac{1}{\omega C} \tag{2.72}$$

The charge induced on the compensation electrode was shown in Section 2.2 to be of the form (where the constant term has been neglected as it does not contribute to power loss)

$$Q = e\kappa z = e\kappa z_a \cos(\omega_z t) \tag{2.73}$$

Taking the square of the time derivative and averaging over the oscillation period gives

$$I^2 = \frac{e^2\kappa^2 z_a^2 \omega_z^2}{2} \tag{2.74}$$

Solving for z_a and inserting into (2.64) gives

$$E_{ax} = \frac{mI^2}{\kappa^2 e^2} \tag{2.75}$$

As the power lost in the real impedance corresponds to the time derivative of the energy, one may write

$$\dot{E}_{ax} = -I^2 Re[Z_{eff}] = -\frac{I^2}{\omega^2 RC^2} \tag{2.76}$$

Combining the energy and energy loss equations and solving gives

$$E_{ax}(t) = E_o e^{-\gamma_{ed} t} \tag{2.77}$$

with

$$\gamma_{ed} = \frac{\kappa^2 e^2}{m} Q^2 R \tag{2.78}$$

where Q is defined as $Q = \frac{1}{\omega RC}$.

For the positron axial cooling circuit this gives a particle width $\gamma_{ed}/2\pi = 1.6\,\mathrm{Hz}$ and a cooling decay time of $.10\,\mathrm{s}$. For an arbitrary number of particles (2.78) can be written as [28]

$$\gamma_{ed} = N\frac{\kappa^2 e_e^2}{m_e} Q^2 R \tag{2.79}$$

where e_e and m_e are the single electron (positron) charge and mass.

2.4.3 Sideband cooling

The last type of cooling to be discussed is sideband cooling [30]. This technique is most easily viewed in a quantum mechanical framework. As has already been discussed the energy of a particle in a Penning trap can be labeled by three quantum numbers, one for each of the characteristic motions. Table 2.3 shows that the frequencies are well separated from each other which leads to the separation of energy level intervals. Figure 2-9 shows a graphical representation of the axial and magnetron states. In sideband cooling an external drive is applied at the sum frequency of axial

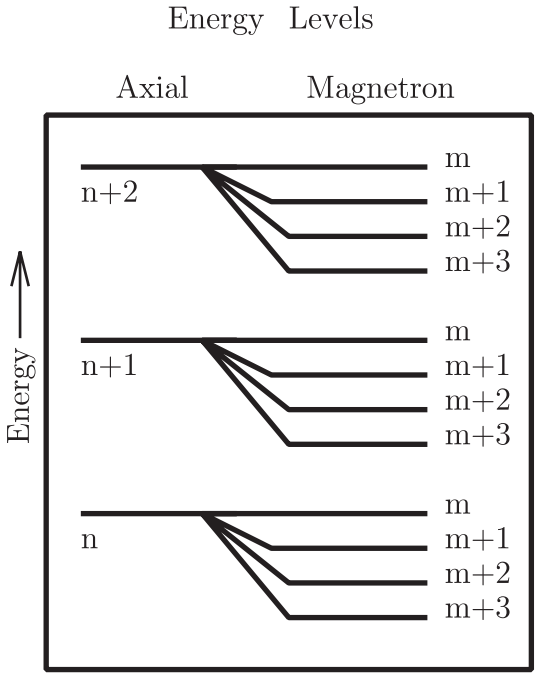

Figure 2-9: Axial and magnetron energy levels for a particle in a Penning trap

and magnetron frequencies. This drive can be expressed as an operator

$$\hat{D} = \hat{a}_z^\dagger \hat{a}_m + \hat{a}_z \hat{a}_m^\dagger \tag{2.80}$$

where $\hat{a}^\dagger$ and $\hat{a}$ are the creation and annihilation operators satisfying

$$\hat{a}^\dagger |n\rangle = \sqrt{n+1}\, |n+1\rangle \tag{2.81}$$

$$\hat{a}|n\rangle = \sqrt{n}\, |n-1\rangle \tag{2.82}$$

To find the transition probabilities to various states one simply computes the expectation value to an arbitrary set of states

$$\langle n_z, n_m|\hat{a}_z^\dagger \hat{a}_m + \hat{a}_z \hat{a}_m^\dagger|n'_z, n'_m\rangle = \begin{cases} \sqrt{n'_m(n'_z+1)} & n_z = n'_z+1, n_m = n'_m-1 \\ \sqrt{n'_z(n'_m+1)} & n_z = n'_z-1, n_m = n'_m+1 \\ 0 & \text{otherwise} \end{cases} \quad (2.83)$$

which shows that the only transitions allowed are those that involve a lowering of the axial state with the raising of the magnetron or the raising of the axial with the the lowering of the magnetron state. If the initial state, $|n'_z, n'_m\rangle$, is such that $n'_z > n'_m$ then $\sqrt{n'_z(n'_m+1)} > \sqrt{n'_m(n'_z+1)}$ and the state will have a higher probability to transition into $|n'_z-1, n'_m+1\rangle$ than $|n'_z+1, n'_m-1\rangle$. The state will continue to evolve until the transition probability of both final states are equal which clearly occurs at $n'_z = n'_m$. (Changing the initial state to either $n'_z < n'_m$ or $n'_z = n'_m$ results in the same final state as above.)

Sideband cooling turns out to be an important experimental tool as it is used to bring particles into a small radial orbit. The previous sections results showed that cylindrical traps can be used as Penning traps but only over a small central volume. Large radial orbits will not have harmonic axial potentials and therefore are generally avoided.

Chapter 3

Particle Detection

The detection of particles in the Penning trap falls into two categories, non-destructive and destructive measurements. Non-destructive measurements rely on the AC currents induced by the oscillating particles onto the conductive electrodes of the Penning trap. Destructive measurements are based on particle annihilation signals. As the apparatus for the destructive annihilation detection was provided by other members of the ATRAP collaboration it will only be briefly summarized here.

3.1 RF Detection

As has been discussed in the previous chapter, trapped particles induce signals on the trap electrodes. As the signals are extremely small (10 fA / particle), large amounts of gain must be used to monitor the signals.

A schematic of the RF detection circuit is shown in Fig. 3-1. The circuit is divided into three parts, the particles, the resonator, and the cold gain. The center-of-mass motion of the particles is represented by a capacitor and inductor in series. The justification of this representation is as follows. It has been previously shown in Section 2.2 that the charge induced on the compensation electrode by an axially displaced particle to be

$$Q_{comp} = \kappa z_a \tag{3.1}$$

Combining this with the result [27] of the compensation potential needed to displace a particle's equilibrium position

$$z_{equil} = \left(\frac{d^2}{2z_o}\right)\frac{d_1}{C_2}\left(\frac{V_{comp}}{V_o}\right) \tag{3.2}$$

gives

$$Q_{comp} = -\frac{\kappa e^2}{m\omega_z^2}\frac{d_1}{2z_o}V_{comp} \tag{3.3}$$

This relationship between charge and voltage is that of a capacitor and therefore the

particle has a capacitance of

$$c_e = \frac{\kappa^2 e^2}{m\omega_z^2} \tag{3.4}$$

where the relationship $\kappa = -\frac{d_1}{2z_o}$ has been used.

Similarly the inductance of the particle can be determined. Assuming that $V_{comp} = V_{co}\cos(\omega_z t)$ and $Q_{comp} = Q_{co}\cos(\omega_z t)$ and taking two time derivatives gives

$$\dot{I}_{comp} = \frac{\kappa e^2}{m}\frac{d_1}{2z_o}V_{comp} \tag{3.5}$$

This result shows that the particles behave like an inductor of inductance

$$l_e = \frac{m}{\kappa^2 e^2} \tag{3.6}$$

For reference, a positron that has an axial oscillation of 30 MHz will have a corresponding capacitance of 5×10^{-21} F and inductance of 6 kH.

The resonator is a RLC series circuit with a non-zero temperature, lossy inductor represented as an inductor, voltage source and resistor. The resistor is the active element of this pre-gain stage. Without this element there would be no signal as all other components are passive.

The two capacitors represent the capacitance between the signal electrode and the neighboring electrodes and the capacitance of the signal line to ground surfaces near it. The cold gain comes from a Mitsubishi MGF1100 MESFET which takes its input from a tap on the inductor. This tap point is chosen as a balance between maximum signal (tapped as shown in the figure) and minimum noise going to the particles (tap being placed at other end of inductor, thereby shorting FET noise to ground.)

The justification of representing the particles as circuit elements will be shown in a following section. The coupled buildup cavity is schematically shown in Fig. 3-2 with the two sources of capacitance combined into a single element.

The current in this circuit is

$$I(\omega) = \frac{VR}{R^2 + \omega^2 L^2\left(1 - \frac{1}{\omega^2 L^2 C^2}\right)^2} \tag{3.7}$$

The definitions in Table 3.1 with the approximation $\omega \approx \omega_o$ give

$$I(\omega) = \frac{V/R}{1 + \left(\frac{2(\omega-\omega_o)}{\Gamma}\right)^2} \tag{3.8}$$

The voltage source in this schematic is the thermal voltage produced across a resistor at non-zero temperature. On average this voltage is given by

$$V(T) = \sqrt{4k_b TBR} \tag{3.9}$$

where B is the bandwidth identified with the resolution bandwidth of the spectrum

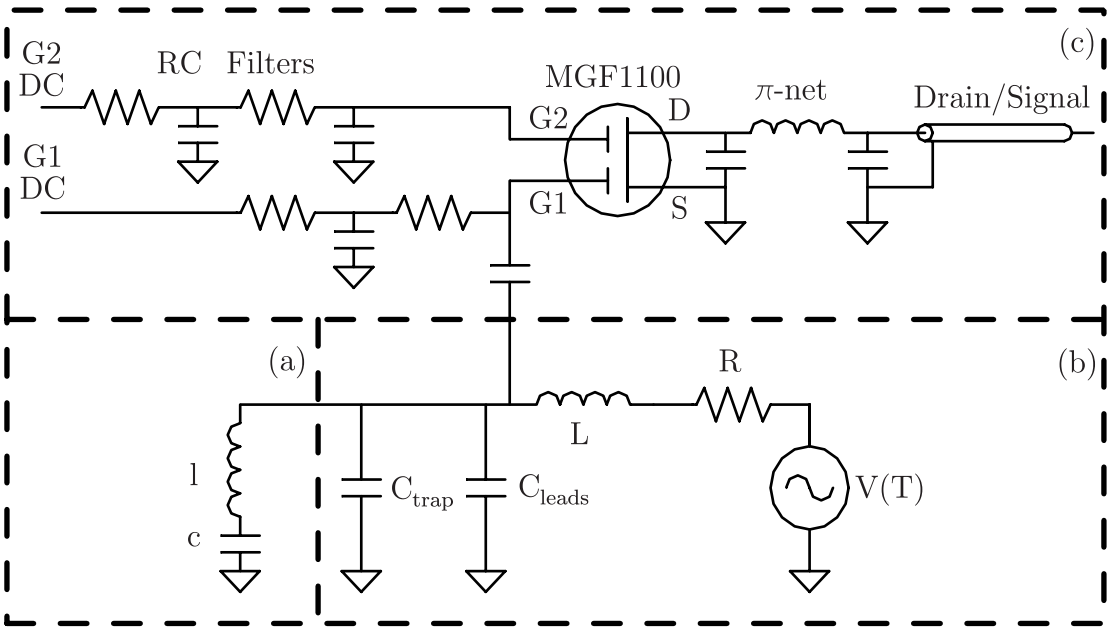

Figure 3-1: Electrical schematic of the RF particle detector divided into three sections. The schematic shows the particles represented by a capacitor and inductor in series (a), the resonator (b) with a voltage source and resistor coming from the lossy inductor, and the cold gain (c) supplied by a Mitsubishi MGF1100 MESFET.

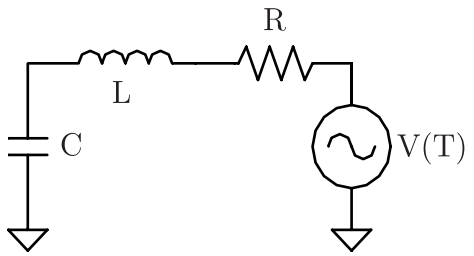

Figure 3-2: Schematic of RF buildup cavity

ω_o	$\frac{1}{\sqrt{LC}}$	$\frac{1}{\sqrt{LC}}$
Γ	$\omega_o^2 RC$	$\frac{R}{L}$
Q	$\frac{1}{\omega_o RC}$	$\frac{\omega_o L}{R}$

Table 3.1: Q and Γ table showing definitions of parameters in terms of inductance or capacitance

analyzer used to monitor the output signal. Substituting this into (3.8) gives

$$I(\omega) = \frac{\sqrt{4k_bTB/R}}{1 + \left(\frac{2(\omega-\omega_o)}{\Gamma}\right)^2} \tag{3.10}$$

The measured signal is nominally the voltage measured across the capacitor (although we frequently tap down on the inductor, thereby reducing the noise going back to the particles and optimizing the impedance matching) which is

$$V_{signal}(\omega) = Q\left(\frac{\omega_o}{\omega}\right)\frac{\sqrt{4k_bTBR}}{1 + \left(\frac{2(\omega-\omega_o)}{\Gamma}\right)^2} \tag{3.11}$$

This signal is a Lorentzian with FWHM of Γ.

The next section of the RF detector is the cold power gain stage. Figure 3-3 shows the various components. The diagram can be separated into DC biases to bring the MGF1100 to the correct operating mode, the capacitively coupled input, the MGF1100, and an impedance matching π-net.

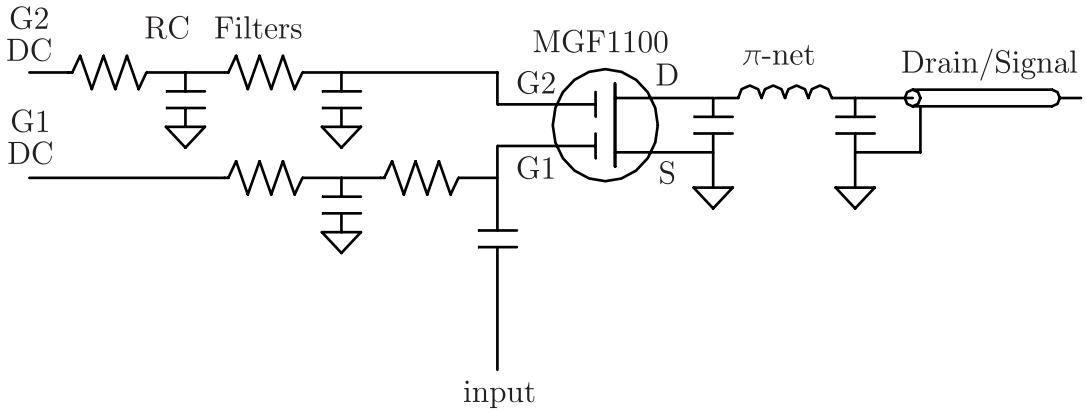

Figure 3-3: Diagram of typical components in the cold stage amplifier

In typical use the MGF1100 has a transconductance of

$$g_t = \frac{I_{DS}}{V_{G1S}} \approx 0.01\Omega^{-1} \tag{3.12}$$

and a output impedance of 10 kΩ [31]. The π-net acts to transfer the power from the high-impedance output of the MGF1100 to the low-impedance input of the following room-temperature amplifier chain. Therefore the power at the first room-temperature amplifier is given by

$$P = g_t^2 V_{signal}^2 R_{out} = V_{signal}^2/\Omega \tag{3.13}$$

A typical amplifier resonance can be seen in Fig. 3-4 at three different temperatures

with the Q at 4 K reaching nearly 1500.

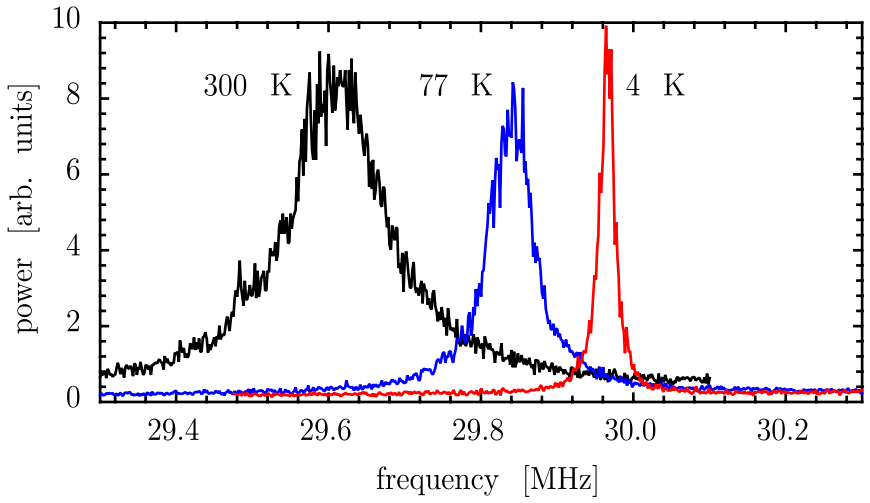

Figure 3-4: Resonance of amplifier at different temperatures

Once particles are trapped in a harmonic well, the noise voltage drives the center-of-mass motion of the particles. This linking of particles and detection will "short out" the amplifier at the particles' frequency. By tuning the trap voltages to bring the particles into resonance with the amplifier, a "dip" in signal can be seen. As the particles' signal width has been shown to depend on particle number, the dip can be used as a particle counter.

With the above results for the particle's capacitance and inductance a circuit analysis of the particles interacting with the tuned circuit [32] gives a power spectrum of

$$P(\omega) \propto \frac{\omega_{LC}^4(\omega_x^2-\omega^2)}{[(\omega_z^2-\omega^2)(\omega_{LC}^2-\omega^2)-\omega^2\Gamma N\gamma_z]^2+\omega^2\Gamma^2[(\omega_z^2-\omega^2)+\Gamma N\gamma_z]^2} \tag{3.14}$$

which reduces in the small number limit ($N\gamma_z \ll \Gamma$) to

$$P(\omega) \propto \left[1-\frac{(N\gamma_z/2)^2}{(\omega_z-\omega)^2+(N\gamma_z/2)^2}\right] \tag{3.15}$$

and in the large number limit ($N\gamma_z \gg \Gamma$) to two separate peaks with separation according to

$$\delta\omega = \sqrt{N\gamma_z\Gamma} \tag{3.16}$$

An example of a large cloud which satisfies this limit is shown in Fig. 3-5 with the non-particle resonance shown as a reference.

For the small limit Fig. 3-6 shows the dip of 8 positrons.

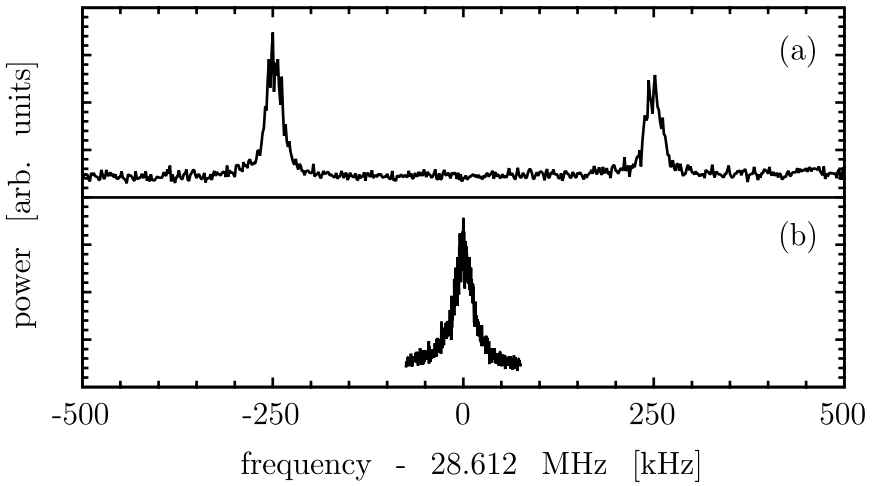

Figure 3-5: Signal of (a) one million positrons and (b) the amplifier resonance

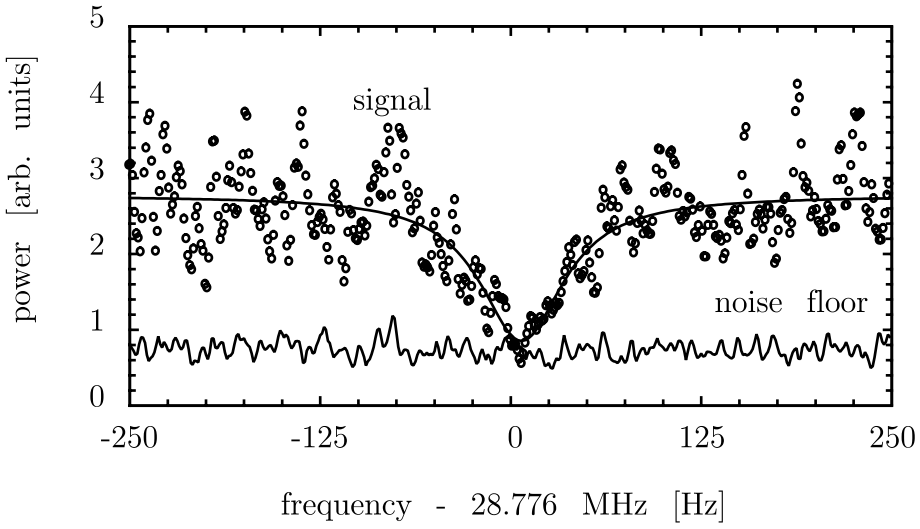

Figure 3-6: Eight positrons shorting out the amplifier signal

3.2 Antiproton annihilation detection

Although working with antimatter particles in normally more difficult than matter particles there are also some advantages. One that will be mentioned here is the availability of destructive detection techniques.

Antiproton annihilation occurs with many possibilities for decay products. The simplest decay that is realized is an antiproton-proton annihilation. One possible outcome is

$$\bar{P} + P \rightarrow \pi^+ + \pi^- + \pi^0 \tag{3.17}$$

The actual antiproton-proton decay has many decay channels but on average it can be written [33]

$$\bar{P} + P \rightarrow 1.5\pi^+ + 1.5\pi^- + 1.7\pi^0 \tag{3.18}$$

where unlikely events and gammas have not been included.

Since the trapped antiprotons can annihilate on many different surfaces in the Penning trap a statistical analysis should be done based on the different materials that could trigger the annihilation and the outcomes of each material.

The antiproton annihilation detector consists of two distinct detectors. Following the path of a π^+ from its creation on the surface of an electrode is instructive and can be seen in Fig. 3-7. As the pion travels away from the center of the Penning trap it will reach the first antiproton annihilation detector, the fiber detector. This detector is made from optical fibers which are able to change the energy loss of the traversing pion into an optical signal. This light is detected with photomultipliers. Because of the high average number of events from a single antiproton annihilation, this detector operates with a near 100% detection efficiency. This detector also detects cosmic events and suffers from some level of electrical noise which gives a noise count rate of 75 per second. In order to reduce the noise counts, the normal event from this detector is two events in coincidence (20 ns time window) from two separate layers reducing the background rate to 10 counts per second.

The other detector of antiproton annihilation is the paddle detector. This detector consists of 18 rectangular paddles arranged in concentric circles around the magnet. This detector has a 50% efficiency of detecting single antiproton annihilation. As these detectors also have high noise rates, single events in this detector are coincidences between two layers as with the fiber detector. An event in this detector is a signal in both of the two layers such the first and second layer adjacent.

A further decrease in noise can be had from combining the events from the two detectors. This combined signal was known as the trigger since it could be used to start a data acquisition cycle. The trigger is the logical AND of both detectors. A complete listing of efficiencies and noise backgrounds can be seen in Table 3.2.

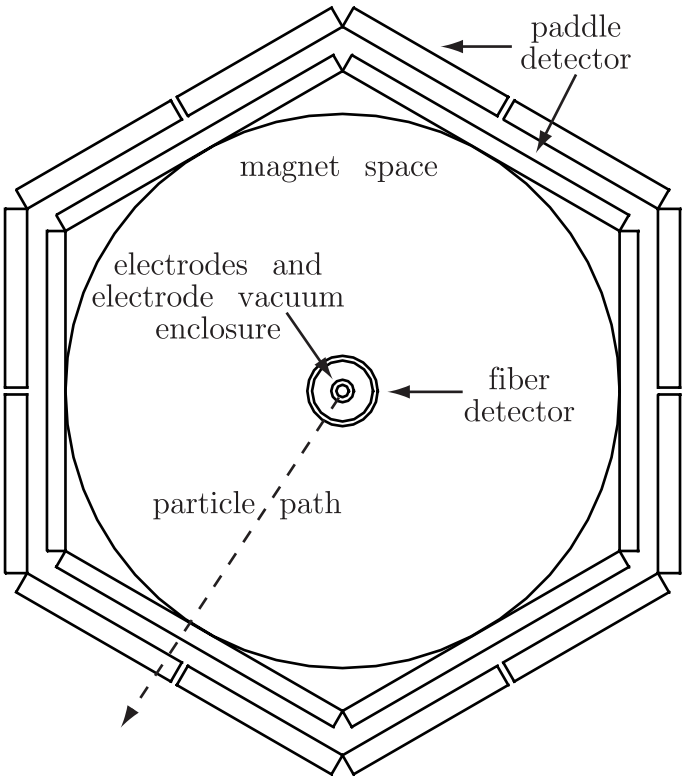

Figure 3-7: π^+ path from creation on an electrode. The π^+ is created from an antiproton annihilation on an electrode surface. Once created it follows a path which crosses both the fiber and paddle detectors, often creating light in both systems. (The curvature of the π^+, due to the magnetic field, is not shown in this figure.)

Detector	efficiency	background count rate [s^{-1}]
Double Paddle Layer	50%	60
Double Fiber Layer	100%	10
Trigger	50%	3

Table 3.2: Antiproton annihilation detector parameters

Chapter 4

Positrons

Trapping positrons from a radioactive source presents interesting difficulties. The list includes the short lifetime of positrons in contact with matter, the continuous emission characteristic of radioactive sources, and the initial amount of kinetic energy with which positrons are emitted. Here we report a new trapping mechanism [1] with rates of $1.4 \times 10^4\, e^+\, \mathrm{h}^{-1}\, \mathrm{mCi}^{-1}$, orders of magnitude greater than a previously demonstrated electronic cooling method [34] or any other method of accumulating 4.2 K positrons. This method, using a Penning trap shown in Fig. 4-1, is compatible with extreme high vacuum and cryogenic temperatures making it ideal for precision studies with antimatter.

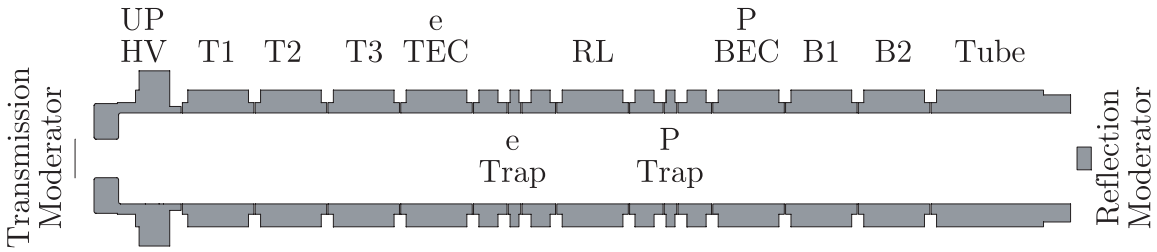

Figure 4-1: Penning trap used for positron studies

Our studies, which focused on the symmetric nature of positron and electron capture from a radioactive source, have shown and explained a new physical mechanism for accumulating cold positrons and electrons. Highly energetic positrons, from a ^{22}Na source, are passed through a moderating tungsten crystal. Highly excited positronium is created as slow positrons leave the crystal, followed by an associated secondary electron. The positronium continues in the direction of the strong (5.3 T) magnetic field and enters a trapping region where it is ionized by an electric field. The ionization field is arranged such that either the positron or the electron is trapped, depending on the sign of the trapping well. Equal amounts of positrons and electrons are captured, indicating the crucial role of positronium. By varying the ionization field and trapping well depth, we have been able to identify a region of the positro-

nium's phase space. The positronium that we create has an initial kinetic energy around 1 eV and interparticle separation of a few μm.

We have also introduced a second tungsten crystal to give the unmoderated positrons an extra channel to eV energies. These moderated positrons are then accelerated back to the first moderator where they become bound with an electron to form positronium. This additional channel increases the accumulation rate by 250%.

The first interaction between cold antiprotons and positrons exhibited a linking between the two trapping mechanisms [2]. The apparatus was unable to accumulate positrons once antiprotons had been captured. Postulating that the antiproton beam had removed an adsorbed gas layer from the tungsten crystal used for positronium creation, the 4.2 K Penning trap was temperature cycled to 300 K. This 12 hour process restarted the positron accumulation mechanism. In order to study this problem without the use of antiprotons, we installed an optical fiber linking the 4.2 K, extreme-high vacuum, Penning trap to an external laser. Up to 4 W of laser light, directed on the thin tungsten crystal, was able to arrest the positron accumulation, as seen with antiprotons. We now understand the need for this adsorbed layer, although its specific role in positronium formation is yet to be explained. To protect this adsorbed layer, we designed and installed a rotary electrode in the apparatus designed for further antiproton and positron studies. The use of this rotary electrode has allowed us to capture positrons and antiprotons in the same apparatus without the previous linking seen before.

4.1 Radioactive source delivery and storage system

In order to trap positrons from a radioactive source, the source needs to be placed near the trapping region. As the placement of a radioactive source in this area both creates a hazard for experimentalists working nearby and renders annihilation particle detectors useless, the source was designed to be moved near the trapping region as needed. Thus, a system was needed to move the radioactive source to either the loading position or a shielded position. Positron experiments were done with either of two source delivery apparatus both of which will be discussed. These apparatus will be referred to as the Harvard and the CERN apparatus for reasons which will become clear.

The positron mechanical system of the Harvard apparatus was first built and used at CERN for the first attempt at cold antihydrogen. After that use, which lasted only a few months, the system was then shipped to Harvard where work on understanding the positron trapping mechanism, reported here, was performed.

The CERN positron system was first partially assembled at Harvard for intermediate tests and then completed at CERN where it is still in use. This system was improved compared to the Harvard system, incorporating a laser access port, a 140 K source precooling system, and a non-vertical storage position to protect annihilation detectors from gamma radiation from the source.

4.1.1 Harvard system

The Harvard positron apparatus can be seen in Fig. 4-2 which includes the positron blockhouse. The straight blockhouse pictured above the experiment serves several purposes. The first is radiation protection. The ^{22}Na material that is used as the source of positrons emits harmful radiation. The design philosophy of the source container was that there should be a negligible increase in radiation compared to the natural background for people working around the experiment. With this constraint, lead shielding was needed to absorb the emitted radiation from the source. The other purposes of this straight blockhouse are the ability to hold a vacuum and once under vacuum to move the source near and away from the Penning trap region.

Keeping the source under vacuum was done using mostly standard vacuum equipment but the source movement was more difficult. The source movement design was heavily constrained including the following necessities...

- Source must be able to move vertically 2 m
- The system must not warm up the Penning trap
- The system must be robust as failures with radioactive materials may ruin an entire trapping system
- Source movement must be able to accept tolerances as great at 0.5 mm

A schematic drawing of this storage blockhouse is presented in Fig. 4-3. The main functional parts of the system in regard to source movement are a computer controlled stepper motor, high performance string used to position the source, string tension sensor and two position sensors. The movement of the source was done via computer control with software that continuously checks string tension and the state of the position sensors.

In addition to being able to move the source into position for trapping, the positron mechanical system must be able to inhibit and allow the beam the enter the trapping region. This is necessary as the loading rate of positrons or electrons was normally the measurement being made. This timing was accomplished via a rotatable beam shutter which allows the positron beam to enter the trapping region when open. The chopping system includes a computer controlled stepper motor with independent position detection, a rotary motion feed-through, thermally non-conductive rods to transfer the motion to the 4.2 K environment, and a metallic plate sufficiently thick to stop all the positrons which come from the source. As an independent check on the position of the beam stop, the current on this stop and on the transmission moderator were monitored with a low-noise, precision ammeter. A plot showing the opening and closing of the beam shutter can be seen in Fig. 4-4.

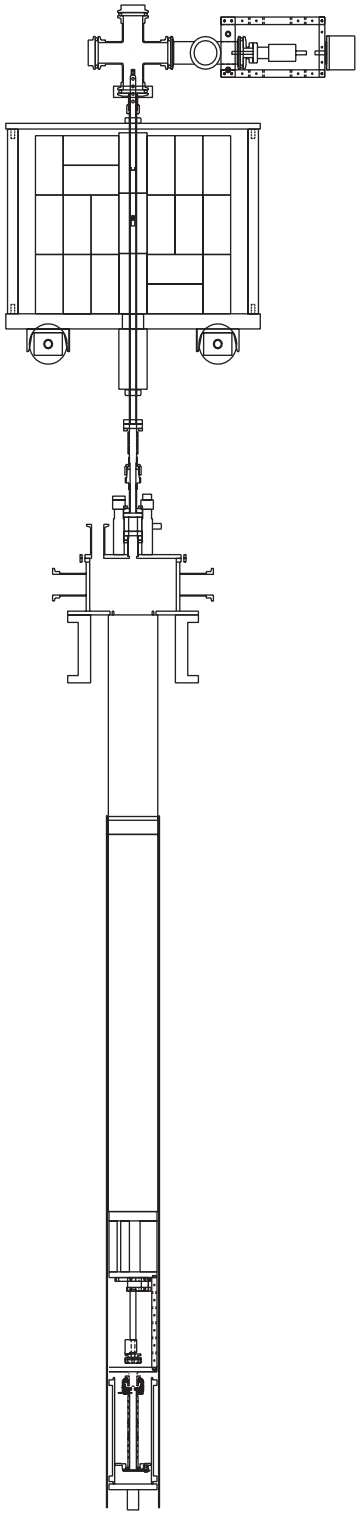

Figure 4-2: Penning trap apparatus used in Harvard positron experiments

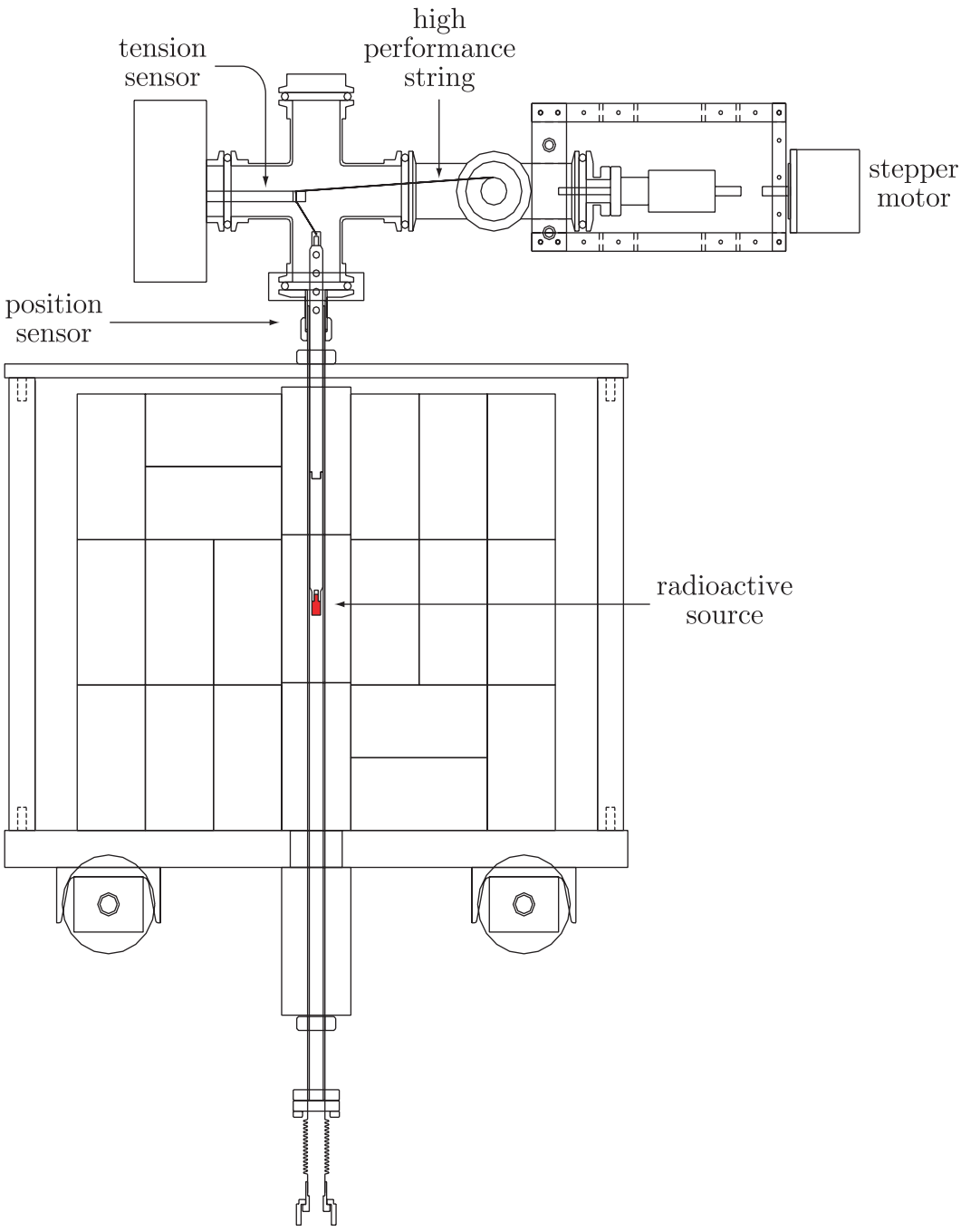

Figure 4-3: Straight blockhouse used in Harvard positron experiments

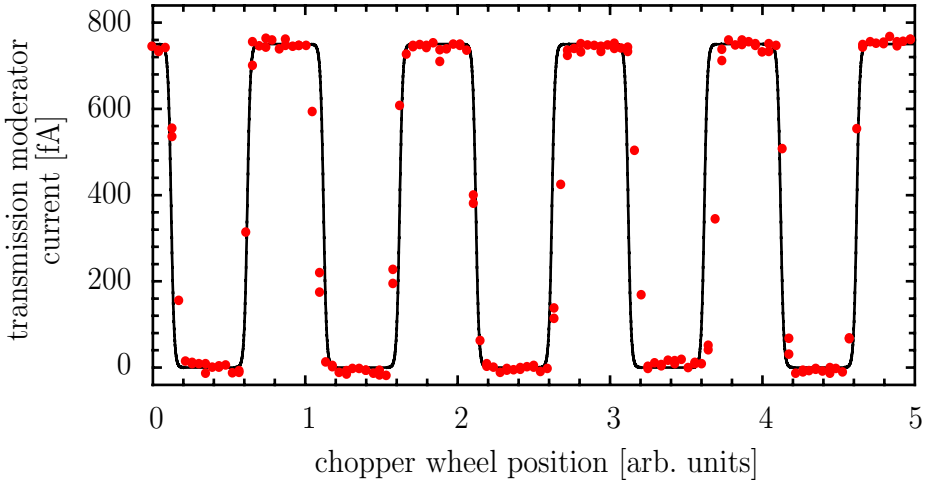

Figure 4-4: Positron beam current on transmission moderator as chopper wheel is cycled. This data shows the ability to chop the positron beam.

4.1.2 CERN system

A second positron mechanical system was built for use at CERN. Because the rates of antihydrogen production depend on the number (or density) of positrons, a new 150 mCi ^{22}Na source was acquired which would allow for much shorter loading times. (Figure 4-5 shows the much greater number of positrons that are trapped with the larger source.) In addition to needing more shielding, this source was also larger in diameter than the previous model and therefore had to have a larger channel through the experimental apparatus.

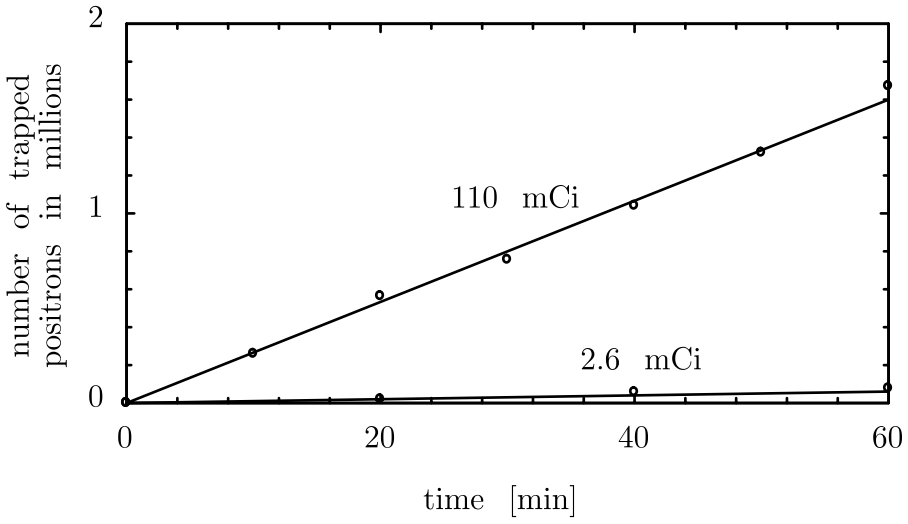

Figure 4-5: Positron loading rate improvement with stronger source

The structure of the positron blockhouse also incorporated three new features as this experiment needed to accommodate the abilities to make and detect antihydrogen. First, the source had to be shielded from below in order to keep the antiproton and positron annihilation detectors from detecting the large number of gammas which continuously come from the ^{22}Na source. This was accomplished by turning the source from the vertical to an angle of 45°. This rotation allowed the radiation to be well shielded by a Elkonite block. Next, the source had to be able to be moved out of the central axis so that the source travel channel could be used to allow laser light to enter the trapping region. This was accomplished by moving the source diagonally out of the central channel. Lastly, the source needed to be precooled in order to allow the trap to remain at 4.2 K when the source is brought down. This was done with a thermal connection between the source and a liquid nitrogen reservoir while the source is in a rest position in the block house. The CERN blockhouse can be seen in Fig. 4-6.

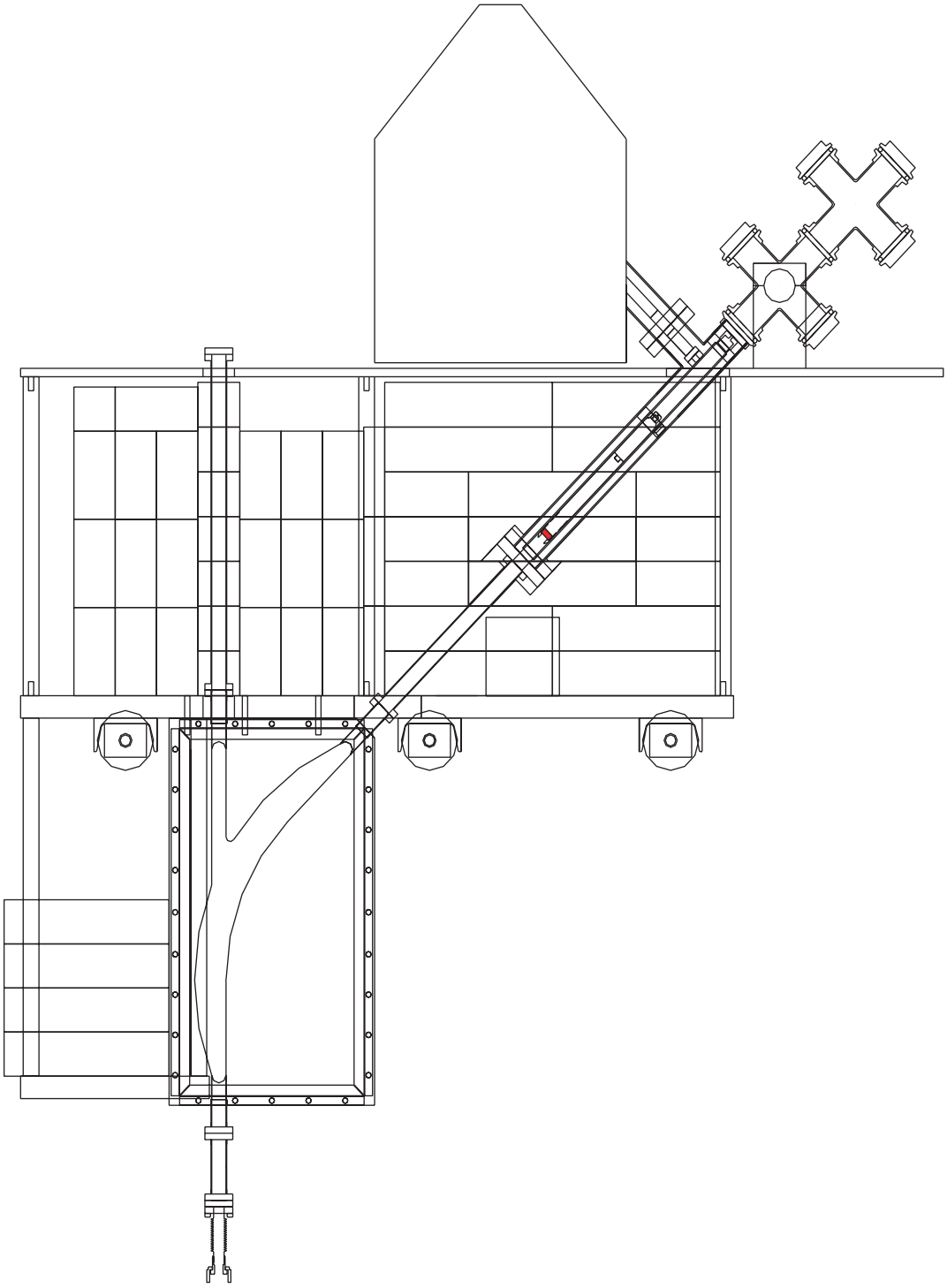

Figure 4-6: Blockhouse used in CERN positron experiments

4.2 Positrons outside the trap enclosure

Positrons are produced as ^{22}Na undergoes a nuclear transition changing one proton into a neutron

$$^{22}_{11}\mathrm{Na} \rightarrow {}^{22}_{10}\mathrm{Ne} + \mathrm{e}^{+} + \nu_e$$

This beta decay process produces positrons with a continuous distribution of kinetic energies between 0 and E_o, with E_o being the energy difference between the initial and final nuclei.

This distribution has been shown [35] to be of the following form

$$N(Z, E_e) = CF_{+}(Z, E_e)(E_o - E_e)^2(E_e^2 - m_e^2c^4)^{1/2}E_e \tag{4.1}$$

where $F_{+}(Z, E_e)$ is defined as follows

$$F_{+}(Z, E_e) = \frac{2\pi\eta}{1 - e^{-2\pi\eta}} \tag{4.2}$$

with

$$\eta = -\frac{Ze^2}{4\pi\epsilon_o\hbar v} \tag{4.3}$$

$F_{+}(Z, E_e)$ is used to account for the fact that the positron is repulsed by the nucleus and therefore reduces the possibility of low energy positrons being emitted. The other terms can be identified as C being a constant which is set to normalize the distribution, Z the final atomic number of the nucleus (10 in this case), E_e the positron energy and v the positron velocity. This distribution for positrons emitted from ^{22}Na is shown in Fig. 4-7.

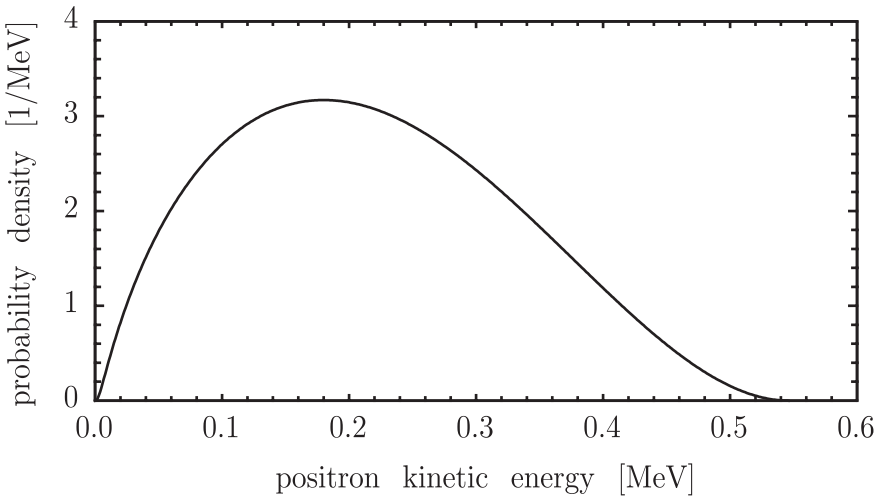

Figure 4-7: Energy probability density of positrons emitted by ^{22}Na

Not all the positrons leaving the source will arrive in the trapping region. A

careful study of the losses has been done [36, 32] and will only be summarized here.

With the ^{22}Na source in the trapping position, the magnetic field used for the Penning trap guides the positrons to move axially with their radial kinetic energy being contained in circular cyclotron orbits. The positrons coming from the source normally would have equal probability of moving either towards or away from the exit window, but a tungsten backing material in the source capsule increases the forward yield. Even so, 25-50% are moving in the opposite direction, 50% are absorbed in the source material and 33% are lost in the source capsule vacuum window. Therefore, only 21% of the positrons emerge from the source.

Once free from the source capsule, the positrons travel along the magnetic field lines towards the Penning trap. Because the radial cyclotron motion is quick compared to changes in the magnetic field, the magnetic flux through the particle orbit remains fixed. This can be equivalently express as an invariance of $p_\perp^2/B$. (Depending on the position of the source, the magnetic field may increase or decrease in strength as the positron approaches the magnetic field center.) Therefore, perpendicular momentum must also increase, thereby lowering the parallel momentum. Depending on the initial momentum angle of the positron, the positron may bounce off the magnetic field. This effect is shown in Fig. 4-8, where the source is raised out of the magnetic field, causing more positrons to bounce off the field, while the positron current on the chopper wheel is monitored.

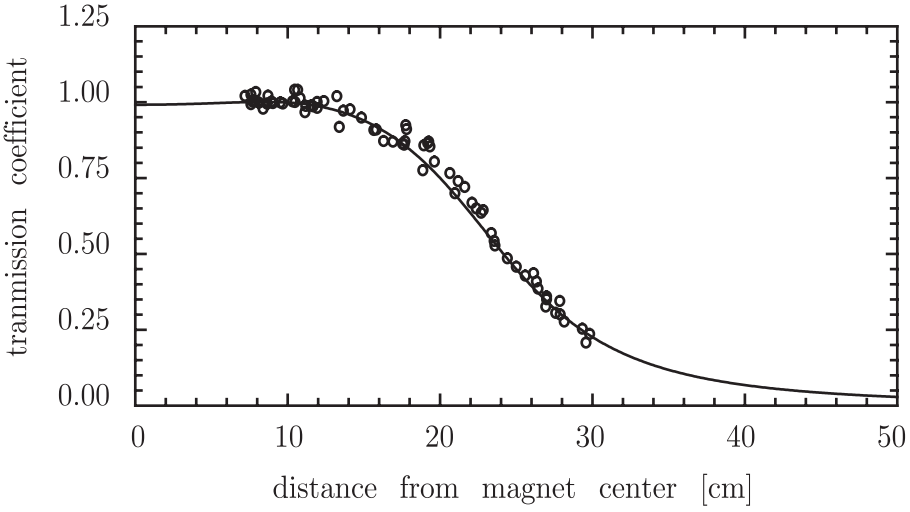

Figure 4-8: Positron current measured on the chopper wheel as the source is raised out of the magnetic field. The data follows a cosine distribution of momentum angle with respect to the axial direction.

As the positrons travel downward, they reach a 10μm Ti vacuum window, which separates the magnet bore vacuum from the extreme high vacuum of the trap itself. This window will also introduce a loss of 34%. At this point there is a 14% efficiency of positrons reaching the trapping region or 4.6×10^6 e^+/mCi/s.

A	B	C	Measured	Solved
+	-	+	$I_C = I_o$	I_o
- -	-	+	$I_C = I_o - i_2$	i_2
++	+	-	$I_C = I_o + i_3$	i_3
-	0	+	$I_A = I'_o - I_o - i_2 - i_3$	I'_o
+	-	+	$I_A = I'_o - I_o - i_0$	i_0
- -	-	+	$I_A = I'_o - I_o + i_1 + i_2$	i_1

Table 4.1: Positron/electron current measurements

	I [pA]	I [pA/mCi]
I_o	1.73	.540
I'_o	2.18	.680
i_0	-.35	-.11
i_1	-.46	-.14
i_2	-.41	-.13
i_3	-.62	-.19

Table 4.2: Positron/electron current values

4.3 Beam current measurements

In order to verify the number of positrons reaching the trapping region, current measurements were taken from the metal surfaces through which positrons pass. Since the positrons have high kinetic energies, it is possible to see effects of secondary electrons leaving surfaces. A complete picture of possible charged currents is shown in Fig. 4-9.

The secondary electrons are normally emitted with low kinetic energies but can be held in the material if it is appropriately biased. Conversely, the non-moderated positrons have energies which can not be overcome at low potentials. The small number of moderated positrons produced was such that it was not possible to measure their current with the methods used here.

By biasing the various conductors which pass or block positrons, one could measure the sum of the various currents. There exists a set of algebraic equations which determine the individual currents on each surface. The complete set of equations can be seen in Table 4.1. Although it was not possible to bias all surfaces through which currents passed, there were enough constraints that all pertinent currents could be determined. The determined values of all positron and electron currents are listed in Table 4.2.

Instead of biasing away all secondary electron emission, the bias can be swept over the range of energies of the electrons. In this way, the secondary electron energy

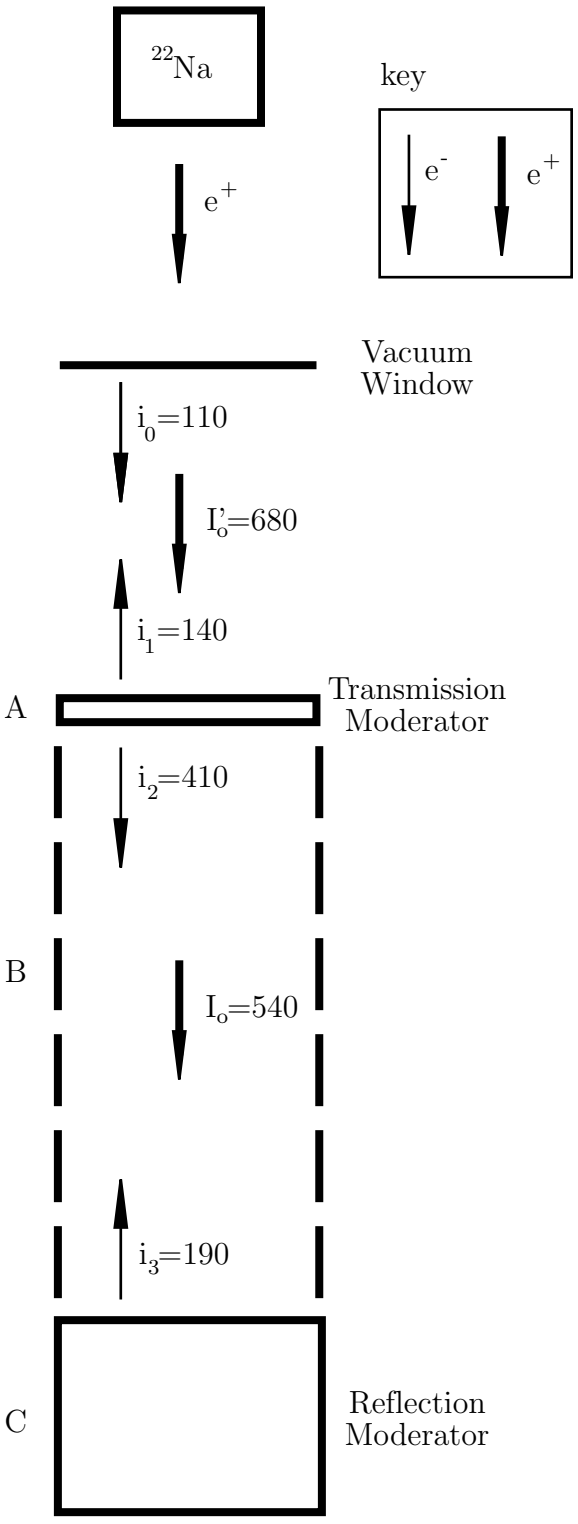

Figure 4-9: Positron and electron beam currents in trap region. All currents are listed in fA/mCi

distribution can be seen. For example, in Fig. 4-10 the forward electron distribution from the transmission moderator is shown.

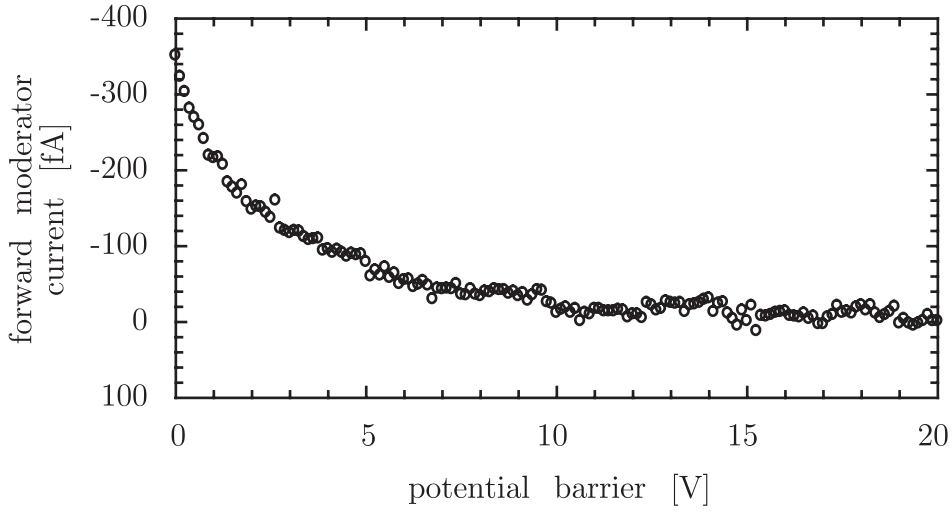

Figure 4-10: Forward electron current from transmission moderator produced when the positron beam is allowed to pass through.

4.4 Positronium

As previous work on positron and electron trapping suggested that the loading mechanism occurred via field ionization of excited positronium, experiments were carried out to validate this possibility. The model was that a small percentage of high energy positrons from the radioactive source thermalized within the transmission moderator. Upon leaving the moderator surface, a thermal positron picked up an electron to form a highly excited state of positronium. As the state of the positronium is highly excited, the particles are guided by the magnetic field. Once in the trapping region, applied electric fields separate the particles. Depending upon the sign and the magnitude of the potential where the particles separate, either the positron, the electron, or neither particle could become trapped. The potential along the direction of the magnetic field used in a typical positron capture experiment can be seen in Fig. 4-11 with typical trapping rates for this well in Fig. 4-12

In order to confirm that the positron loading was due to positronium, electron trapping was investigated. The idea was that the positronium production region potential (i.e. transmission moderator) should be held constant between electron and positron accumulation, while the particle capture region should have all potentials inverted. A typical potential field used is shown in Fig. 4-13

Figure 4-14 shows the loading rates of positrons and electrons are identically over a wide range of loading parameters, confirming the loading of both particles via the field ionization of highly excited positronium.

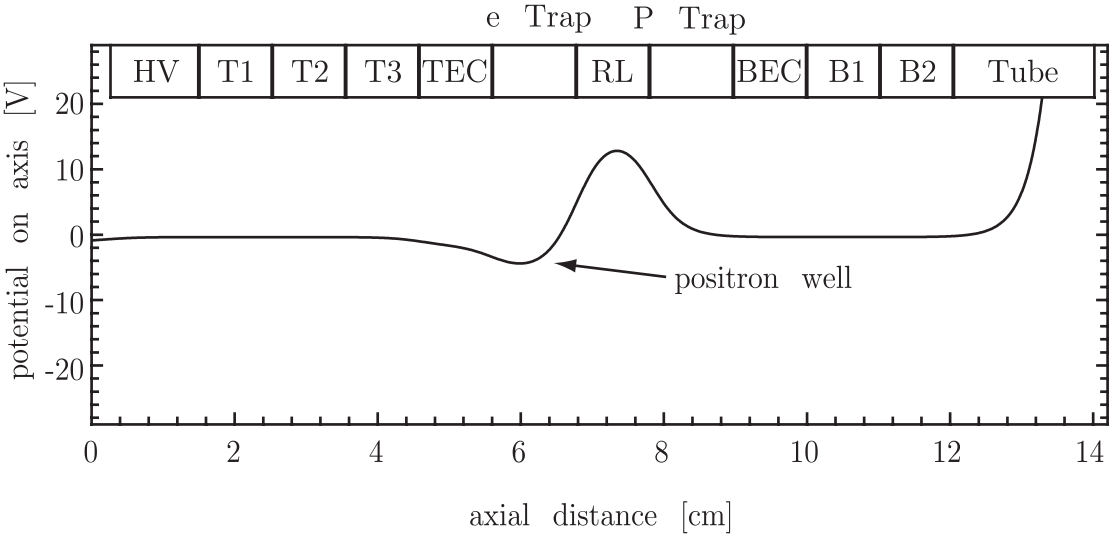

Figure 4-11: A potential field used for trapping positrons

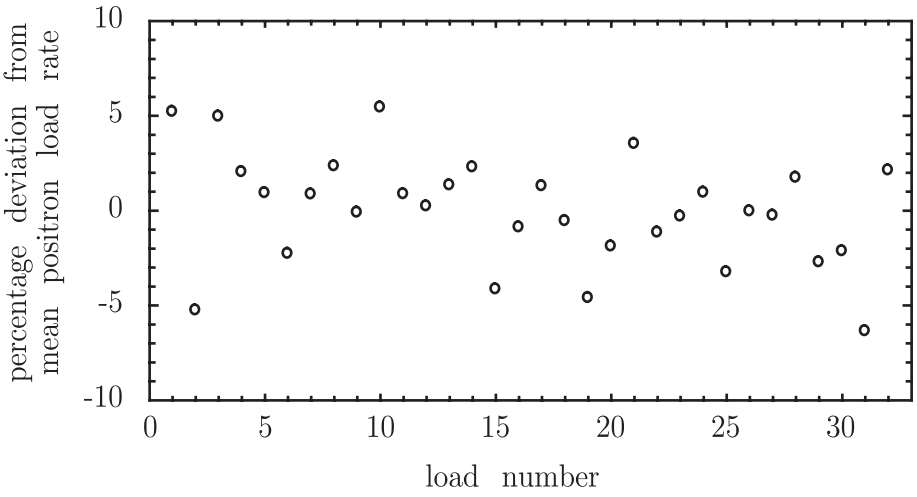

Figure 4-12: Repeatability of positron trapping with nominal 1 minute loads, giving approximatively 1000 positrons.

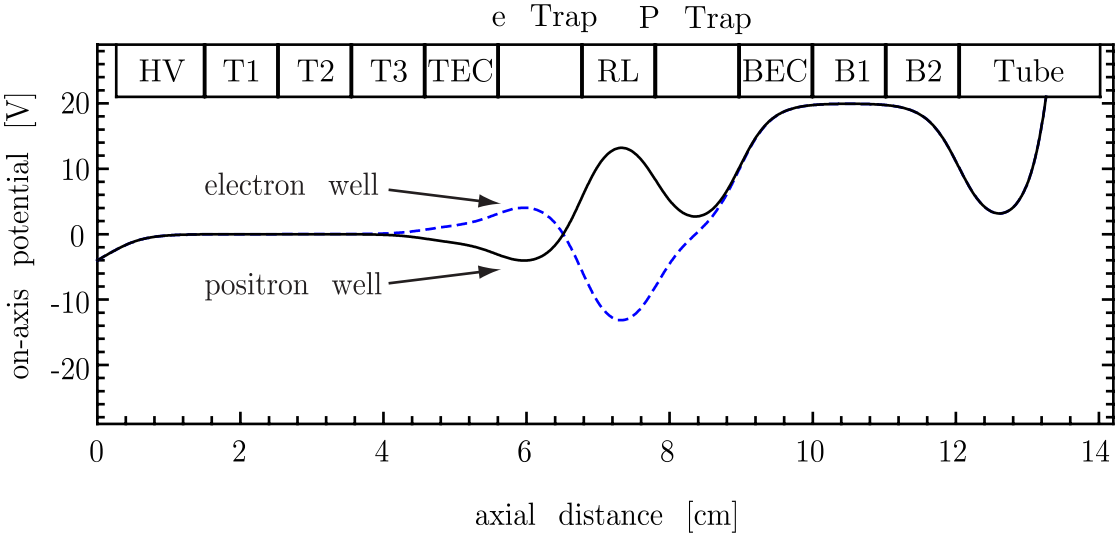

Figure 4-13: On-axis potential used to trap positrons and electrons

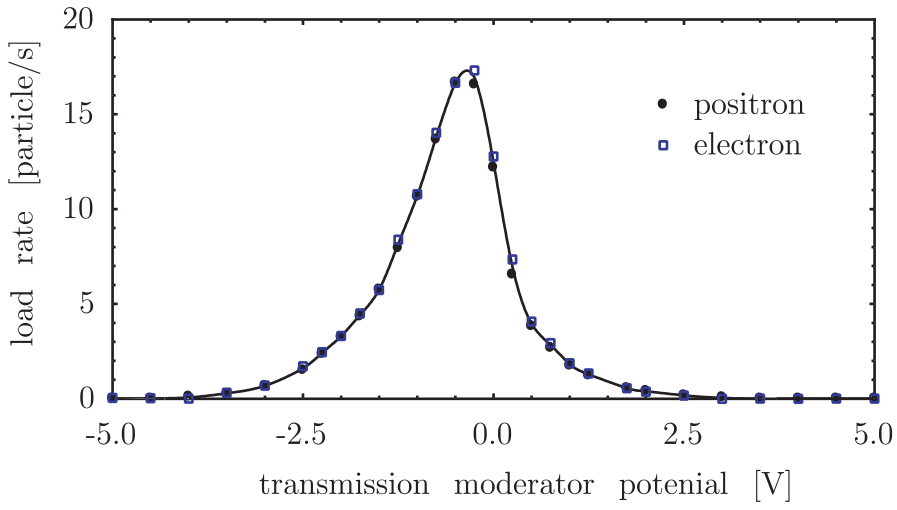

Figure 4-14: Loading rate dependence on transmission moderator potential showing symmetry between positron and electron trapping

In order to increase the positronium current, we have installed a reflection moderator to act on the unmoderated positron beam which passes through the transmission moderator. This second moderator creates a low-energy positron beam traveling back towards the transmission moderator. If this reflection moderator is then biased correctly, moderated positrons can reach the transmission moderator. These positrons then have another chance to bind with an electron to form positronium. Seen via the number of trapped particles, this beam does increase the amount of positronium leaving the transmission moderator. An illustration of the additional moderated positron channel can be seen in Fig. 4-15 with data supporting this view shown in Fig. 4-16.

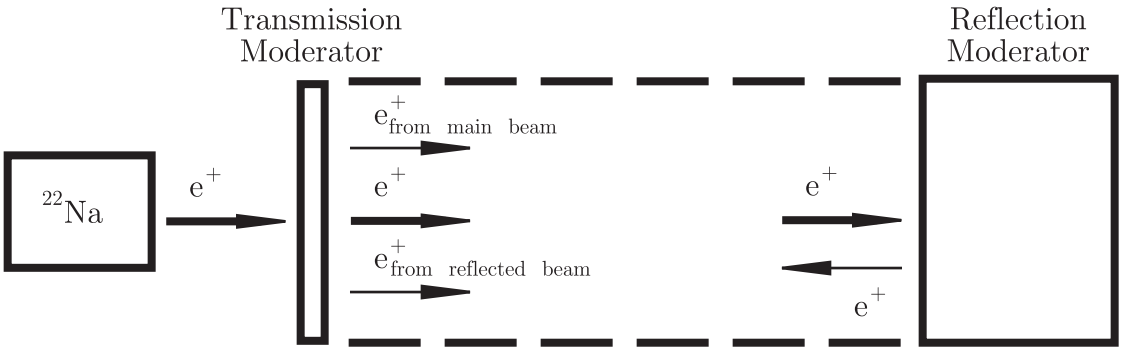

Figure 4-15: Using reflected positron beam to increase positronium production

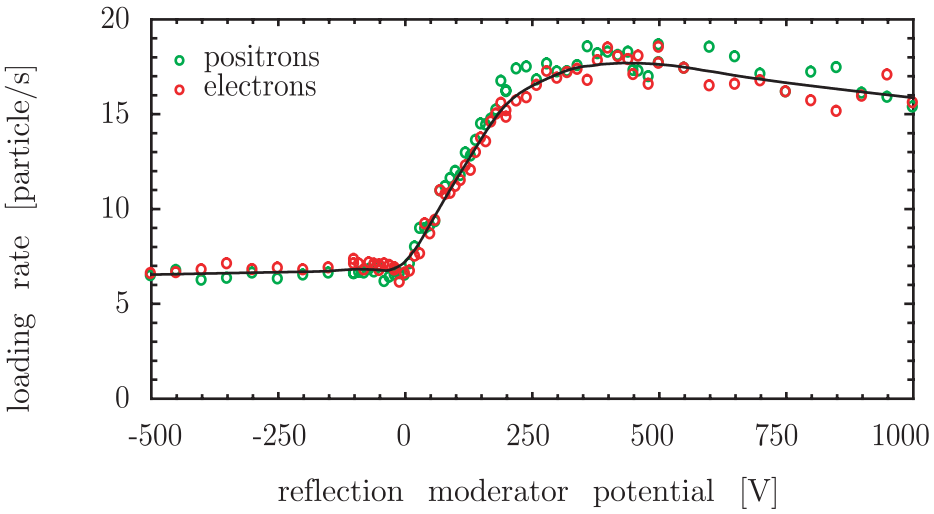

Figure 4-16: Increase of loading rate via acceleration of moderated positrons from reflection moderator

Although it seemed likely that the reflection moderator was improving the positron load rate through moderation, another possible mechanism exists. It is the reflection

of positrons with energies below 100 eV by the potential of the reflection moderator. This channel would not depend at all on the material used as a positron mirror, only the potential applied. To determine if this indeed was the case, the electrodes which come before the reflection moderator were biased to the nominal reflection moderator bias. The potential seen in the two cases is shown in Fig. 4-17. The dramatic difference in loading rates when using the reflection moderator or a potential to reflect positrons shows that moderation does occur and is responsible for the increased loading rate.

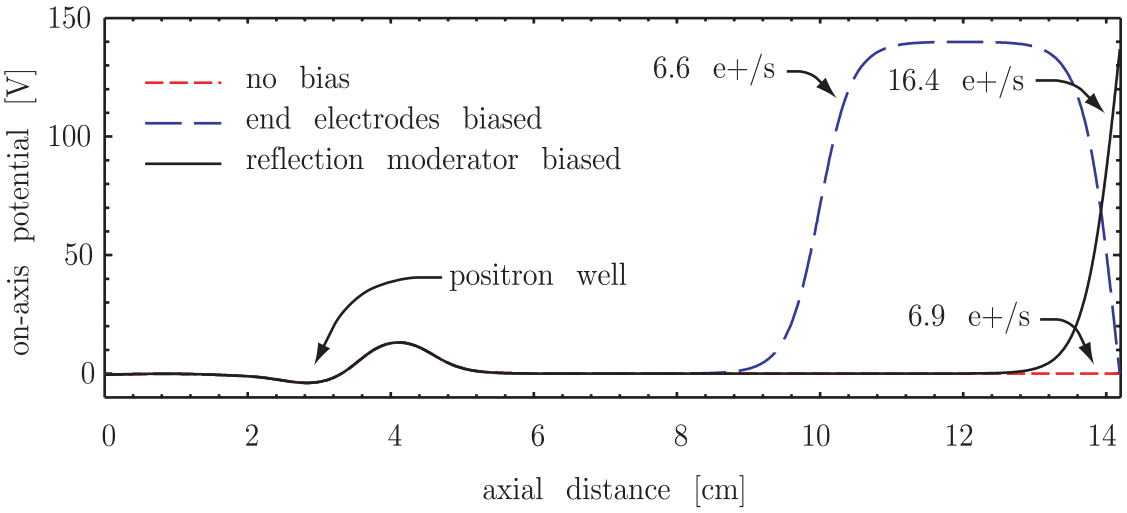

Figure 4-17: Potentials used to determine whether positronium increase is sensitive to material

Using this second source of moderated positrons, we were able to probe the energy distribution of this beam in an indirect manner. This technique is the measurement of the loading rate associated with the particular beam. We controlled the blocking of the moderated positron beam from the reflection moderator. By varying the difference in potential between this beam and the blocking potential one measures the energy distribution of the moderated beam. A plot of the potential can be seen in Fig. 4-18 and the data showing the energy distribution of these moderated positrons in Fig. 4-19. The indicated FWHM of the distribution depends on the fitting function used with fits of 2.5 eV also in agreement with the data.

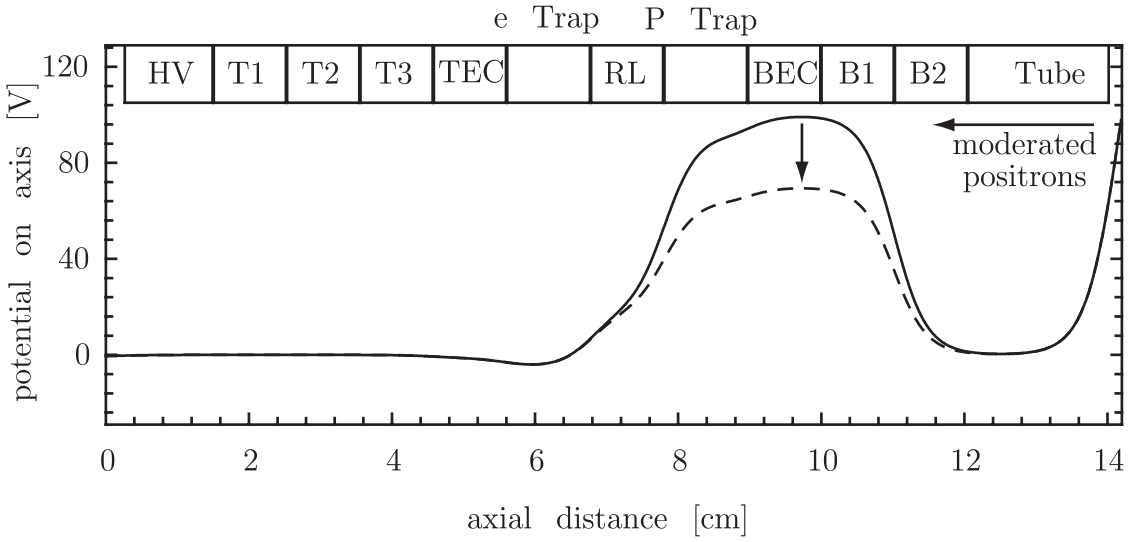

Figure 4-18: Plot of the potential used to analyze the energy of the moderated positrons from the reflection moderator

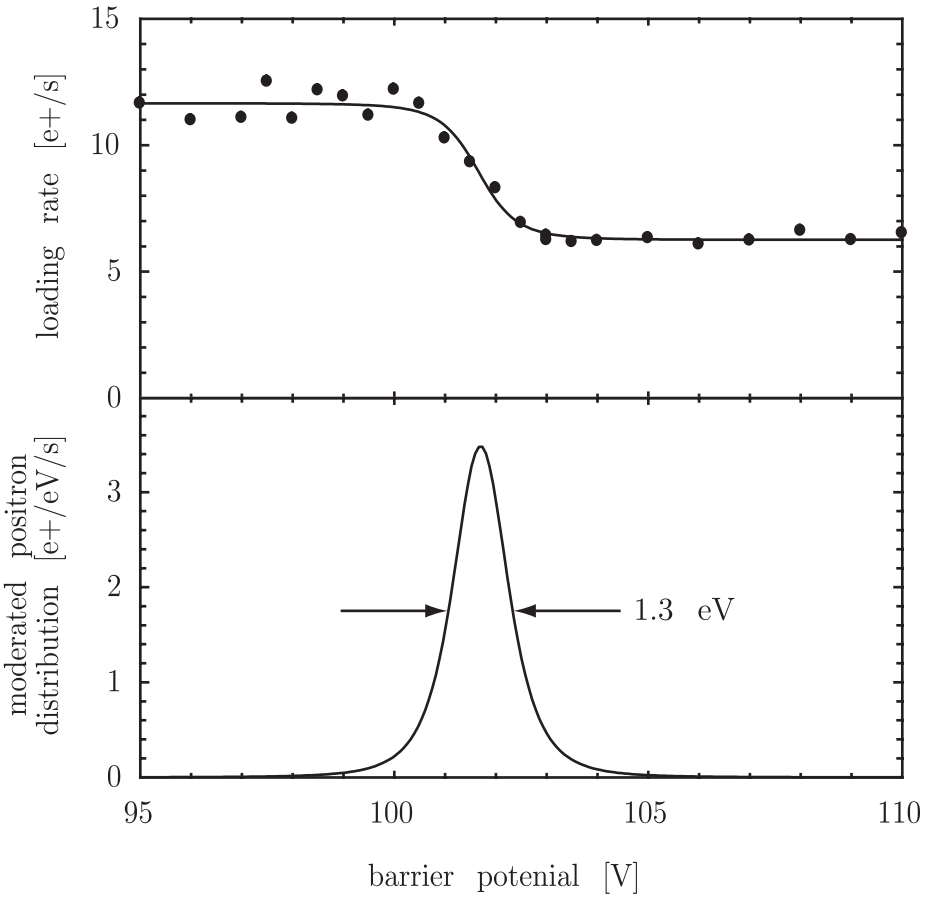

Figure 4-19: Positron loading rates as a barrier blocking the reflected beam is changed. This data then shows the distribution of moderated positrons being reflected by the reflection moderator. The reflection moderator was biased to 100 V, showing that the moderated positrons leave with a average energy of 1.7 eV and a FWHM of 1.3 eV.

4.5 Distribution of positronium

By varying the potential used to capture positrons one is actually probing the phase space of initial positronium states. Using a simple 1-dimensional model of the field ionization of positronium, one can map out a phase space that would result in a trapped positron. Although this reconstruction only limits the initial states to a range of initial conditions, this does give an idea of the initial states created. Data sets used for this purpose can be seen in Figs. 4-20, 4-21, and 4-22 with a partial phase space diagram in Fig. 4-23.

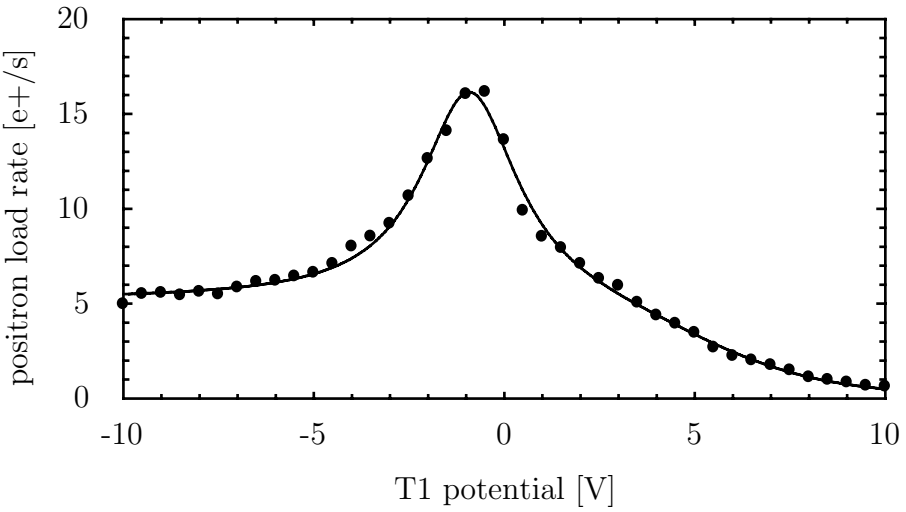

Figure 4-20: T1 map. This electrode acts to set the electric field seen as the positronium first enters the trapping region. A large positive value acts to field ionize the positronium before the positron is in location where trapping can occur. A large negative value also results in field ionization yet increases the physical space of the positron trapping region.

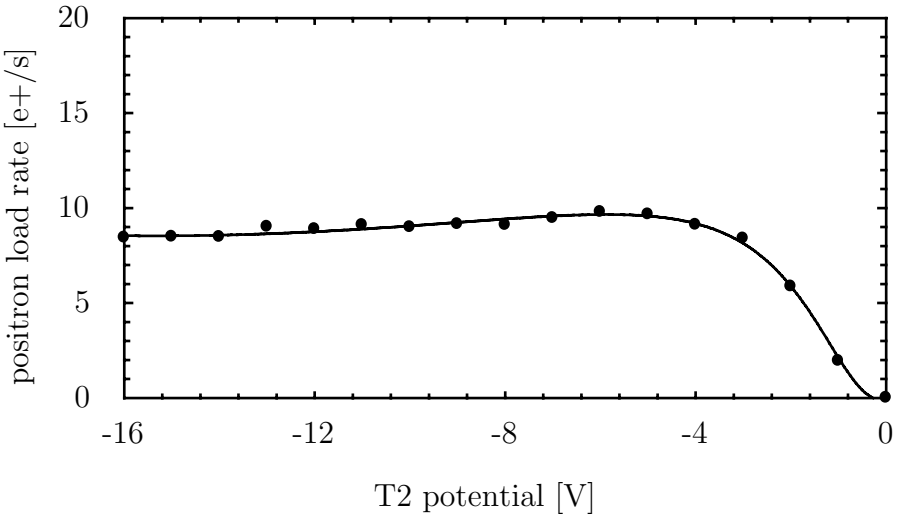

Figure 4-21: T2 map. This electrode is the positron trap. A shallow well allows positronium to enter yet does not field ionize the particle to trap the positron. Increasing the potential, over the range shown above, shifts the field ionization point towards the edge of the well but such that trapping still occurs.

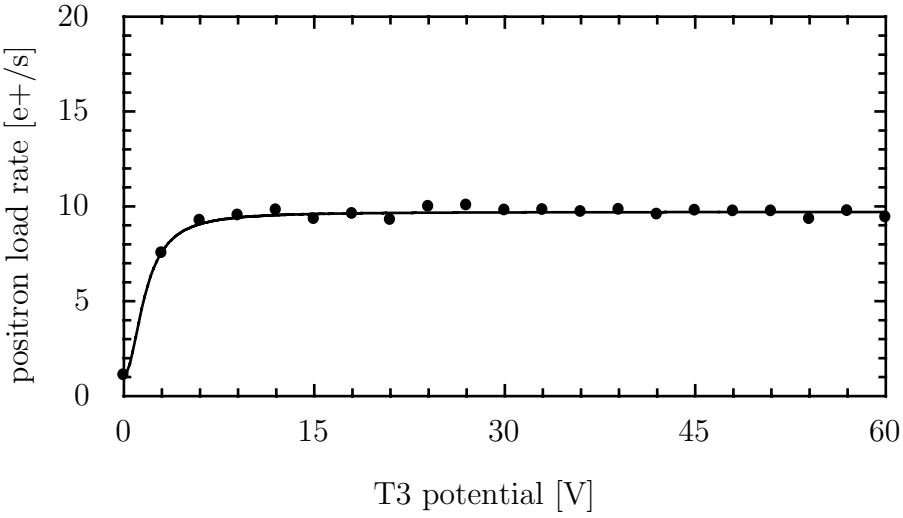

Figure 4-22: T3 map. This electrode is used to place a large electric field in the positron well. Once this field is sufficiently large to field ionize positronium no effect is seen as greater potential act only to shift the ionization to points deeper in the well.

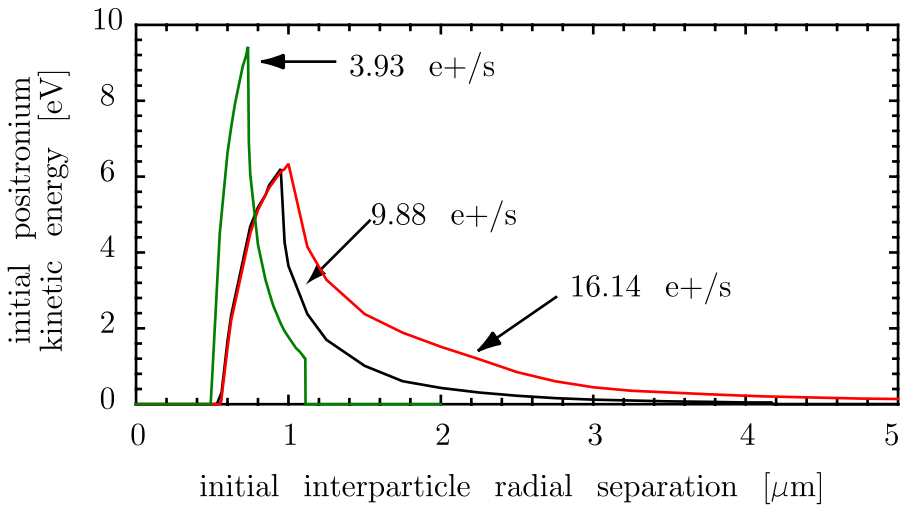

Figure 4-23: Possible phase space which results in captured positrons for three trapping fields

4.6 In-situ laser cleaning of transmission moderator

In earlier work, a Penning trap that had been consistently trapping positrons stopped accumulating once exposed to an antiproton beam. This was clearly a grave problem for the hopes of making antihydrogen in a single trapping system. Therefore, it was decided to determine the cause of this failure in order to avoid the same problem in the next generation of Penning traps.

Among the possible failure mechanisms were either "cleaning" or "coating" of the positron transmission moderator by the antiproton beam. In order to investigate the "cleaning", an optical fiber was brought into the Penning trap. Although optical fibers routinely carry light, there were many problems to overcome as this optical fiber had to make vacuum seals both at a room temperature junction and also in a 4.2 K environment and it had to carry large amounts of power into a vacuum environment. After trying many paths, a vacuum tight optical fiber was installed with a copper finger that helped keep the fiber tip from melting as the light was pulsed through it.

As the previous work showed that cycling of the Penning trap to room temperature restored the positron loading at least on a temporary basis, it was believed that as the transmission moderator cooled it cryopumped the residual gas left in the vacuum of the Penning trap critical to the formation of positronium. When the high energy antiproton beam passed through this foil the frozen gas layer would be slightly removed. Over time this gas layer would be "cleaned" off. Using the installed optical fiber to direct light on this same foil, we were able to do a controlled removal of the gas layer without the expense and difficulty of using an antiproton beam.

A 818 nm laser diode was chosen as the light source. Before pulsing the light on the transmission moderator, a positron loading rate curve was taken while varying the transmission moderator potential. This initial curve can be seen in Fig. 4-24.

As the light was brought in to clean the moderator the loading rate was indeed seen to diminish. This brought light to the previous failure and allowed the design of the next generation Penning trap to include a rotary electrode which would be able to block the antiproton beam from reaching the transmission moderator. Figure 4-25 shows the effect of increasing amounts of laser energy applied to the moderator and also the recovery of positron loading rate once the moderator was cycled to room temperature and back to 4.2 K.

4.7 Moderator treatment

The positron moderators used are tungsten single crystals. The moderators are treated in order to free them of impurities using a recipe that was developed elsewhere [37], but slightly modified. The moderator is suspended by thermally isolating, thin, tungsten wires in a vacuum chamber. An ordinary light bulb filament is placed next to the moderator and is used to produce an electron source which heats the moderator. In order to direct the electrons, the moderator is biased to 1 kV above the filament and a 150 gauss magnetic field is applied to focus the electron beam. The

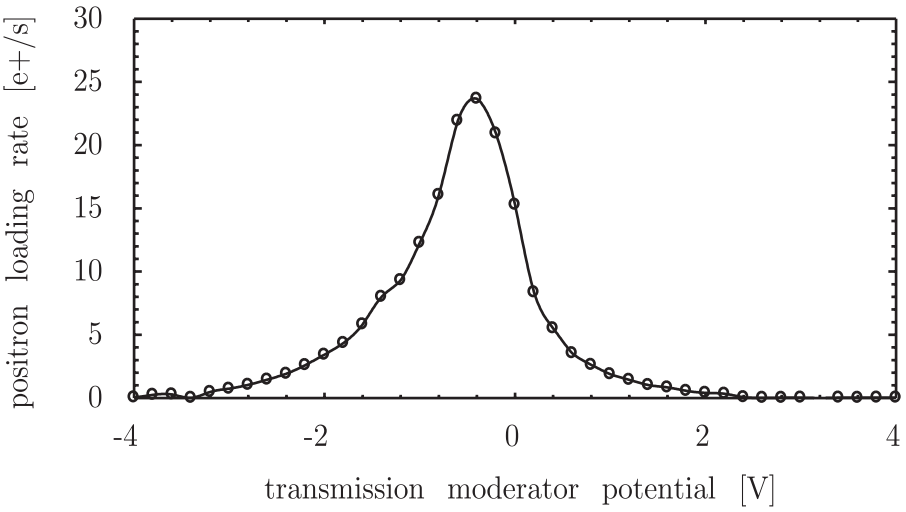

Figure 4-24: Loading rate as a function of transmission moderator potential before laser cleaning

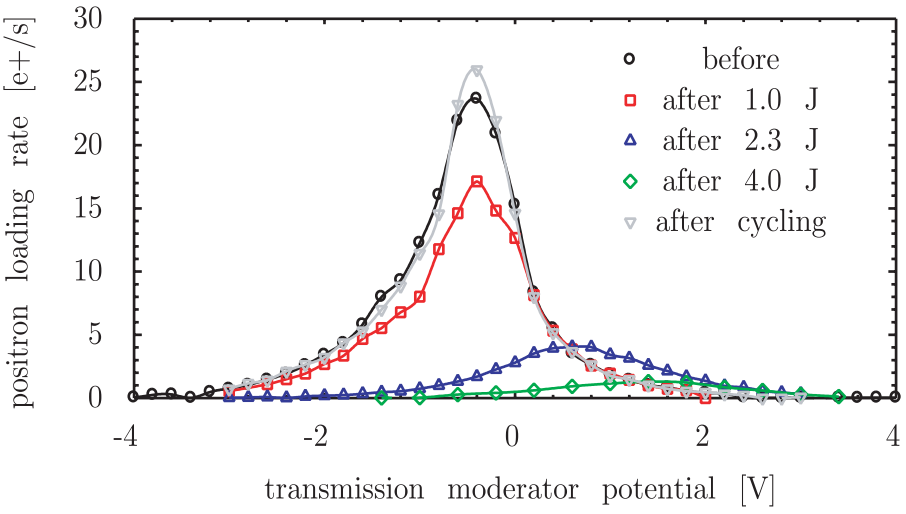

Figure 4-25: This graph shows the decrease of positron loading rate with application of laser light on the transmission moderator. Also shown is the recovery of the trapping rate once the Penning trap is cycled from 4.2 K to room temperature and back.

filament is powered with either an AC or DC voltage source. The vacuum chamber is evacuated to better than 0.2 μTorr and the filament slowly warmed. As the moderator heats, outgassing effects are seen, probably both from the moderator itself and the surrounding vacuum chamber. At temperatures above 1500 K, the moderator temperature is measured with a optical pyrometer. The treatment cycle employed, involved two alternating steps. The first was to inject oxygen into the chamber until a pressure of 1 μTorr was achieved, keeping the moderator at 1500 K. This was done for 30 minutes such that any surface contaminants would react with the oxygen, thereby forming an oxide layer. The next step was to stop the oxygen flow and hold the moderator at 2500 K for five minutes. This step serves two purposes, removing the oxide layer which would then be pumped away and allowing contaminants to move from the bulk to the surface where their concentration is now lower. The two steps were iterated five times. A schematic of the setup is shown in Fig. 4-26

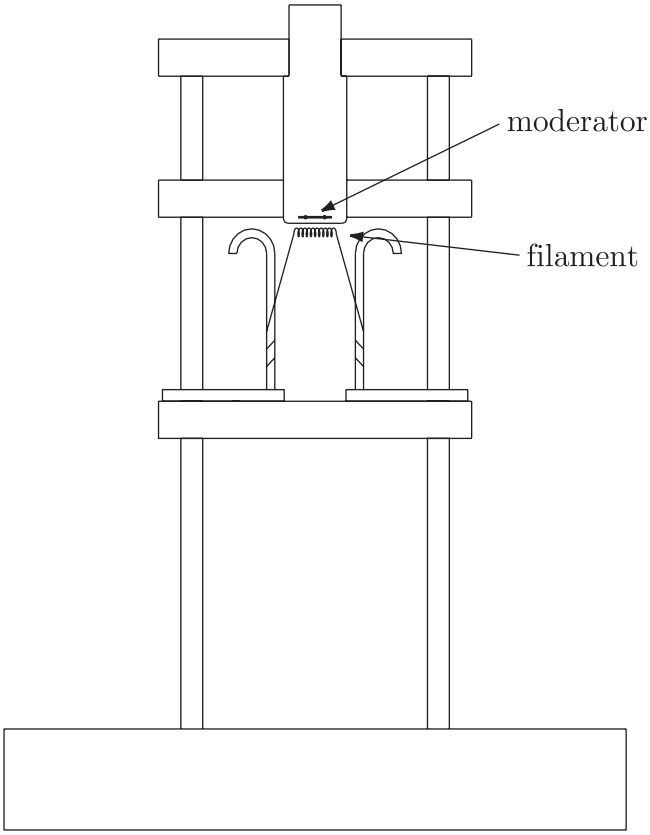

Figure 4-26: Setup to clean moderators

Chapter 5

Antiprotons

For antihydrogen experiments, the availability of antiprotons are essential and great lengths are taken to capture these particles. We have now shown that we can trap, cool, and stack antiprotons from the new Antiproton Decelerator (AD) facility. We accumulate these antiprotons in an extreme-high vacuum, 4.2 K, Penning trap. The antiprotons are created through high-energy collisions, then cooled by the AD, and pulsed to our experimental area. This chapter will discuss how we are able to capture these particles and our techniques to cool and stack them. This work builds upon techniques pioneered by the TRAP collaboration [3, 4, 5, 2].

In 1997, the European Organization for Nuclear Research (CERN) approved the construction of the AD. This new machine was to replace the Low Energy Antiproton Ring (LEAR) which had shut down at the end of 1996. The AD was designed to reduce the operational costs of delivering low energy antiprotons. The design goals [38] for the AD were 1.2×10^7, $100\,\mathrm{MeV}/c$, antiprotons delivered in $200 - 500\,\mathrm{ns}$ pulses with a $60\,\mathrm{s}$ cycle time.

To supply the AD, antiprotons are produced via collisions of 10^{13}, $26\,\mathrm{GeV}/c$ protons on an iridium target. Once produced, about 5×10^7 antiprotons are collected into the AD with a momentum of $3.57\,\mathrm{GeV}/c$. As the antiprotons circulate in the AD, two different cooling schemes are applied. Stochastic cooling is used on the antiprotons at $3.57\,\mathrm{GeV}/c$ and $2\,\mathrm{GeV}/c$ and then electron cooling at $300\,\mathrm{MeV}/c$ and then again at $100\,\mathrm{MeV}/c$. After cooling, a nominal bunch of 2×10^7 antiprotons are ejected to the experimental extraction lines. The AD facility can be seen in Fig. 5-1.

In July 2000, the Antiproton Decelerator (AD) began delivering low-energy antiprotons [39] to the ATRAP experiment. On July 18, the ATRAP collaboration trapped antiprotons coming from the AD for the first time. Fig. 5-2 shows the annihilation signal from these first trapped antiprotons. By the end of that day, antiprotons had also been cooled down to eV levels from their initial keV energies via interactions with cold (4.2 K) trapped electrons. We have since repeatedly demonstrated accumulation and electron cooling of antiprotons. We trap up to 12,000 antiprotons per 110 second AD cycle with cooling to sub-eV energies.

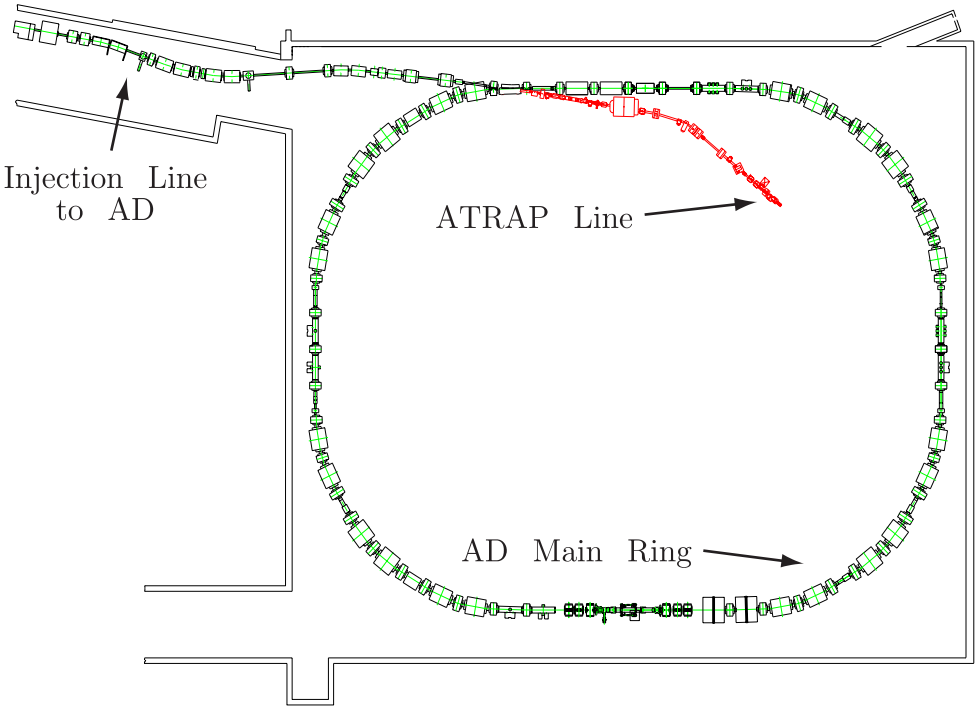

Figure 5-1: AD facility showing the injection line, the main AD ring, and the ATRAP extraction line. For simplicity other existing lines are not shown.

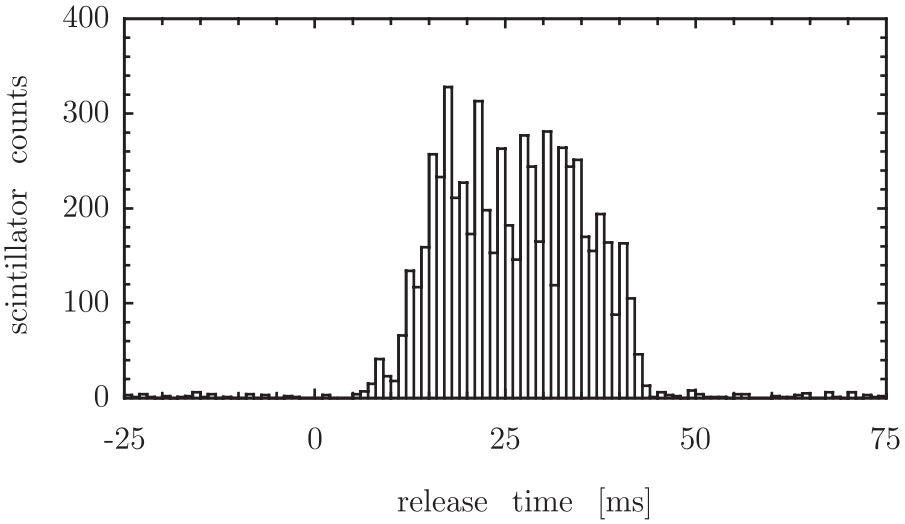

Figure 5-2: First trapped antiprotons at the AD. This figure shows the signal of the scintillation detectors as the 3 kV antiproton well is opened, allowing the antiprotons to escape and annihilate.

	DE0.QN10	DE0.BHZ12	DE0.BHZ18	DE0.QN20
Current [A]	1.73	99.50	176.00	-15.77
Tuning [A]				0.02
	DE0.QN30	DE0.DHZ35	DE0.DVT35	DE0.QN40
Current [A]	27.15	0.00	-0.50	18.00
Tuning [A]				2.00
	DE0.DHZ45	DE0.DVT45	DE0.QN50	DE0.QN60
Current [A]	-0.34	0.00	3.38	-4.34
Tuning [A]	0.10		0.02	0.02
	DE3.BVT10	DE3.QN20	DE3.BVT25	
Current [A]	-125.50	-7.01	-179.20	
Tuning [A]	0.25		0.80	

Table 5.1: Transfer line settings

5.1 Accumulating antiprotons in a Penning trap

After the antiprotons are ejected from the AD ring, they travel through a vacuum line, while being steered and focused by several magnets. Once the particles leave the AD extraction line, the beam intensity and position are nondestructively measured. The beam then passes through a gas cell reducing their energy by a small, but tunable amount. Finally, the antiprotons pass through two vacuum windows and an energy degrader, thereby entering the trapping region. Once inside the trap (see Fig 5-3), a time synchronized potential is quickly applied, trapping the antiprotons. A thorough understanding of each of the steps mentioned is crucial to the trapping of antiprotons.

5.1.1 Beam line elements

The AD extraction line is the link between the AD ring and the experimental areas. This vacuum line bring the antiprotons to the experimental areas, and also steers and focuses the beam. Some of these magnetic elements are represented in Fig. 5-4.

In addition to steering the beam for a particular experiment, the beam elements guide the beam between the experiments in the AD. There are three particular magnetic elements used to do this.

A typical antiproton run begins with switching the beam elements to allow the beam into the ATRAP experimental area, setting all the necessary magnets to the previous optimum settings and steering the beam. This process consumes anywhere from 10 to 30 minutes depending on the beam position fluctuations and the time since the previous run. Typical magnet settings can be seen in Table 5.1, where the tuning parameter is the characteristic change in magnet current needed to move or focus the beam. In order to minimize the beam steering time, a procedure was developed to quickly steer and focus the beam [40] which will only be outlined here.

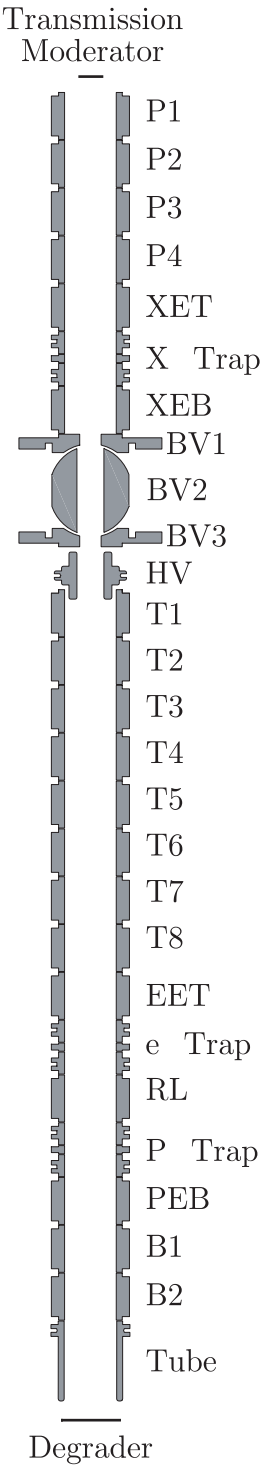

Figure 5-3: The electrodes of the Penning traps

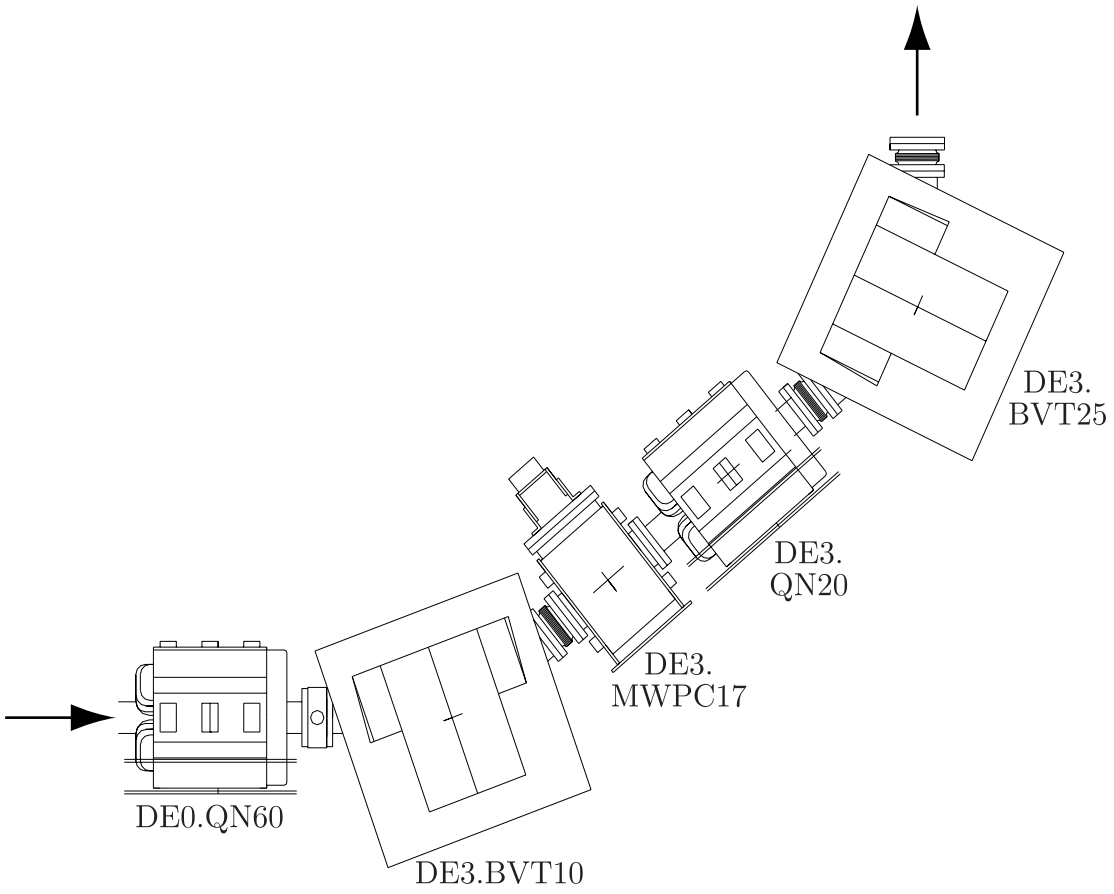

Figure 5-4: ATRAP extraction beam line showing a DE0 element and the complete DE3 line. This drawing includes quadrupole (QN), vertical bending magnets (BVT) and a wire chamber (MWPC).

gas	5% Methane & 95% Argon
pressure [mbar]	200
anode [V]	0
cathode [V]	-200

Table 5.2: Typical PPAC operating parameters

Assuming that the major beam line adjustments have already been done, usually with CERN/AD personnel, the beam preparation involves up to four magnets. The first adjustment to be made involves a horizontal tuning dipole, DE0.DHZ45, which is adjusted by its characteristic step size (see Table 5.1.) Once the beam is centered in this plane, the perpendicular direction is adjusted via DE3.BVT25, a vertical tuning dipole. This process is iterated until the beam is centered in both directions. At this point, the beam may have an unacceptably large diameter in either of the two major axis. Modification of the beam diameter is done with tuning quadrupoles, DE0.QN40 and DE0.QN50, which focus in the horizontal and vertical directions. These magnets can be adjusted in a manner similar to the steering dipoles.

5.1.2 Measuring antiproton beam intensity and position

Knowledge of the position and intensity of the antiproton beam is crucial for the capturing of antiprotons. The AD provides wire chambers in the transfer line but they provide neither an absolute particle number nor the required position resolution. In order to obtain this information, a parallel plate avalanche counter (PPAC) is used (see Fig. 5-5.)

The PPAC consists of two cells labeled ppac-x and ppac-y which measure beam position in each of the two directions perpendicular to the beam path. Each cell contains two plates, an anode and a cathode. The anode has five metallic strips which are mutually electrically isolated, while the cathode is fully conductive over its surface. Additionally, the cell has two gas lines through which a gas mixture flows. Typical operating parameters for the PPAC can be seen in Table 5.2.

As the antiprotons enter a PPAC cell, they collide and strip electrons from the argon atoms. The methane is used to quench secondary electron avalanches, by absorbing gamma rays, which are produced by the incoming antiproton beam. Currently, the PPAC is operated in the linear regime where the probability of a stripped electron further ionizing the gas is low. This mode gives signals which are proportional to the number of antiprotons passing through the cell. The free electrons are accelerated along the magnetic field direction by the electric field and are captured on one of the five strips of the anode. These signals are connected to a multichannel integrating ADC, which integrates only during beam extraction to minimize noise. The integration gate must be made long enough to accommodate the timing jitter of the antiproton beam. Typical beam timing jitter can be seen accompanied by the integrating gate in Fig. 5-6. Finally, the control computer reads out the ADCs and

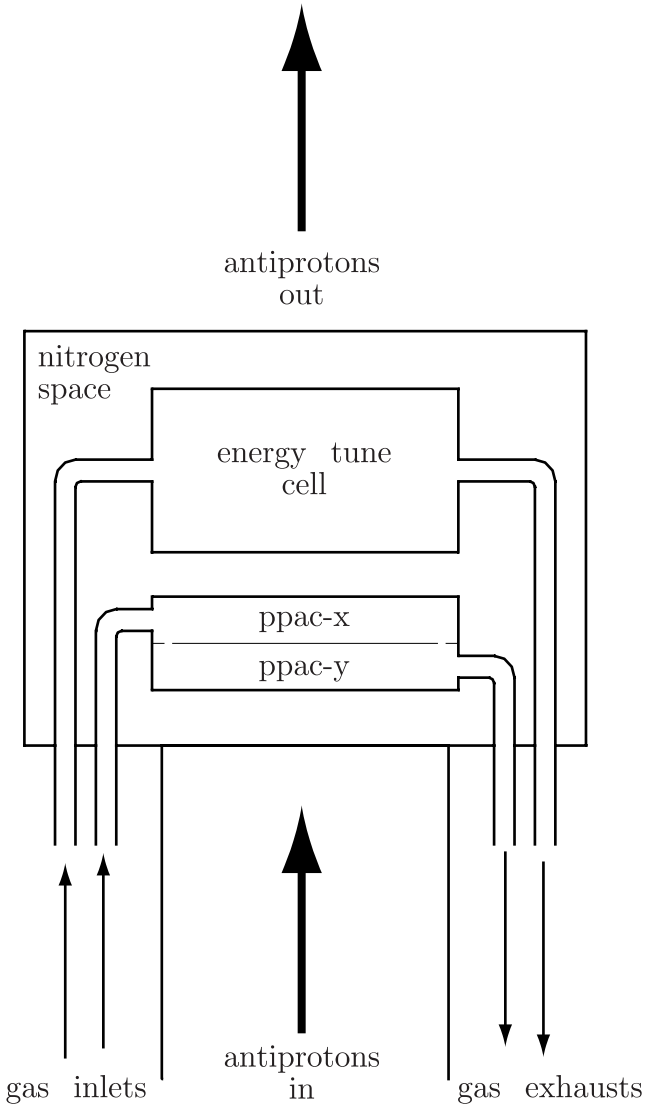

Figure 5-5: Schematic representation of PPAC showing the antiproton beam line, the ppac-x and ppac-y cells, the energy tuning cell, and externally available gas lines.

display a beam profile as seen in Fig. 5-7. A schematic representation of the PPAC electronic system is shown in Fig. 5-8.

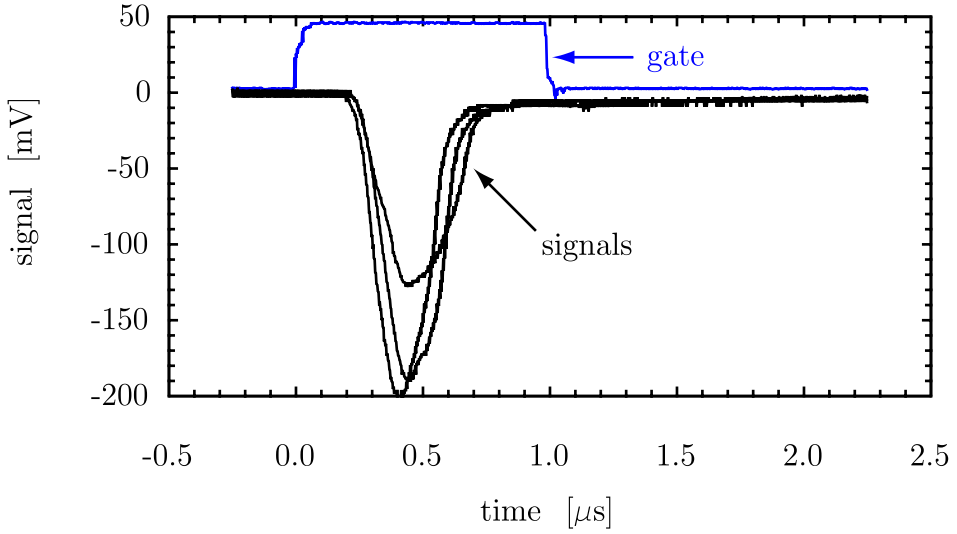

Figure 5-6: PPAC shot to shot jitter. This single channel data shows variation between shots.

The sum of all the PPAC detector channels is an indicator of the amount of beam entering the trapping region. Plotting this sum against the number of trapped antiprotons, see Fig. 5-9, shows that the PPAC can act as a normalizing detector, indicating the number of antiprotons trapped from any particular AD pulse.

5.1.3 Antiproton energy reduction

The antiprotons leaving the AD are cooled to a momentum of 100 MeV/c, which is a kinetic energy of 5.3 MeV. Since trapping charged particles requires voltages greater than the incoming energy, the trapping of these particles would require 5.3 MV if no slowing process were to take place. It is possible to slow down the antiprotons such that more manageable trapping voltages are used. The slowing of the particles takes place in two steps.

First, the antiproton beam passes through an adjustable gas mixture of helium and sulfur hexafluoride. The ratio of the two gases is variable and the the mass flows are controlled such that the total pressure of the cell is kept at one atmosphere. The total mass seen by the beam can be adjusted by more than a factor of 35 with a corresponding energy loss of 0.02 to 0.68 MeV. Since the incoming beam has a energy centered around 5.3 MeV, this loss is only a fine tuning and a more substantial loss must accompany it for trapping to occur.

After losing energy in the gas cell, the antiproton beam enters the trap enclosure and passes through a thin foil. (The beam actually passes through other materials. A review of these energy losses can be found elsewhere [41] and will not be mentioned

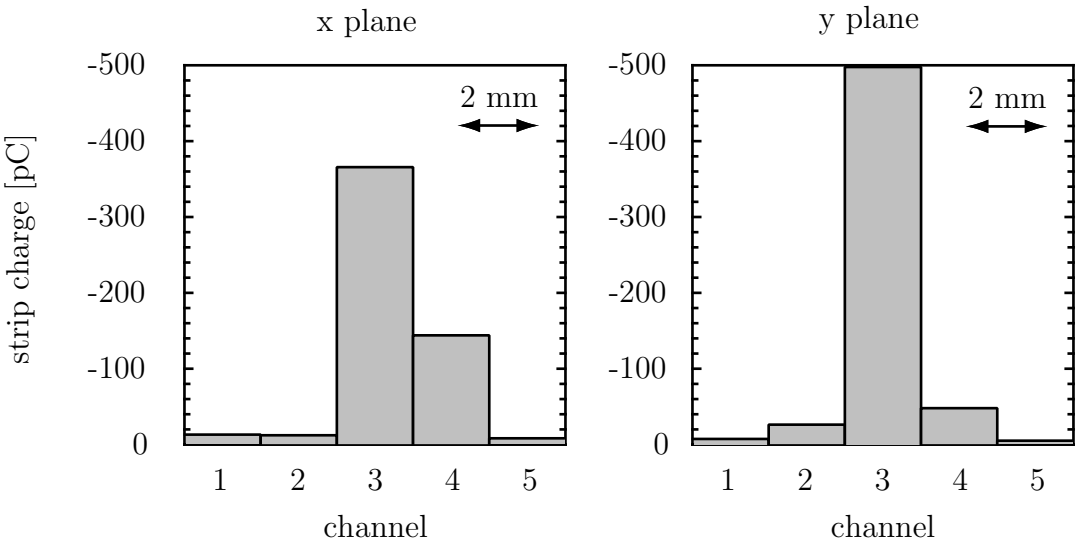

Figure 5-7: Typical antiproton beam profile

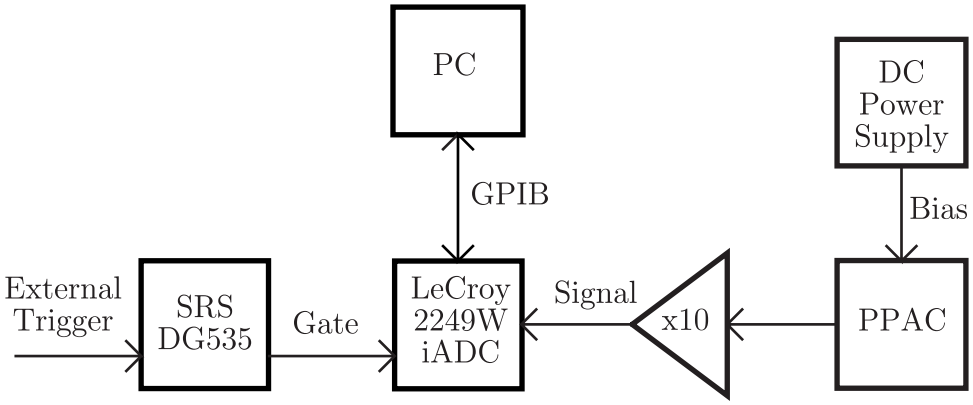

Figure 5-8: PPAC readout electronics

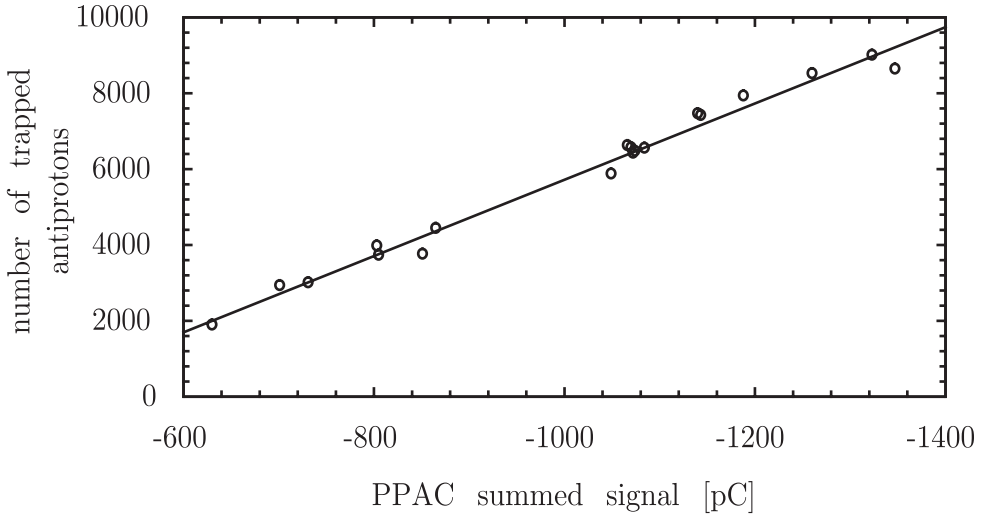

Figure 5-9: Fit of measurement of beam intensity to antiproton capture

further here.) This thin foil, referred to as the degrader, is a 125 μm thick beryllium crystal. The thickness of this foil is chosen such that a maximum number of antiprotons are slowed below the trapping voltage. If the foil is too thin, the antiprotons will emerge with enough energy that they will not be trapped by the keV voltages used to trap the particles. Conversely, if the foil is too thick, the antiprotons will stop within the degrader and annihilate.

5.2 Antiproton trapping

Now that the antiprotons have entered the Penning trap, and a fraction, typically 5×10^{-4}, have been slowed to kinetic energies on the order of keV, the particles are ready to be trapped. Trapping occurs when a time synchronized pulse closes the axial potential well, which is initially open on one end to allow the antiprotons to enter. A diagram of these events is shown in Fig. 5-10.

As the antiproton beam is delivered in a single pulse of only a few hundred nanoseconds every two minutes, the timing of their capture is crucial. This section presents a overview of the electronics used to control the antiproton capture timing. Figure 5-11 shows the most important devices which control the timing, while Fig. 5-12 shows a timing sequence.

The AD forewarning pulse, which arrives one second before the antiproton beam, turns on the HTS high voltage switch and inhibits the scintillation detectors. The HTS switch is used to quickly change the degrader from a positive voltage (trap open) to a negative voltage (trap closed). Because it produces RF noise, it is kept off as much as possible. The scintillation detector inhibit only functions for a few seconds, at which point the detectors come back on-line. Next, the AD warning pulse arrives triggering a delayed pulse which then triggers the HTS switch to close, trapping the

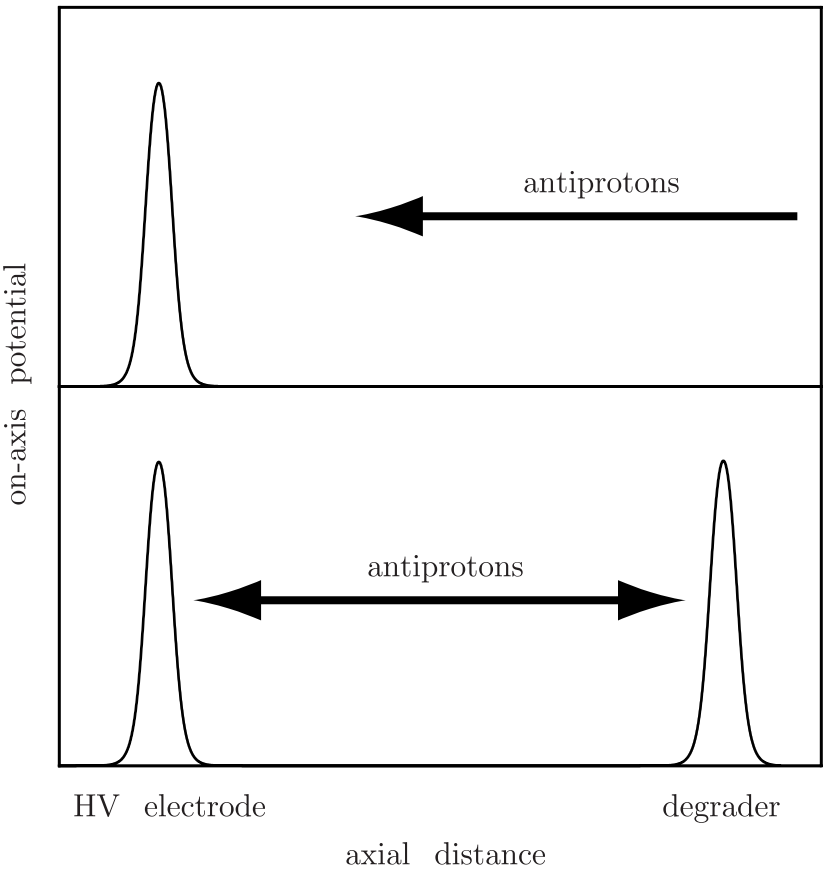

Figure 5-10: Diagram of antiproton trapping showing the antiprotons entering the trap with one end of the potential well in place. Once they are inside, the other end is quickly ramped up to the trapping voltage, holding the particles inside.

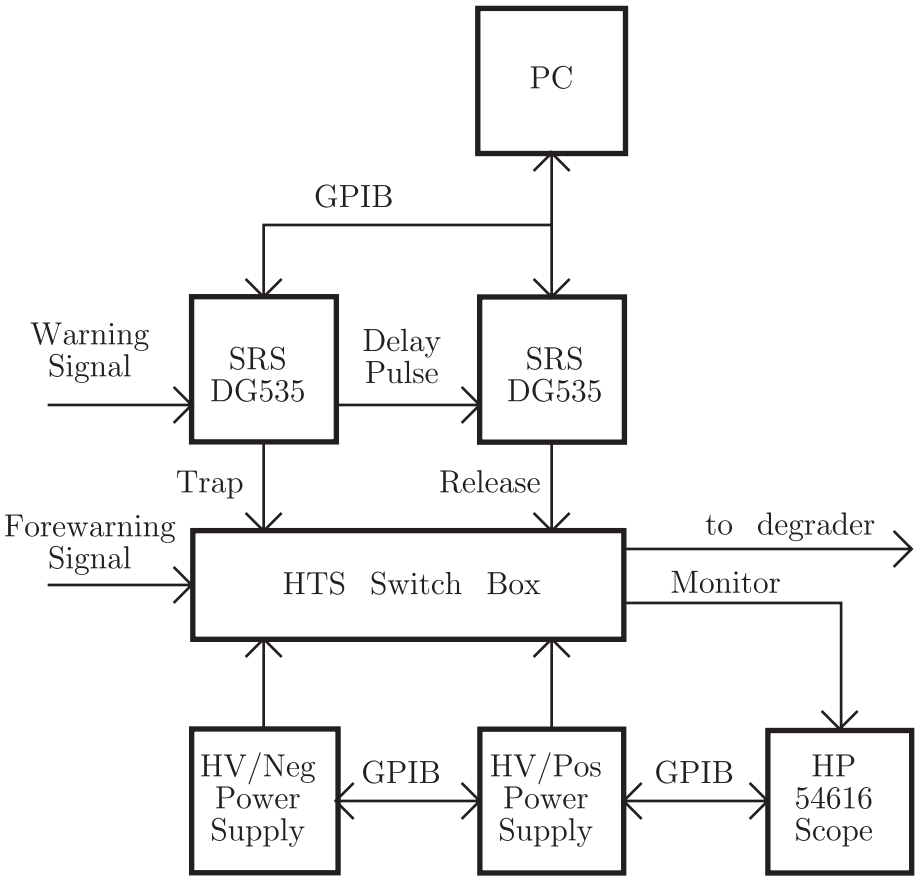

Figure 5-11: Control electronics of antiproton trapping. The AD provides both a forewarning and warning signal announcing the antiproton arrival. The forewarning signal comes one second before the beam and turns on the HTS switch box. The warning signal comes 2 microseconds before the beam, triggering the first of two delayed pulse generators. After a short programmable delay, the HTS switch is sent a trigger, switching the degrader to a negative power supply. When the particles are ready to be released from the high voltage well, a second signal is sent to the HTS to switch the degrader back to a small positive bias supply.

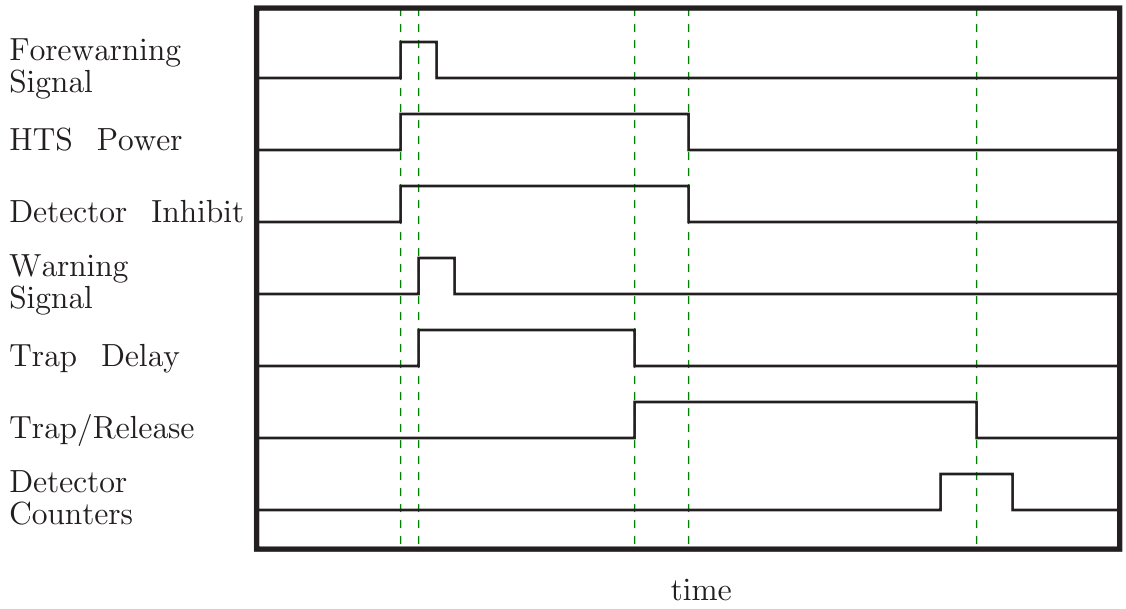

Figure 5-12: Schematic of antiproton trap and release timing

incoming antiprotons.

Signals derived from the AD warning pulse include a gate used by the PPAC integrating ADCs. The warning pulse also triggers a delayed pulse which is used for the release of the uncooled trapped antiprotons. This delayed pulse triggers the HTS switch to slowly bring the degrader voltage to a positive value.

As the HTS switch plays a critical role in antiproton trapping, it will be discussed in further detail. A schematic is shown in Fig. 5-13. The switch has three states. The first is the one pictured in Fig 5-13, with both switches open. Because the positive bias supply is removed from the circuit, the degrader is held steady at the negative trapping supply potential, as needed to keep antiprotons in the Penning trap. In order to analyze the energy of these antiprotons, one would like to slowly ramp the voltage from the negative trapping supply voltage to a positive value (see Fig. 5-14.) This is done by switching the reed relay to the closed position. Because of the 10 ms filter immediately following the reed relay this switching follows the function

$$V_{deg}(t) = V_{trap} + 0.9(V_{bias} - V_{trap})(1 - e^{-t/10ms}) \tag{5.1}$$

The reed relay is only closed when either a high voltage ramp or a setup of the HTS switch box has been called. Therefore once the high voltage ramp trigger goes to the off state, the reed relay will re-open sending the degrader back to the trapping supply voltage.

In order to prepare the Penning trap for antiproton trapping, a setup signal closes the reed relay. Once the antiprotons have entered the trap, a trigger is sent to close

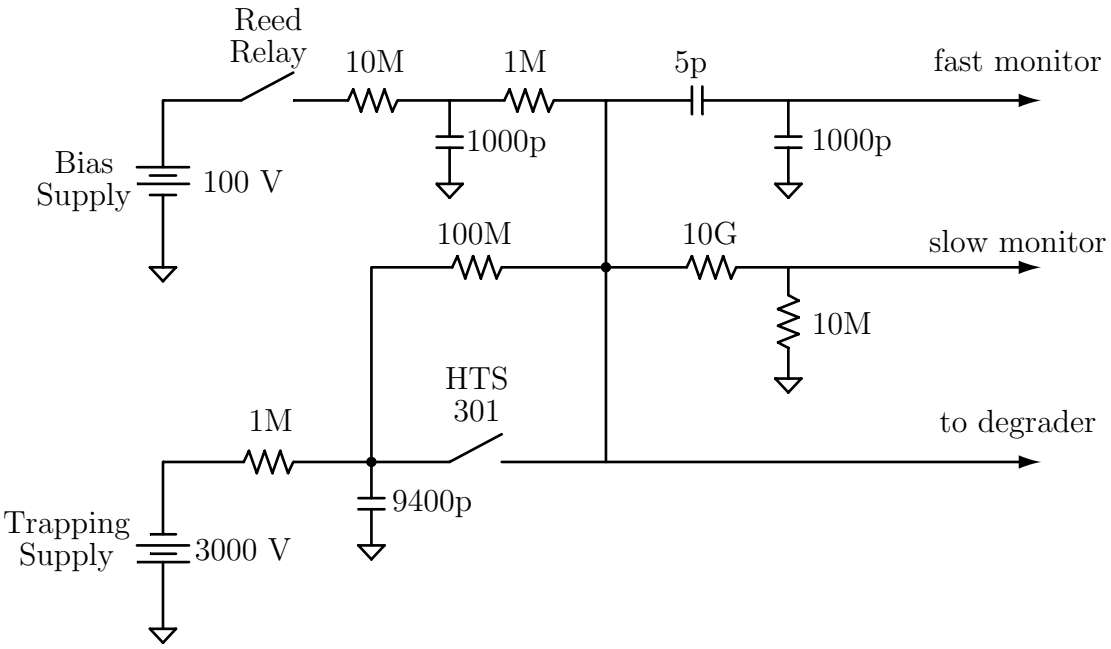

Figure 5-13: HTS switch box schematic

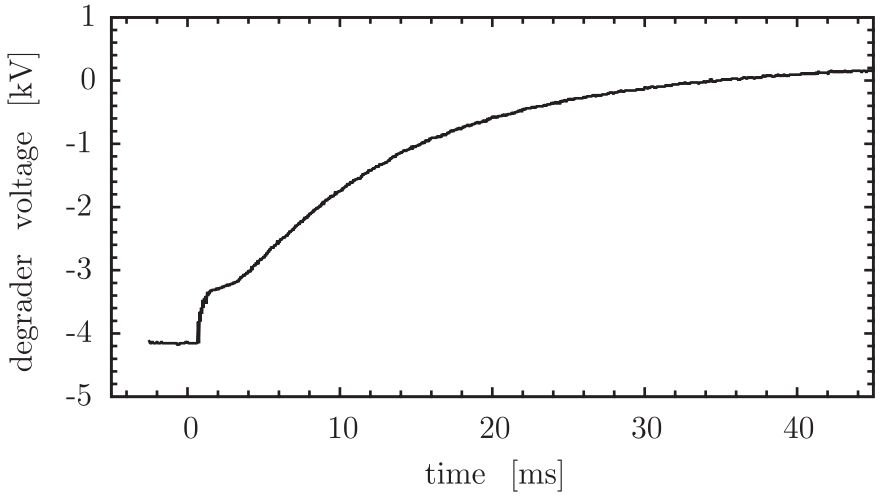

Figure 5-14: Potential on degrader electrode as the Penning trap is opened, slowly releasing the trapped antiprotons

the HTS 301 which quickly brings the degrader to the trapping supply voltage (see Fig. 5-15) The reed relay then opens, which has no effect at this point. After a few milliseconds the HTS 301 is turned off, which also acts to open this switch. This produces no change in voltage as the reed relay has already been opened, leaving the degrader at the negative trapping voltage.

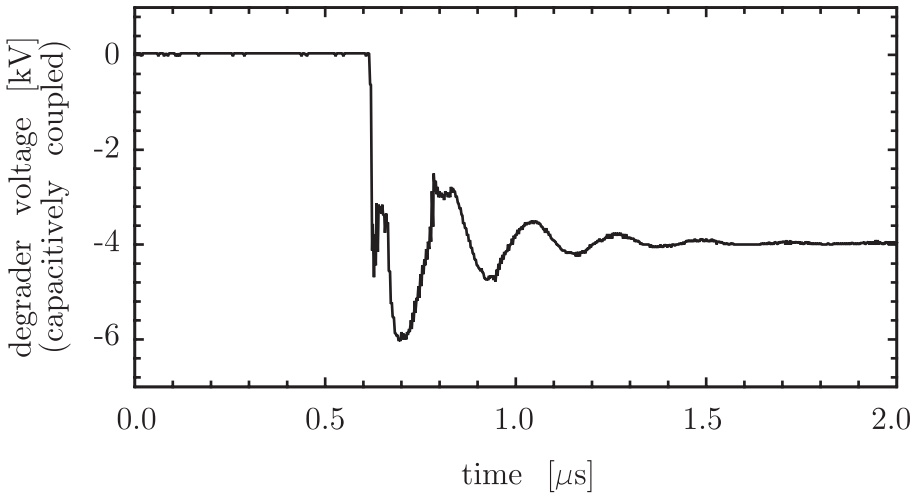

Figure 5-15: Fast monitor signal of degrader electrode as the Penning trap is closed, trapping the antiprotons. The line shows ringing effects due to impedance mismatch.

The switching of the degrader to the negative trapping voltage must happen quickly but it must also happen at an accurate time after the antiprotons have entered the trap. The AD provides the experiment with a warning pulse at a fixed time before the beam is to be extracted. This pulse is used to trigger a delayed pulse which triggers the HTS switch box. As expected, varying this delay changes the number of trapped antiprotons which can be seen in Fig. 5-16.

5.2.1 Antiproton energy tuning

As it is experimentally difficult to change the thickness of the cold degrader in the trap enclosure, the variable gas cell is used for fine tuning the final particle energy distribution. This tuning varies the trapping efficiency as shown in Fig. 5-17. When tuning the gas cell the total pressure of the cell is held constant at one atmosphere while the relative ratio of SF_6 to He is changed.

Although the peak of the energy tuning curve was never seen to move, it is possible that the ability to tune the energy curve could provide the ability to "tune out" any frozen gas layers that can freeze onto any of the vacuum windows of the trap system.

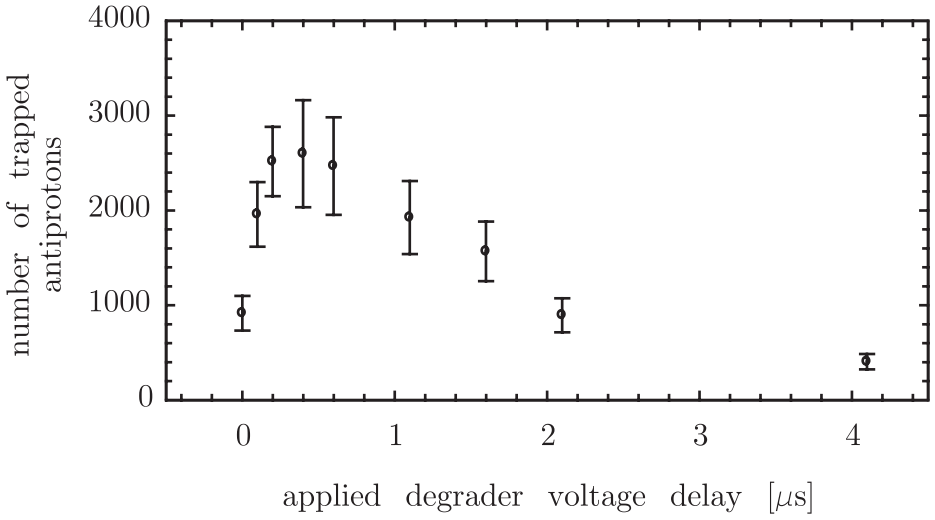

Figure 5-16: Number of antiprotons captured as a function of switch delay

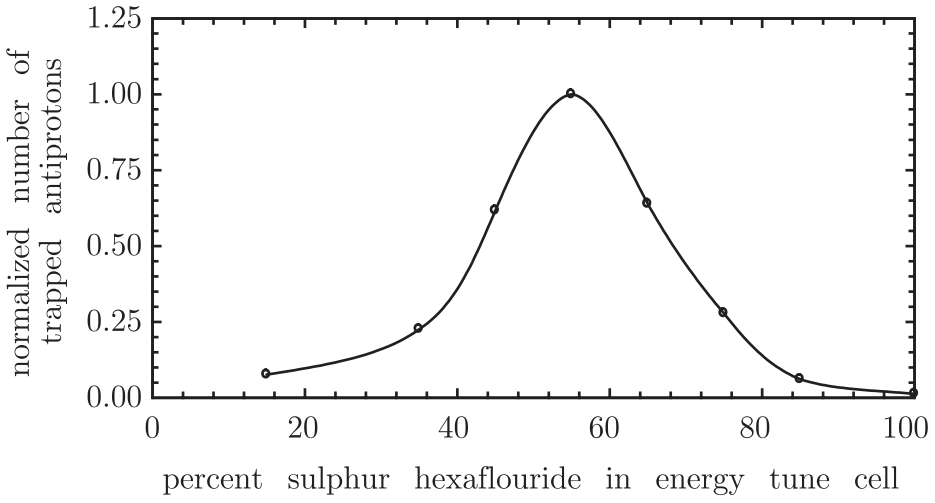

Figure 5-17: Efficiency of antiproton trapping as a function of SF_6 ratio

5.2.2 Analysis of the antiproton energy distribution

Once antiprotons have been trapped it is necessary to confirm they are indeed there. One method is to slowly bring the degrader from its negative trapping voltage to a positive bias. In order to synchronize the changing voltage with the signals seen on the scintillation detectors, a common clock is used. When the dumping sequence is to begin, a signal is sent to begin a clock signal. This clock starts the single channel scalers used to look at various logic combinations of the detectors. After a defined delay, the HTS switch box is triggered to switch the degrader to a positive bias while an oscilloscope records the voltage on the degrader through a slow monitor. As the degrader voltage and detectors signal are measured as functions of time, they can be combined to produce a single display of particle energy as seen in Fig. 5-18.

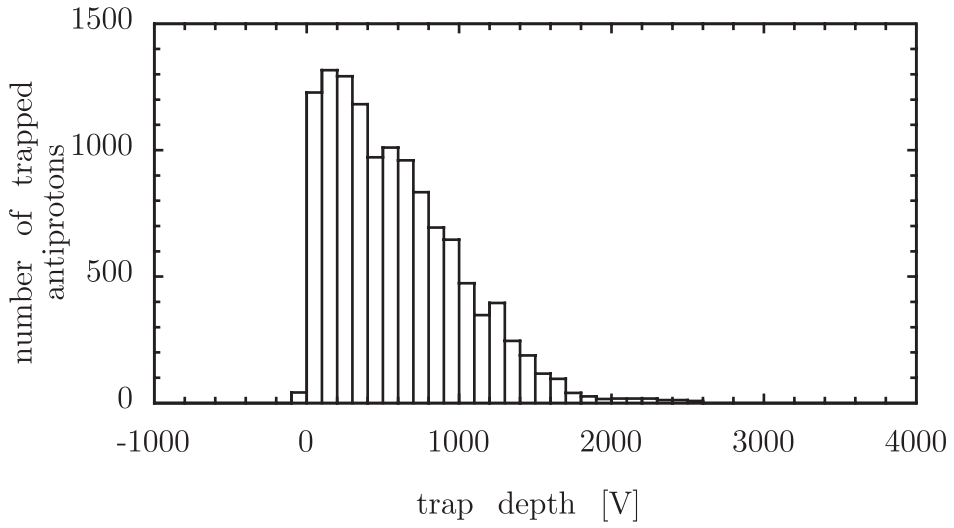

Figure 5-18: Energy spectrum of more than 12,000 uncooled antiprotons trapped in a single AD extraction.

5.3 Electron cooling

The antiprotons cool to eV energies via collisions with electrons. The electrons are preloaded into single or multiple wells in the Penning trap, before the antiprotons are caught. These electrons cool quickly into equilibrium with the 4 K environment via cyclotron radiation. Once the antiprotons are trapped in the long well between the HV and degrader electrodes, they have repeated collisions with the electrons. As an antiproton collides with an electron, the antiproton will have a small energy loss and the electron, although heated, will radiate away its energy. After multiple collisions the antiprotons will cool into the electron wells. With multiple wells and 100 s cooling times, near 100% cooling efficiencies are routinely seen. After cooling, the degrader is brought down from its initial voltage to release any antiprotons which have not

been cooled down into one of the trapping wells. The few particles which remain (approximatively 1%) have very low energies compared to the initial distribution as seen in Fig. 5-19.

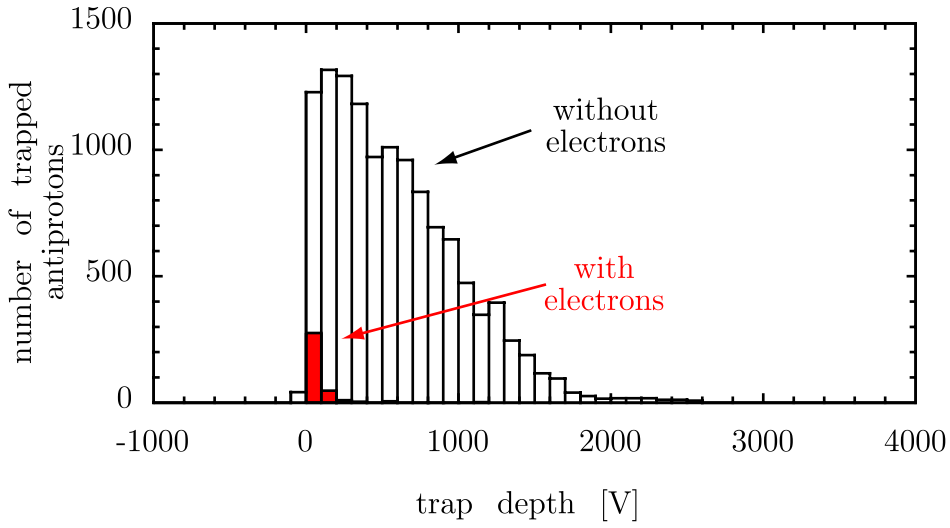

Figure 5-19: Energy spectrum of cooled antiprotons not trapped in the electron wells. Also shown is a data set from trapped uncooled antiprotons for comparison.

Since it was normal to trap the antiprotons in multiple wells the next step was to combine the particles into one well. This is done using slow changes in the well structure to move the particles axially. This process was previously developed [32] and implemented without change. Once the particles were combined, the well could then be slowly shallowed down to release the particles. In this way, we could determine the energy distribution of the trapped cooled antiprotons as illustrated in Fig. 5-20.

5.4 Electron ejection

After the antiprotons have been cooled and combined, the cooling electrons are ejected. The goal of many antiproton experiments was the combination with positrons, therefore the presence of electrons could not be tolerated. In practice two different ejection procedures were used.

The first technique was the pulsing open of the trapping well long enough to allow the electrons to escape but not the antiprotons. A typical well structure is shown in Fig. 5-21. As the velocity of electrons is approximatively 40 times greater at the same temperature, electrons can escape from a well before antiprotons are able to leave.

The second technique is used when the antiprotons are to be injected into a long well. The initial well structure can be seen in Fig. 5-22. The antiprotons and electrons are trapped together on electrode EET. Electrodes T3 and T8 are then pulsed down and the particles then move towards T3. Again, as the electrons are much lighter,

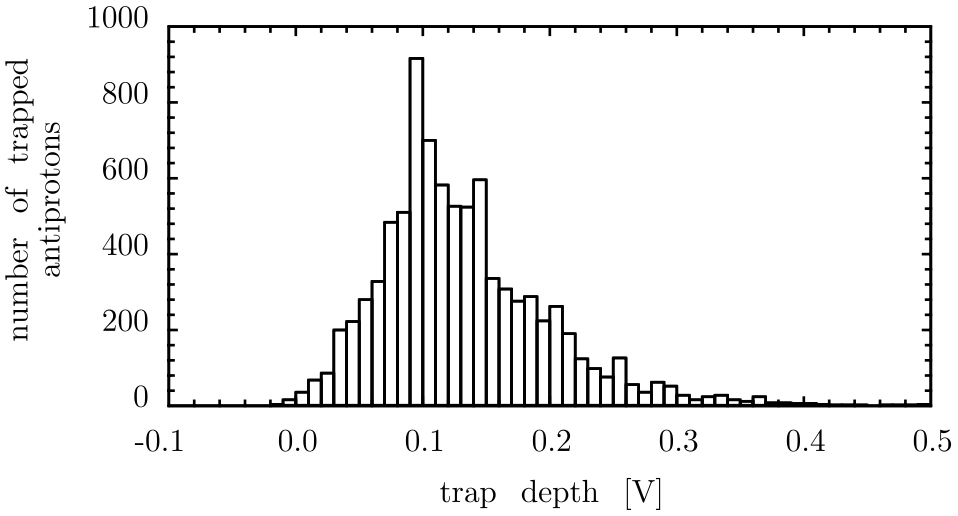

Figure 5-20: Energy spectrum of approximatively 9,000 cooled trapped antiprotons which were held in a 5 V well. The well was slowly raised through zero to energy analyze the particles.

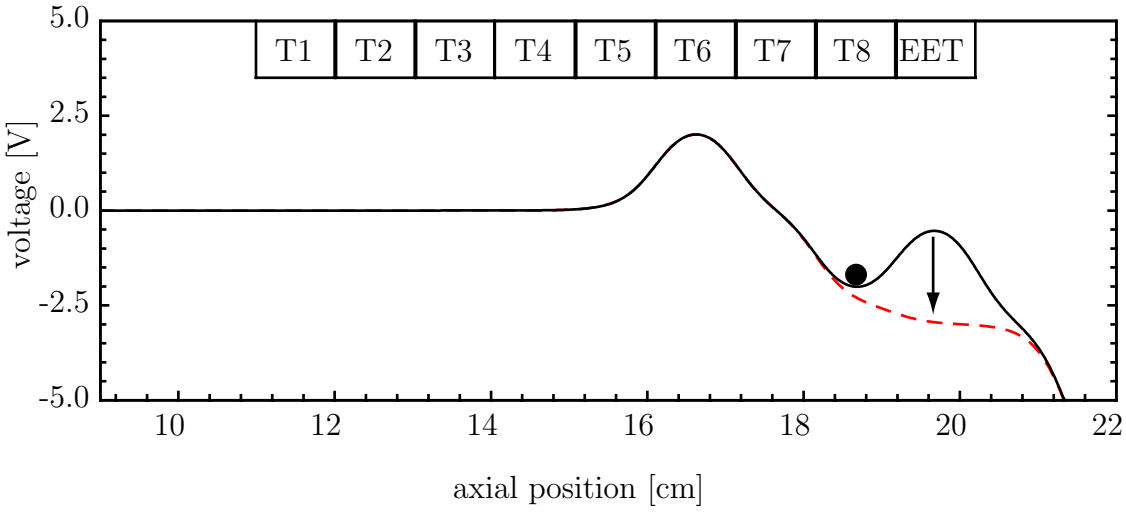

Figure 5-21: Typical well structure used to remove electrons from trapped antiprotons. This figure shows a potential well which originally holds both antiprotons and cooling electrons. A pulse is applied to the EET electrode which opens the well on one side such that particles can escape. As the pulse is of short duration only the electrons escape, leaving the antiprotons alone as the well closes shut.

they will reach the T3 electrode first. By correctly biasing electrodes further away, the electrons enter into the ball valve set of electrodes and do not return. Once the antiprotons are half way to the T3 electrode, the T3 voltage is pulsed back. Once the antiprotons reach the T3 electrode, the T8 electrode is pulsed back, leaving the antiprotons trapped in this long well free of electrons.

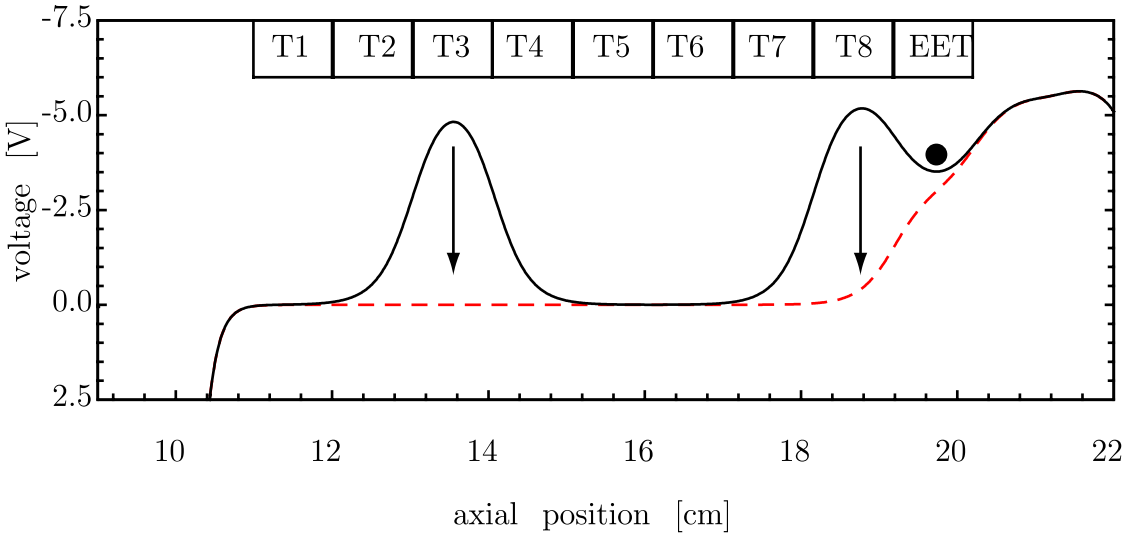

Figure 5-22: Long well used to pulse out electrons. In this scheme the T3 and T8 electrodes are pulsed down (represent by arrows) to allow the antiprotons and electrons to exit the original EET well. As the electrons will move faster than antiprotons, they will leave the trap and be collected further away. When the antiprotons reach the midway point between the T3 and T8 electrodes, the T3 electrode is brought back to keep the antiprotons trapped. As the antiprotons reach T3, T8 is pulsed back trapping only the antiprotons in the long well.

Chapter 6

Combining positrons and antiprotons

During the four month long, year 2000 beam run we began trapping, cooling, and stacking antiprotons. As antiprotons are only available during such a short period, we decided to push forward the antiproton/positron interaction experiments. We performed initial studies into both three-body recombination and pulsed-field recombination techniques. During the last night of the year 2000 beam, we focused on positron cooling of antiprotons and saw cooling [7].

Making antihydrogen requires combining a single positron with a single antiproton into a bound state. Although this is made easier by the opposite charges of the particles, there is still the problem of removing energy. If two particles are initially not bound, the total energy of the system is positive and it is not possible for them to bind together without additional means. Two particular methods which we initially investaged for removing the "extra" energy will be discussed here. Three-body recombination relies on a third particle to carry away energy and momentum leaving a bound antihydrogen atom. As a first step, we have demonstrated the first cooling of antiprotons with positrons in a configuration compatible with three-body recombination. A second method is the use of an external field to allow a positron to enter near an antiproton. Once the positron is deep in the potential well of the antiproton the field is removed, thereby binding the particles together. This pulsed-field recombination [42] has been shown to work on other systems and we began initial exploration of this method, demonstrating that we could do the nanosecond pulsing that is required.

6.1 Three-body recombination

Three-body recombination of antihydrogen can be written as

$$\bar{\mathrm{P}} + \mathrm{e}^+ + \mathrm{e}^+ \rightarrow \bar{\mathrm{H}}^* + \mathrm{e}^+$$

The antiproton and a positron become bound to form an antihydrogen atom while the other positron carries away the excess energy and momentum. Calculations for the

matter version of this process [8, 9], with a correction for strong magnetic fields [10, 11, 12], give a recombination rate per antiproton of

$$\Gamma = 6 \times 10^{-13} \left(\frac{4.2}{T}\right)^{9/2} n_e^2 s^{-1} \tag{6.1}$$

where T is the positron temperature in Kelvin and n_e is the positron density in cm^{-3}. Assuming a positron temperature of 4.2 K and a density of 10^7 gives a recombination rate of 50 $\bar{H}$ s^{-1}.

Antihydrogen must either be formed or deexcited to a tightly bound state so that it is not ionized by the electric fields which are needed to create the nested well. A study [12] has shown that this can indeed be the case for a sufficiently long interaction region.

6.1.1 Antiprotons in a long well

A first step towards three body recombination is the injection of antiprotons into the long well represented in Fig. 6-1. The antiprotons should remain trapped in the well with their original injection energies. After the antiprotons are loaded into the long well, it is slowly opened on one side to energy analyze exiting particles. (Antiprotons are placed into the long well by the quick pulsing (< 10 ns) of one side of the initial contament well.) A spectrum of antiprotons ejected from the long well can be seen in Fig. 6-2.

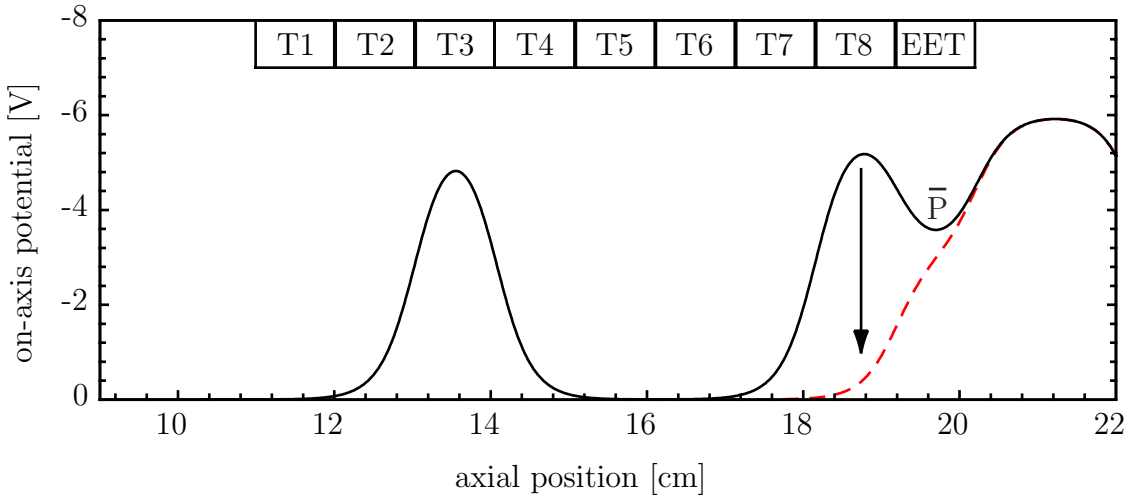

Figure 6-1: Electrostatic potential well used to pulse antiprotons into a long well. As the T8 electrode is pulsed quickly compared to the time needed for the antiprotons to move, the antiprotons are released with their original kinetic energy and a reduced potential energy. The voltages implemented are as follows: T3=-6V, T8=-6V/0V, EET=-3V, ER=-6V, and RL=-6V.

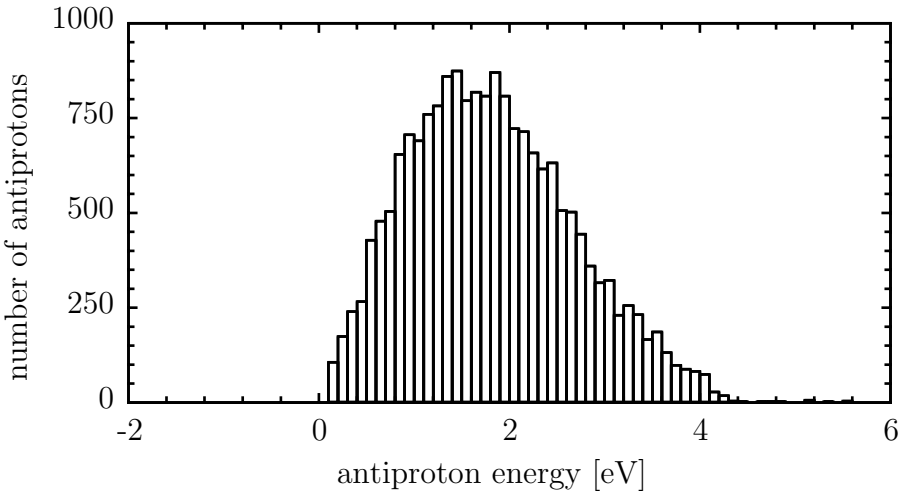

Figure 6-2: Energy distribution of antiprotons injected into the long well of Fig. 6-1.

The energy distribution of the antiprotons is low compared to what is expected. One effect which needs to be taken into account is the spread in energy of the antiprotons as they are launched. Assuming the antiprotons had up to 1 eV of axial energy, they would fall in energy as the well was opened. This concept is shown in Fig. 6-3. As the ac pulsing to open the well may have large amounts of "line ringing", there is some uncertainty in the initial distribution of injected antiprotons.

The other factor which should be considered is the energy loss as one potential is slowly ramped. The antiprotons oscillate in the long well and therefore sample the time-varying potential. Figure 6-4 shows a 1-dimensional simulation of the energy loss in this process as one end is linearly ramped down slowly compared to the particle movement time. Using the conditions of this experiment, a 3 eV antiproton (energy measured from 0 V potential of the long-well) would experience an energy loss of approximatively 7% (which has been taken in account for Fig. 6-2.)

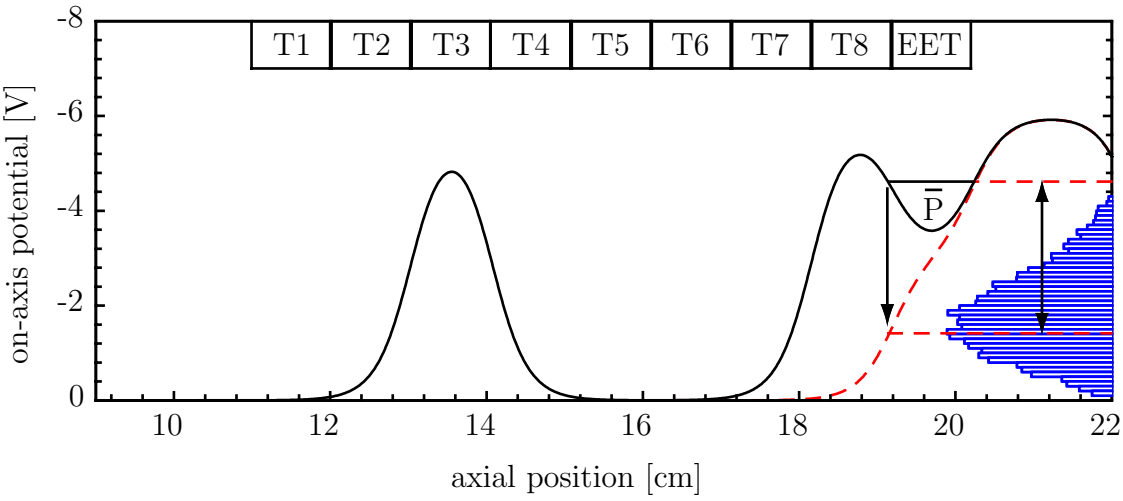

Figure 6-3: Electrostatic potential well showing distribution of initial energies. The antiprotons are assumed to have an initial axial energy up to 1 eV (represented by the solid line above the initial well.) As the well is quickly pulsed open the antiproton energy spread increases to the 3.2 eV. The antiproton data is included on the graph for comparison.

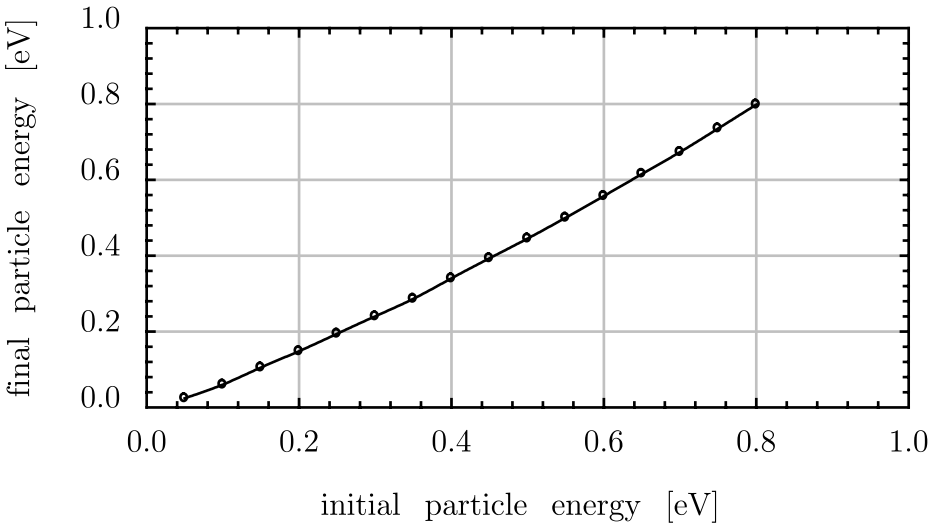

Figure 6-4: Adiabatic cooling of an antiproton in the long well of Fig. 6-1. This numerical simulation shows the cooling effect of particles in a long well as one of the ends is slowly ramped down. The simulation was performed using a well of the T3 and T8 electrodes with 1 V applied to each electrode. (Applying 1 V to a single electrode produces a voltage of 0.8 V in the center of the trap, limiting the maximum energy particle able to be trapped.)

Another data set was taken to understand the apparent energy loss of the antiprotons. In this experiment, the antiprotons were raised higher in energy to measure the variation of loss with initial energy. This data can be seen in Fig. 6-5. It is interesting to note that the antiprotons are seen to be raised in energy compared to the previous experiment. In fact the energy width with respect to the expected minimum energy point seems to be consistent in the two cases.

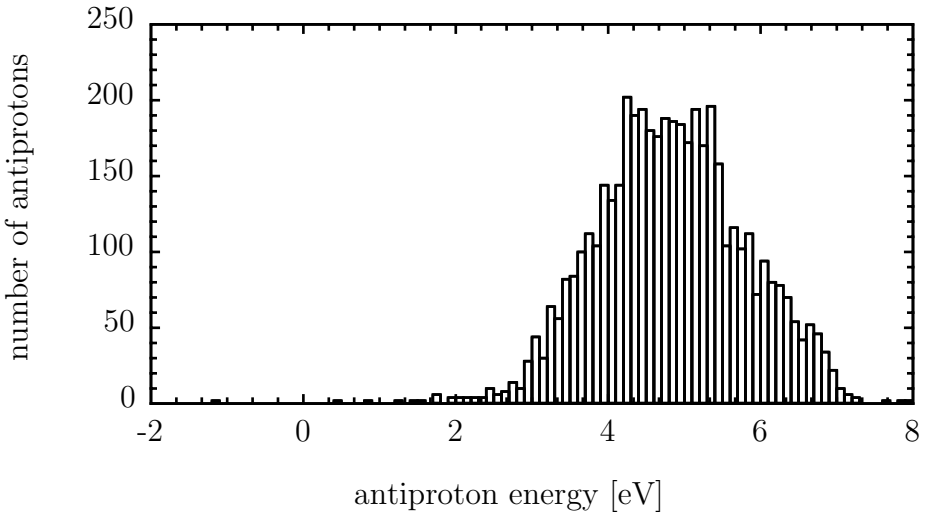

Figure 6-5: Energy distribution of antiprotons in a long well. The voltages implemented are as follows: T3=-10V, T8=-10V/-4V, EET=-7V, ER=-10V, and RL=-10V.

It is assumed that after careful studies are performed, this initial energy distribution of the antiprotons will be measured. As time limits did not permit this before, it will remain as an invitation to following researchers.

6.1.2 Positron cooling of antiprotons

Using a nested Penning trap configuration, antiprotons were shown to cool via interactions with positrons. This was seen when the antiprotons which nominally remain at their initial injection energy in the absence of positrons, were cooled when the two species were combined.

A plot of the on-axis potential of a nested well is shown in Fig. 6-6. In this configuration, positrons (when used) are placed in a single electrode well at T6. The antiprotons are then injected in a larger nested well (consisting of five electrodes in this case) with an energy higher than that of the positrons. As the antiprotons oscillate through the positron cloud, they transfer energy to the positrons which are kept in thermal equilibrium with the 4 K environment via cyclotron radiation.

After a variable interaction time, the nested well is opened on one end and the antiproton energy distribution is measured. Because of experimental constraints, the

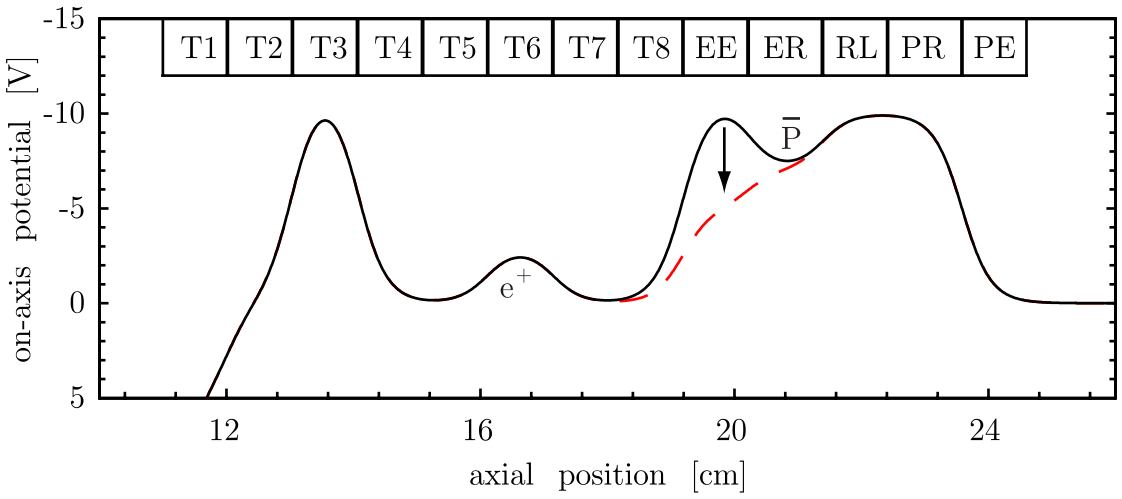

Figure 6-6: Electrostatic potential of nested well for combining antiprotons and positrons

cooled antiprotons which become trapped on the other half of the nested well were not measured as a function of energy. The number of antiprotons trapped on the far side were approximately 65% of the energy analyzed total. Data showing the effect of interaction time is shown in Fig. 6-7

As the positrons seem to be cooling the antiprotons to nearly zero axial energy, the effect of changing the positron well depth was investigated. A plot of the potential of a deeper well is shown in Fig. 6-8 where the positron well depth is now an applied 5 V compared to 3 V used before.

Antiprotons were then injected into a nested well with a 3 V and then a 5 V positron well while the interaction time was fixed at 40 s. Figure 6-9 clearly shows that the antiproton final energy depends on the depth of the positron well.

6.2 Pulsed field recombination

Pulsed field recombination is a technique to combine a negative ion (antiproton) and an electron (positron) using a time-dependent external electric field to form a bound atom (anti-atom). Looking at Fig. 6-10, one can see that applying an external electric field reduces the potential energy on one side of the antiproton, allowing a particle to enter closer to the nucleus. If the external field is switched off while the particle is in the newly accessible region, then it may be trapped. The trapping depends on the particle's kinetic energy and radial position.

Implementing pulsed field recombination requires the opening of the potential well as above and also the ability to move the two species of particles together. Penning traps are well suited for both these requirements. The sequence of steps used can be seen in Fig. 6-11.

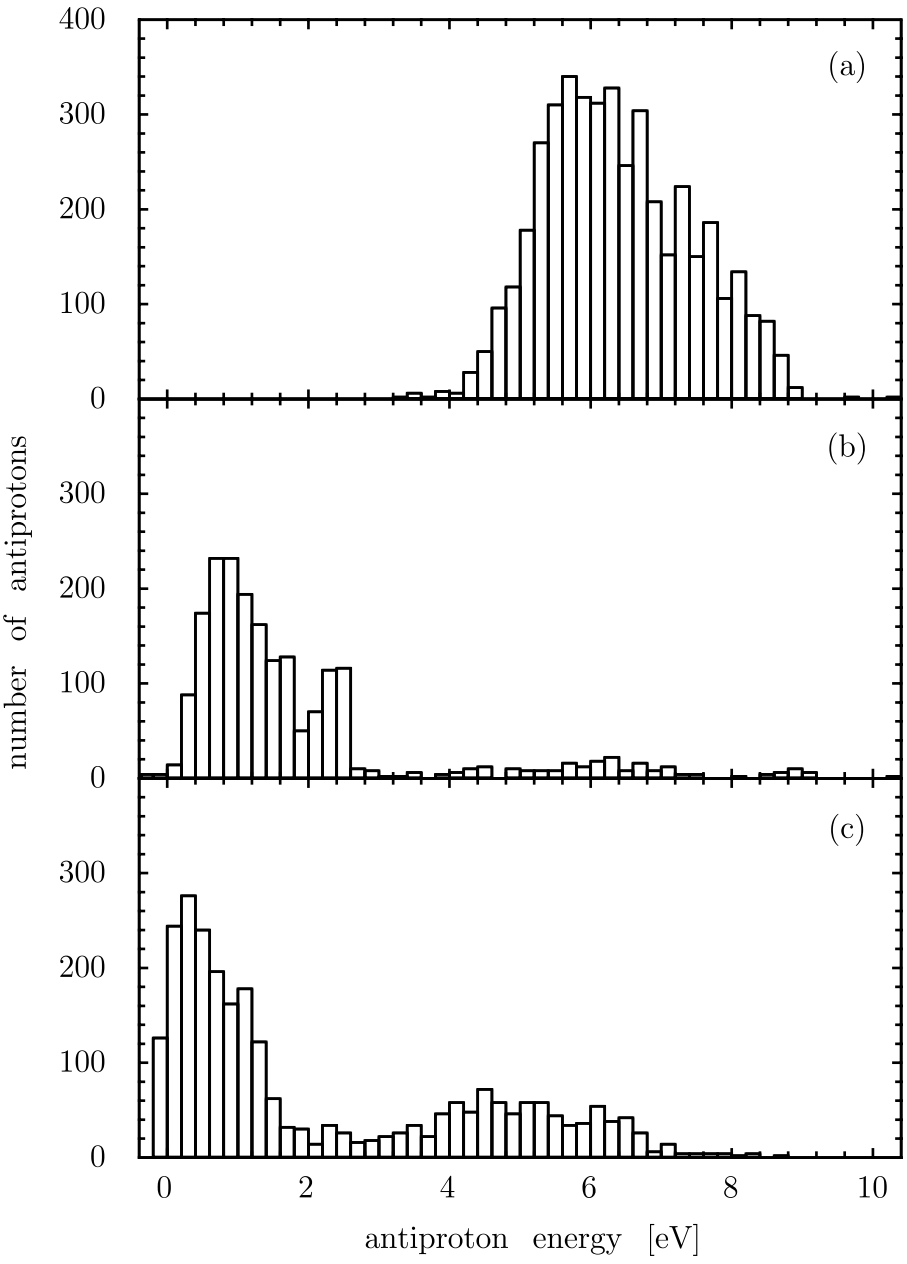

Figure 6-7: Positron cooling of antiprotons for different interaction times. The uncooled spectrum (a) is shown along with cooling times of 20 s (b) and 120 s (c).

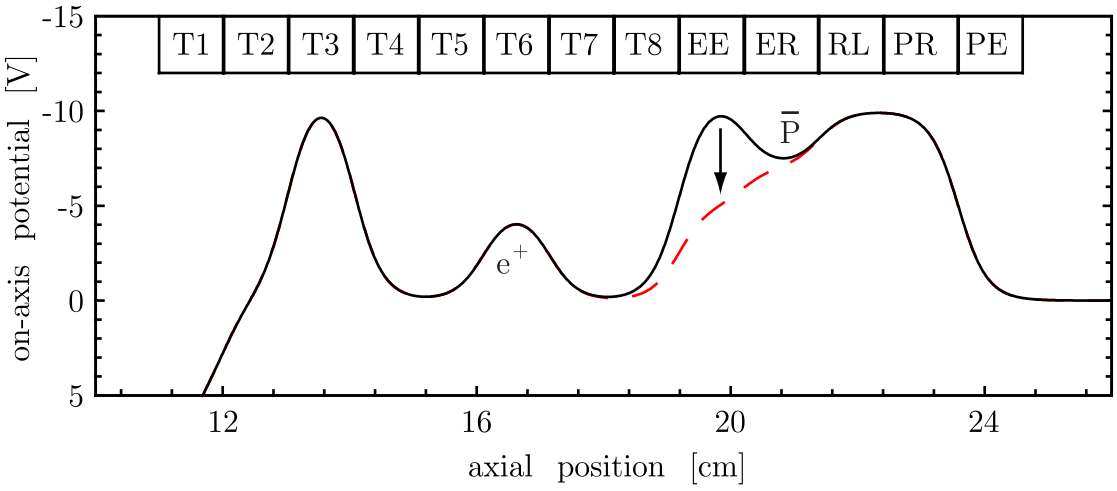

Figure 6-8: Electrostatic potential of nested well for combining antiprotons and positrons with deep positron well

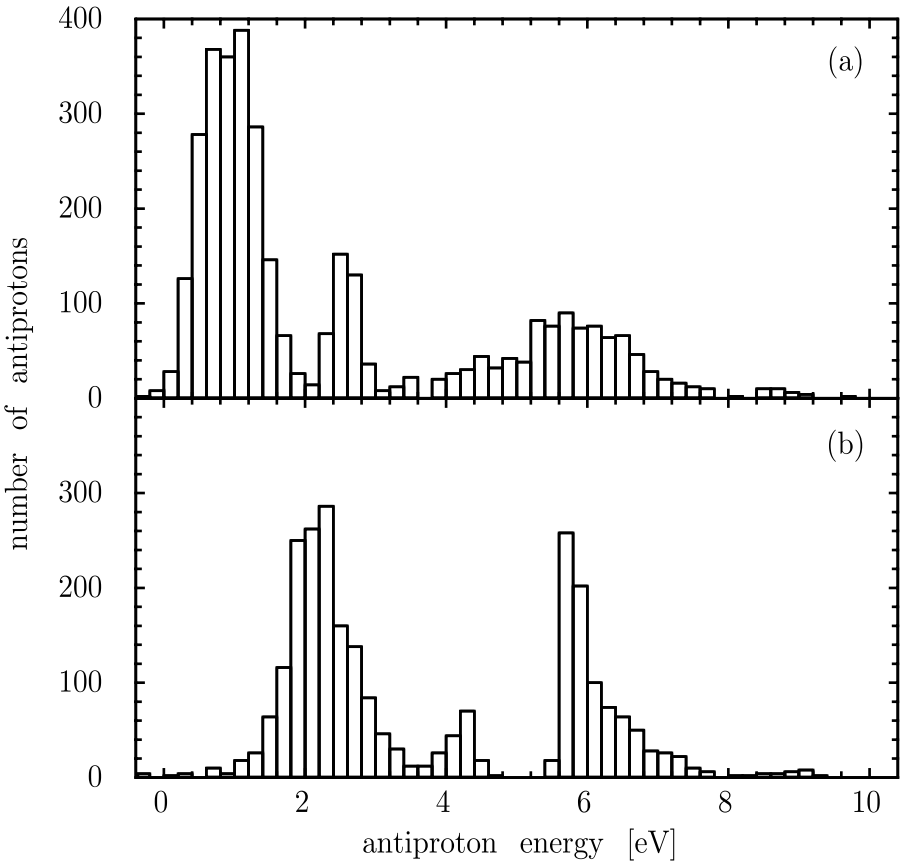

Figure 6-9: Positron cooling of antiprotons for different positron well depths. The antiprotons are seen to interact with positrons in a 3 V (a) and 5 V (b) well.

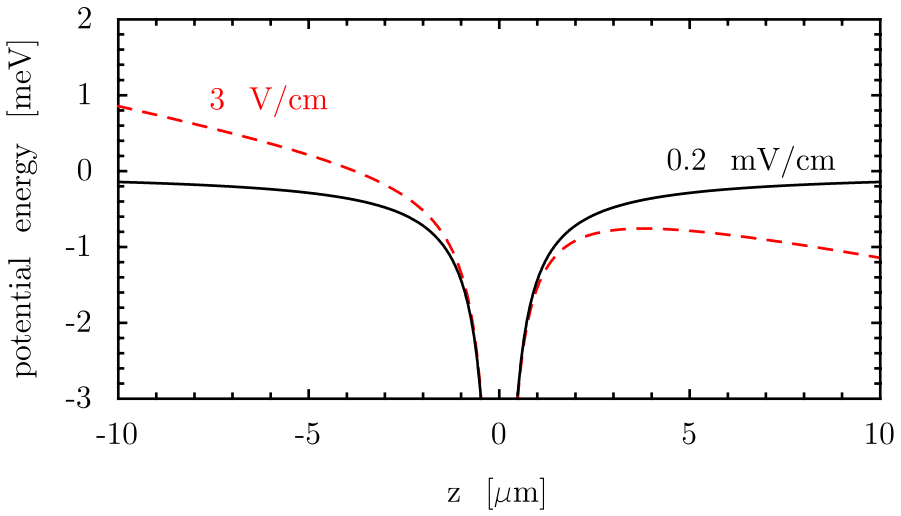

Figure 6-10: Electrostatic potential well from an antiproton with an external field of 3 V/cm and 0.2 V/cm

6.2.1 Pulse transfer of electrons and positrons

Because pulsed field recombination relies on the accurate timing and positioning of particles, experiments were carried out with electrons to show that the needed accuracy could be achieved. The goal was to pulse electrons from one electrode, bounce them off a repulsive electric field and then recatch them on their return. The electrons are originally trapped using an offset well which requires only one voltage pulse to release the particles. Once the trapping field is pulsed down (shown in Fig. 6-12 as a dotted line), the particles travel along the trap axis towards the far end of the trap. As they approach the electrodes biased to stop the particles, the electrons return back towards their original location. By changing the pulse duration the particles can be seen to execute from 0 to 3 trips as shown in Fig. 6-13. Special care had to be taken in the implementation of this experiment as pulse rise and fall times must be kept short compared to the particle travel time. Typical values seen for pulse rise and fall times range from 5 to 10 ns when measured at the 4 K electrical feedthroughs close to the electrodes.

As the electron pulsing experiments were successful, the next step towards pulsed field recombination was tried. This experiment involved the pulsing, stopping, and catching of positrons. The technique used was similar to that of the electron pulsing experiments except that the particles were caught after a single pass. A drawing of the various steps can be seen in Fig. 6-14. As the particles round trip time had already been verified with electrons the experiment was attempted with a pulse duration of 90 ns. Up to 3.3×10^5 positrons were pulsed from the T2 offset well and caught on the T8 electrode with 100% efficiency.

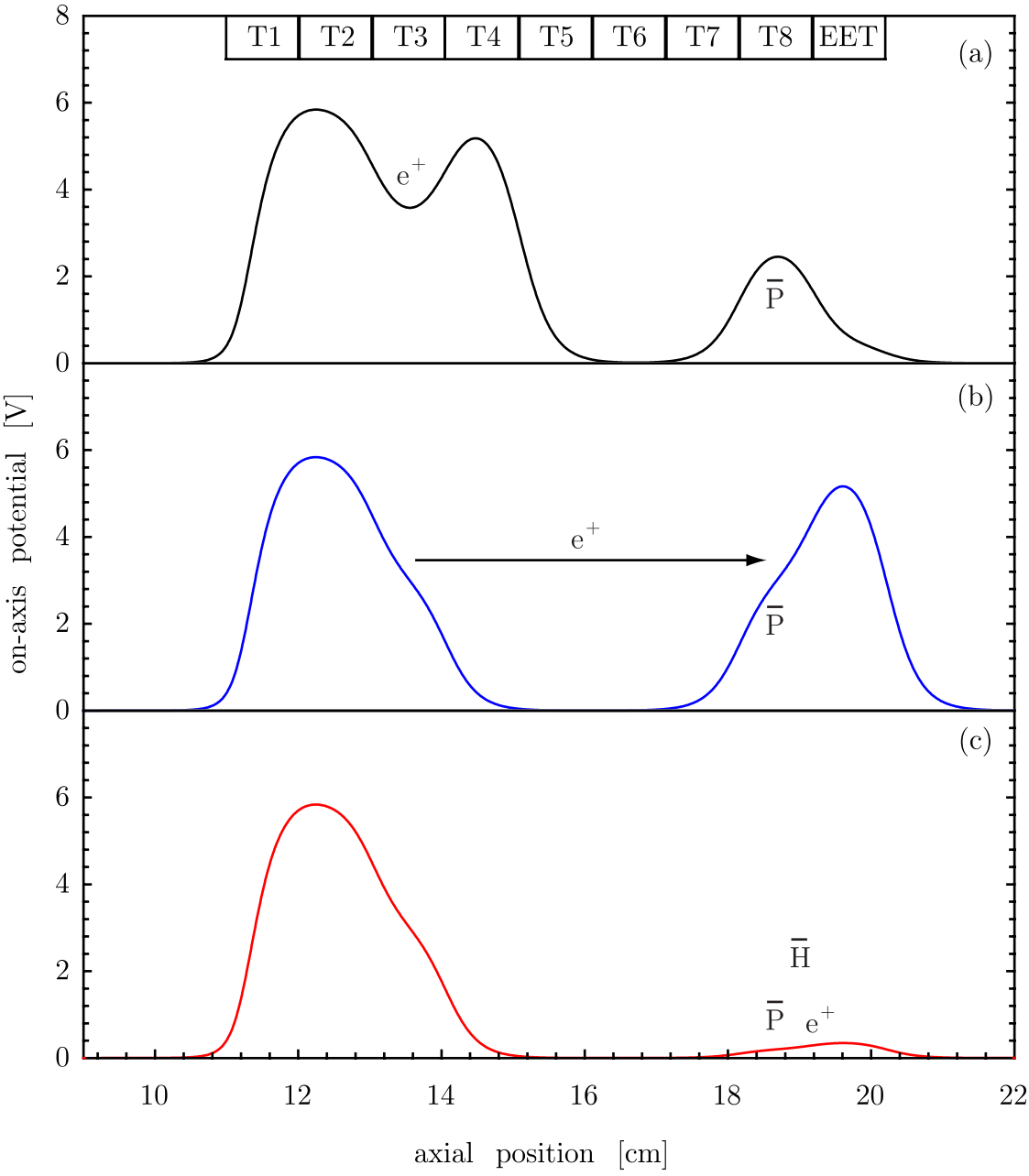

Figure 6-11: Pulse field recombination of positrons and antiprotons into antihydrogen. Initially the particles are contained in separate spaces (a). The positrons are allowed to escape from their trap as the right side of the trap is pulsed open. At the same time, the antiproton well is pulsed into a configuration to stop the incoming positrons (b). As the positrons enter the antiproton cloud, they are slowed by the electric field. During the turn around time of the positrons, the electric field is pulsed down allowing the particles which have come close enough together to remain bound (c). A small electric field is kept in the recombination region to push the charged particles away.

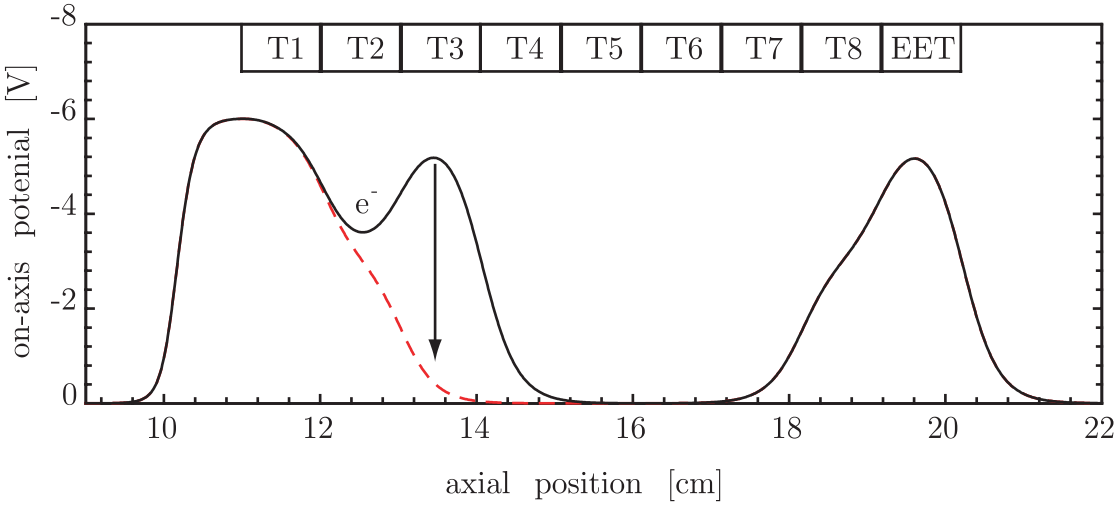

Figure 6-12: Plot of the voltage along the axis of the Penning trap for electron pulsing experiments

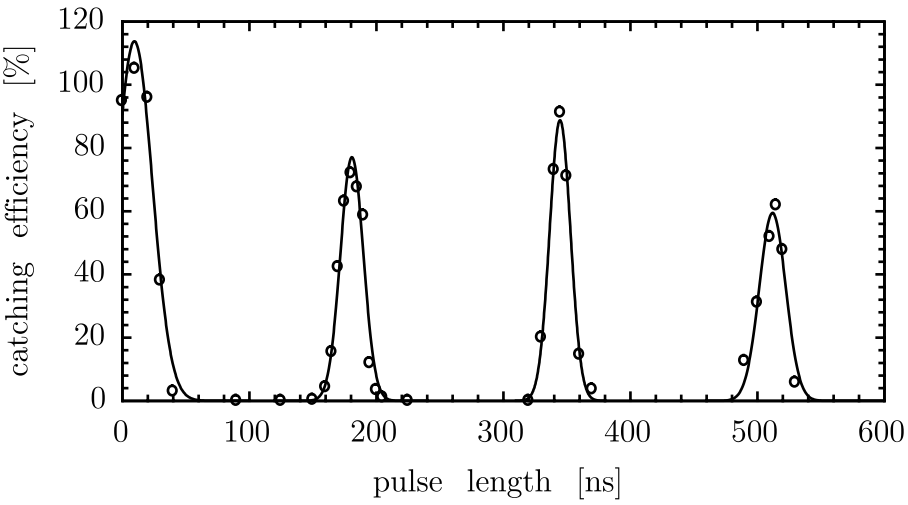

Figure 6-13: Plot of the capturing efficiency of electrons as a function of the release/capture pulse length

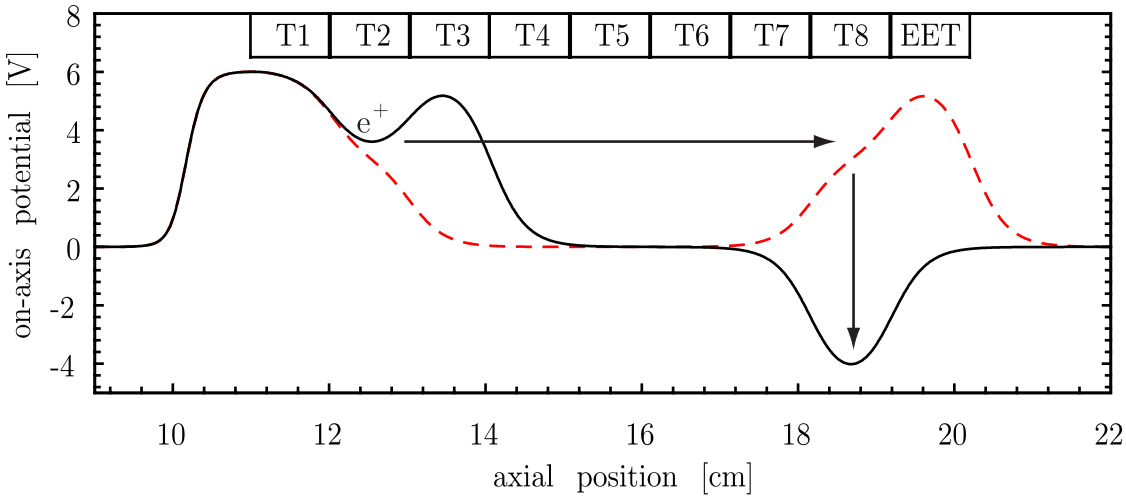

Figure 6-14: Plot of the electrostatic potential used for pulsing, stopping, and catching positrons

6.2.2 Antiprotons pulsed into a nearly field free region

As the positron techniques had been shown to work, the last remaining step towards pulsed field recombination of antihydrogen was the manipulation of antiprotons. This step involves the pulsing of the trapping potential used to confine the antiprotons (seen in Fig. 6-11.) Once the antiprotons are placed in a single electrode well, the electrode and an adjoining one are pulsed up to create an electric field that can stop positrons pulsed out of a elevated potential well. This nominal 3 V/cm electric field does accelerate the antiprotons, but as the time needed to stop the positrons is short compared to the time needed to move the much more massive antiprotons, the antiprotons do not move appreciably during this sequence. Once the positrons are stopped, the 3 V/cm field is brought down to 200 mV/cm which acts to separate charged particles from the recombination region. During this antiproton manipulation, all the antiprotons left the trap after about 3μs. An analog detector signal of this escape can be seen in Fig. 6-15.

One hypothesis for the antiproton loss is the axial exit of the particles. Antiprotons in the initial trap well have axial oscillation frequencies below 1 MHz or periods longer than 1 μs. Pulses applied to the antiprotons which are quick compared to this time scale will not change their kinetic energies. As the pulsing which is used for pulse field recombination have rise and fall times below 10 ns, the antiprotons should not be axially heated. Given an exit time of 3 μs, the antiprotons must have a kinetic energy of over 5 eV before pulsing. As this has not been seen in other energy analysis of the antiprotons, axial escape seems improbable.

Another possible channel for antiproton loss would be radial expansion as the particles are pulsed into a longer well. The long well that antiprotons are injected into has a long electric field free region. As the particles sample this region they

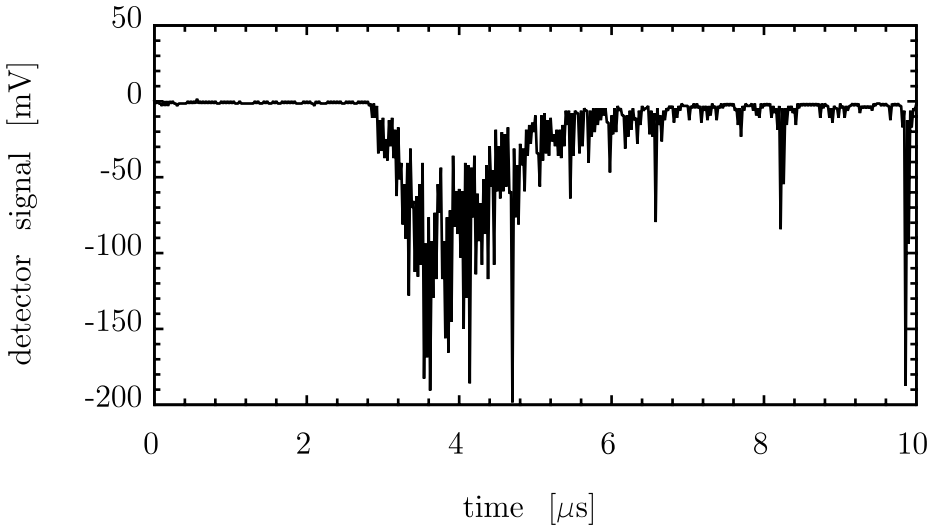

Figure 6-15: Analog detector signal of antiproton annihilations during studies of pulsed-field recombination

probe the trap imperfections, either mechanical or electrical. It is thought that as the particle energies are of the same order as the energy perturbations caused by the imperfections that instabilities will occur.

In order to inhibit the loss of antiprotons slight variations on the pulsed field recombination scheme were tried. One of the first ideas was to place voltage barriers around the antiproton region. These barriers would not interfere with the initial recombination area but would help to keep the antiprotons from leaking out radially by providing an electric field. This scheme can be seen in Fig. 6-16. With these barriers 50% of the initial antiprotons were kept in the trap. Because of the excessive loss, trying to detect antihydrogen with this sequence would be extremely difficult. Nevertheless, positrons were combined with antiprotons in a slightly modified way (see Fig. 6-17.) Both of these experiments did not show massive fast losses (which are detected on an analog channel of the annihilation particle detectors) but using positrons our yield of antiprotons kept in the long well was reduced to 25%. Although this was different than expected, the difficulty of detecting antihydrogen with this background loss made this scheme unworkable so far.

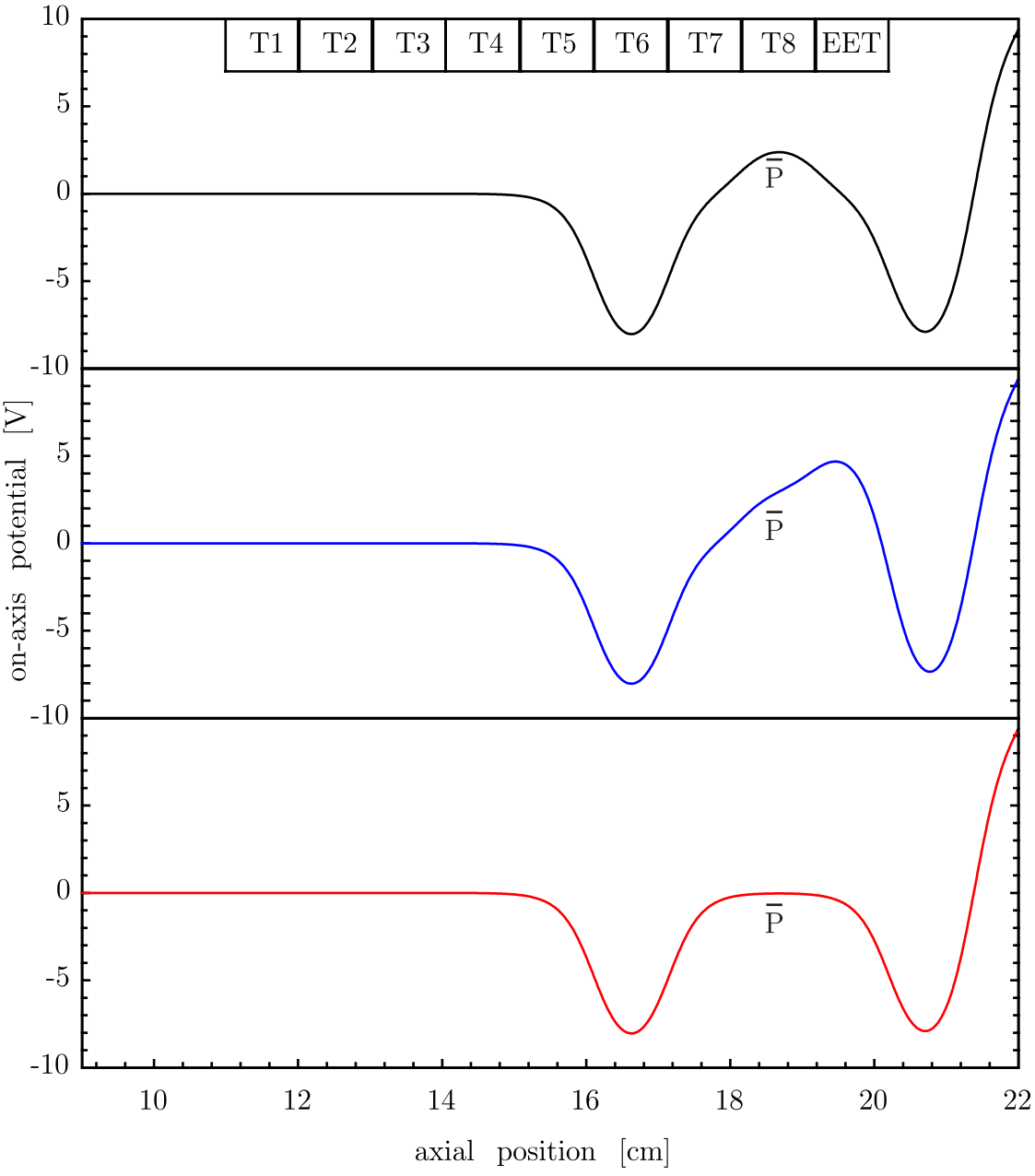

Figure 6-16: Test of antiproton release with low axial energy in three electrode well

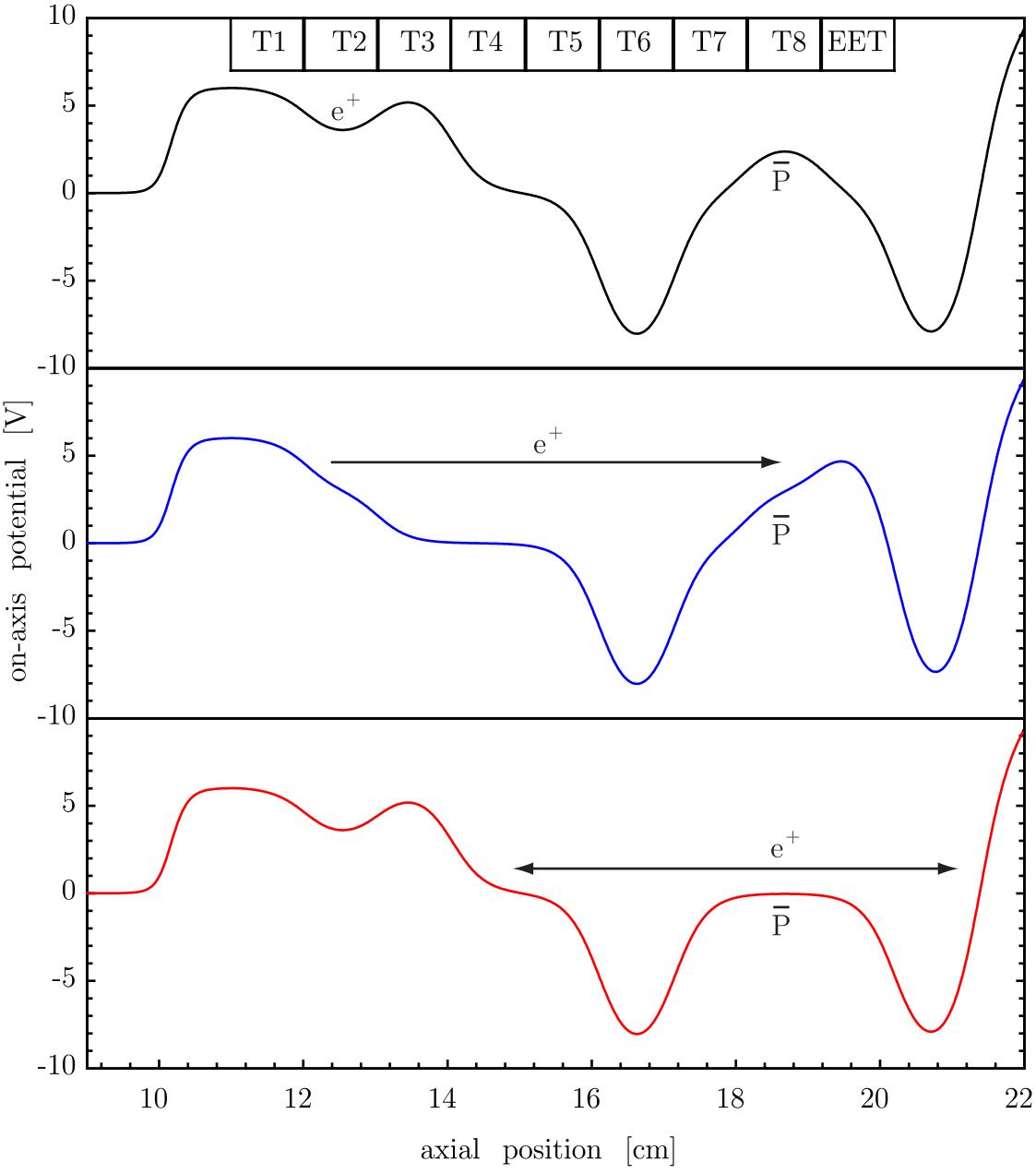

Figure 6-17: Test of low energy antiproton release into three electrode well with positrons

Chapter 7

Conclusions

This work has presented the progress made in accumulating and manipulating the ingredients of cold antihydrogen. We presented and explained a new technique for positron accumulation, simultaneously accumulated cold positrons and antiprotons at the new AD facility, and made these particles interact at low temperatures.

A new positron accumulation technique, compatible with extreme-high vacuum and cryogenic temperatures, has been described and demonstrated [1]. This mechanism is orders of magnitude more efficient than previous methods. Positrons emitted from a radioactive source are passed through a tungsten crystal. Positronium is formed as positrons, moderated by the tungsten crystal, exit the moderator in a high magnetic field accompanied by a secondary electron. This highly-excited positronium is ionized by the electric field of a trapping well. This technique can be used to accumulate symmetric numbers of positrons or electrons.

We have incorporated dual tungsten crystals to increase positron accumulation rates by 250%. The second crystal, used as a moderator, supplies slow positrons for positronium production. Additionally, this second moderator has allowed us to study the energy distribution of the moderated positron beam. A new 150 mCi ^{22}Na source has been installed, increasing positron loading rates. The maximum rate observed is $1.4 \times 10^4\, e^+\mathrm{h}^{-1}\mathrm{mCi}^{-1}$.

In the first interaction of cold antiprotons and positrons [2], the introduction of the antiproton beam into the Penning trap arrested the positron loading mechanism. The understanding of this effect, the removal of a gas layer on the positronium production surface, along with the preventive measures taken (the addition of a valve to block the antiproton beam) have allowed us to demonstrate the simultaneous accumulation of cold positrons and antiprotons.

Because of new demands including a rotary electrode, fiber detector, additional positron moderator, and larger radioactive source, a completely new Penning trap and support apparatus had to be built. This system has been shown to be robust in capturing electrons, positrons and antiprotons over the two years it has been in use.

The antiproton experiments done with the new apparatus at the new AD facility include the capture, cooling, and stacking of antiprotons. The antiprotons are ejected from the AD at 5 MeV, passed through an energy degrader and then cooled down to sub-eV energies via collisions with cold (4.2 K) electrons.

Combining cold antiprotons and positrons, we have started investigating two recombination techniques. These methods, three-body recombination and pulsed-field recombination, have promise for the eventual production of cold antihydrogen. Investigations of antiprotons and positrons, in a configuration compatible with three-body recombination, have resulted in the first positrons cooling of antiprotons [7].

The future direction of antihydrogen will probably concentrate on understanding the interaction between antiprotons and positrons. This includes particle cloud size and density, interaction rates, and antihydrogen detection schemes. As predicted rates are high and we have not encountered fundamental limitaions in combining the particles together, future work should be well placed for the production of cold antihydrogen.

Appendix A

Positron trap wiring diagrams

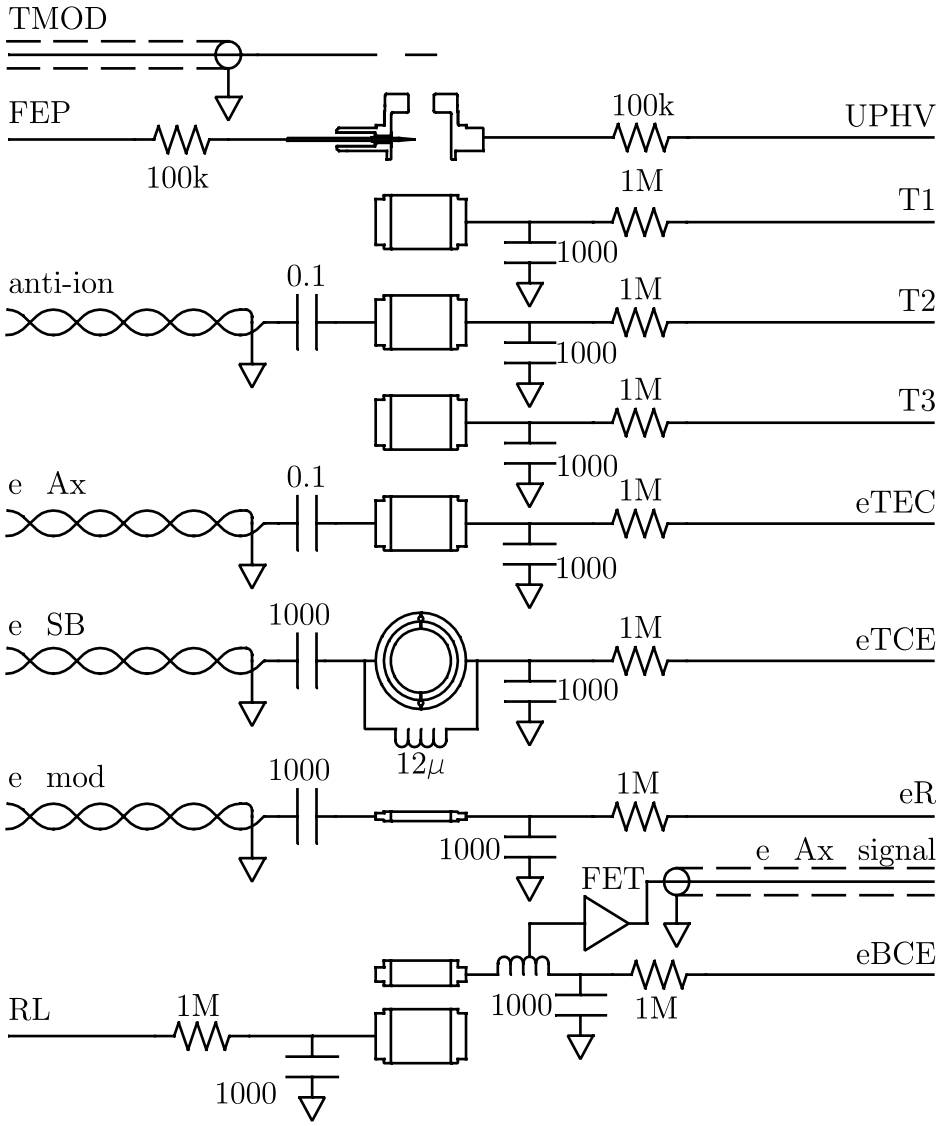

Figure A-1: Positron trap wiring (1/2)

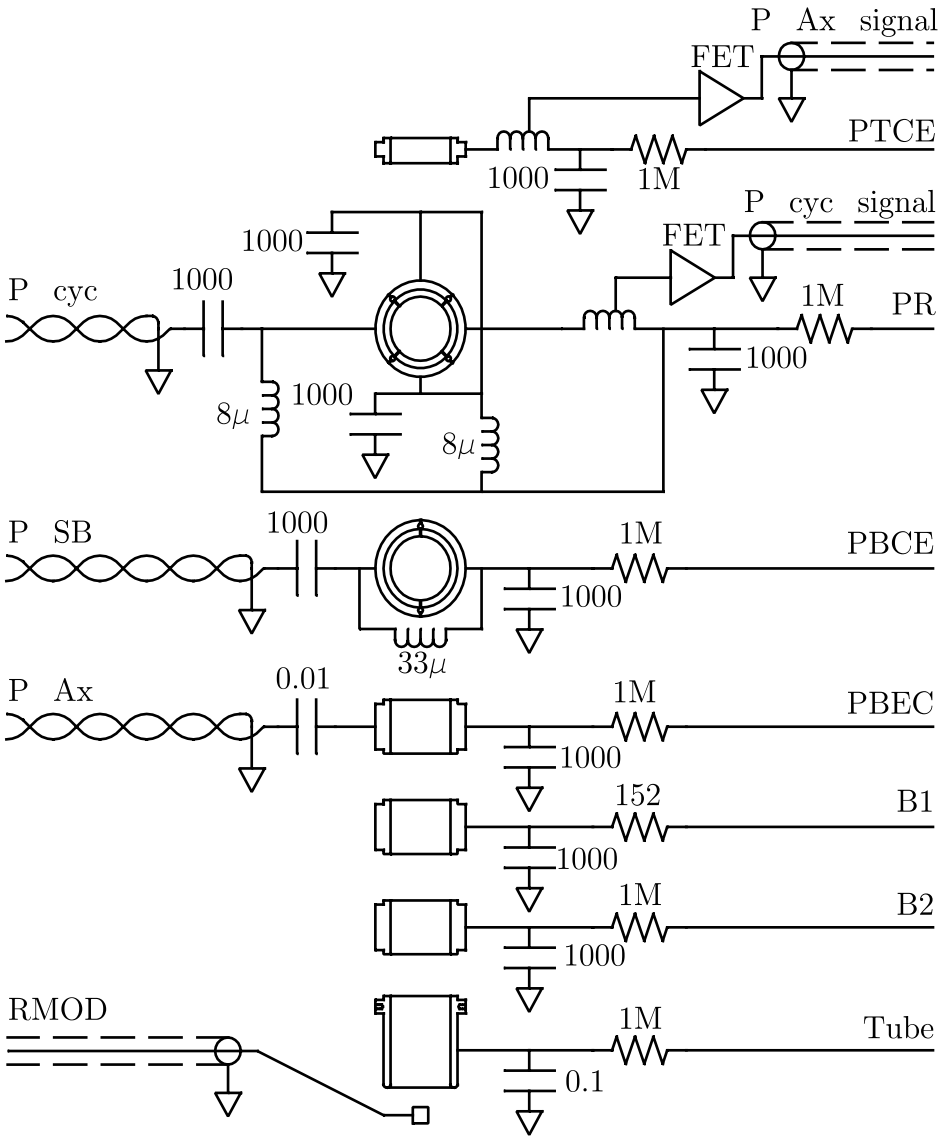

Figure A-2: Positron trap wiring (2/2)

Appendix B

Antihydrogen trap wiring diagrams

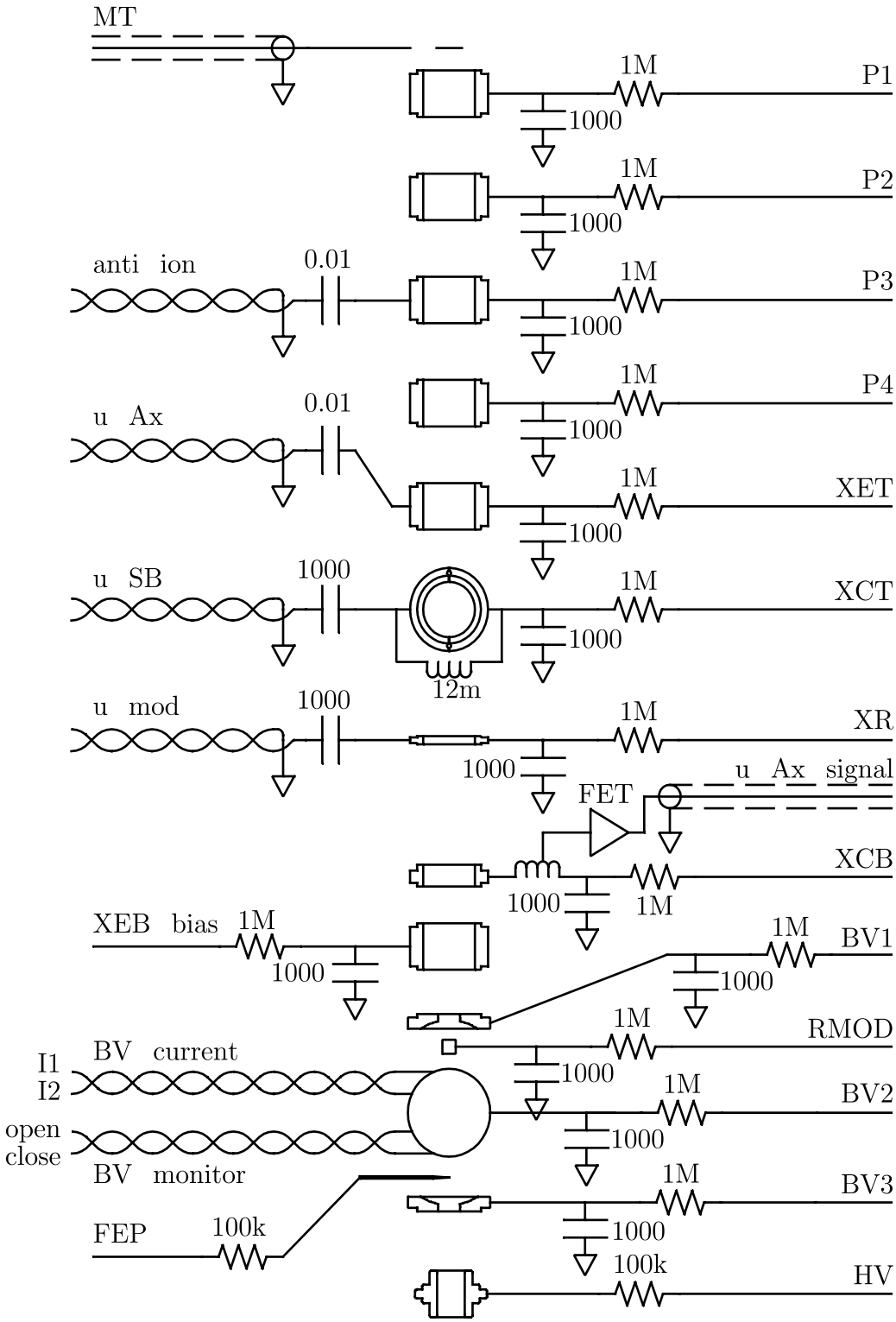

Figure B-1: Antihydrogen trap wiring (1/4)

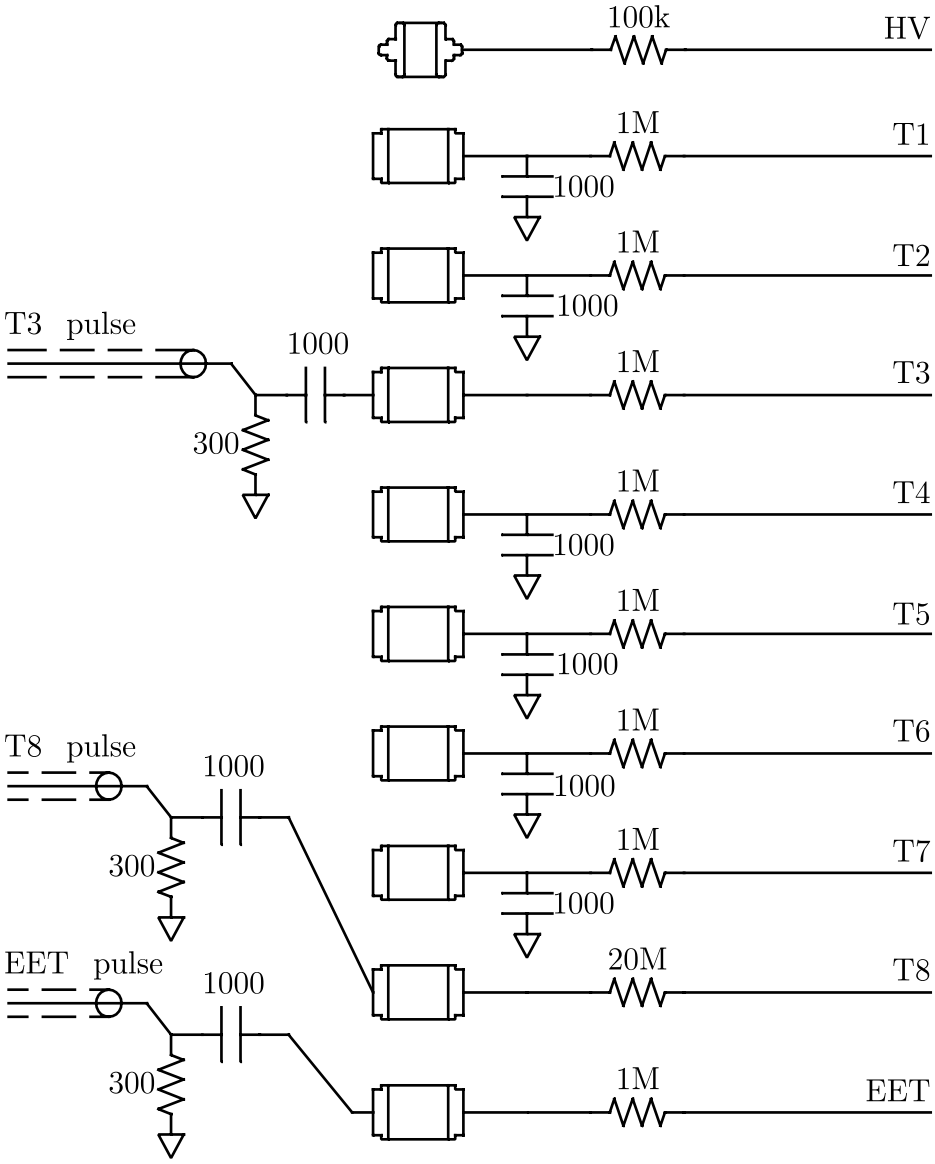

Figure B-2: Antihydrogen trap wiring (2/4)

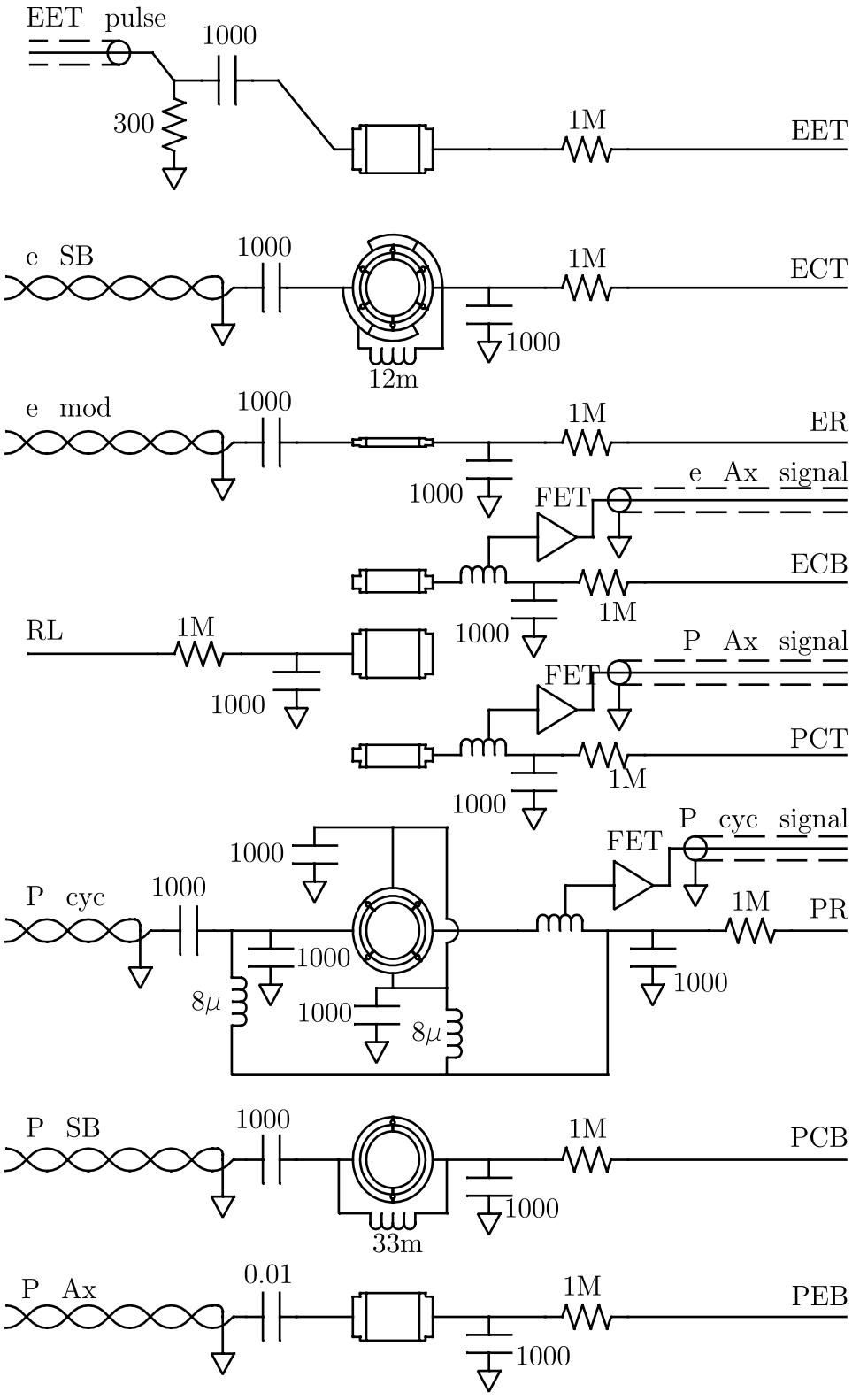

Figure B-3: Antihydrogen trap wiring (3/4)

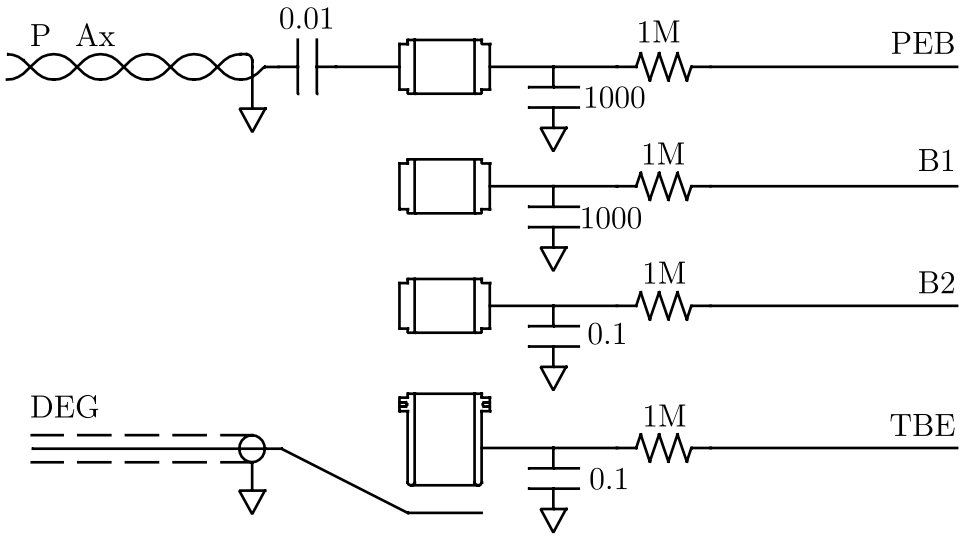

Figure B-4: Antihydrogen trap wiring (4/4)

Bibliography

[1] J. Estrada, T. Roach, J.N. Tan, P. Yesley, and G. Gabrielse. Field ionization of strongly magnetized rydberg positronium: A new physical mechanism for positron accumulation. *Phys. Rev. Lett.*, 84:859, 2000.

[2] G. Gabrielse, D. S. Hall, T. Roach, P. Yesley, A. Khabbaz, J. Estrada, C. Heimann, and H. Kalinowsky. The ingredients of cold antihydrogen: Simultaneous confinement of antiprotons and positrons at 4 k. *Phys. Lett.*, B 455:311–315, 1999.

[3] G. Gabrielse, X. Fei, L. Haarsma, S. L. Rolston, R. Tjoelker, T. A. Trainor, H. Kalinowsky, J. Haas, and W. Kells. First capture of antiprotons in an ion trap: Progress toward a precision mass measurement and antihydrogen. *Phys. Scr. T*, 22:36–40, 1988.

[4] S. L. Rolston and G. Gabrielse. Cooling antprotons in an ion trap. *Hyperfine Interact.*, 44:233–245, 1988.

[5] G. Gabrielse, X. Fei, L. A. Orozco, R. L. Tjoelker, J. Haas, H. Kalinowsky, T. A. Trainor, and W. Kells. Cooling and slowing of trapped antiprotons below 100 meV. *Phys. Rev. Lett.*, 63:1360–1363, 1989.

[6] Peter Spoor Yesley. *The Road to Antihydrogen.* PhD thesis, Harvard University, 2001.

[7] G. Gabrielse, J. Estrada, J.N. Tan, P. Yesley, N.S. Bowden, P. Oxley, T. Roach, C.H. Storry, M. Wessels, J. Tan, D. Grzonka, W. Oelert, G. Schepers, T. Sefzick, W.H. Breunlich, M. Cargnelli, H. Fuhrmann, R. King, R. Ursin, J. Zmeskal, H. Kalinowsky, C. Wesdorp, J. Walz, K.S.E. Eikema, and T.W. Hansch. First positron cooling of antiprotons. *Phys. Lett. B*, 507:1, 2001.

[8] J. Stevefelt, J. Boulmer, and J-F. Delpech. Collisional-radiative recombination in cold plasmas. *Phys. Rev.*, A 12:1246–1251, 1975.

[9] G. Gabrielse, S. L. Rolston, L. Haarsma, and W. Kells. Antihydrogen production using trapped plasmas. *Phys. Lett. A*, 129:38–42, 1988.

[10] M. E. Glinsky and T. M. O'Neil. Guiding center atoms: Three-body recombination in a strongly magnetized plasma. *Phys. Fluids*, B 3:1279–1293, 1991.

[11] L. I. Men'shikov and P. O. Fedichev. Theory of elementary atomic processes in an ultracold plasma. *JETP*, 81:78–86, 1995.

[12] P. O. Fedichev. Formation of antihydrogen atoms in an ultra-cold positron-antiproton plasma. *Phys. Lett.*, A 226:289–292, 1997.

[13] C. Wesdorp, F. Robicheaux, and L. D. Noordam. Field-induced electron-ion recombination: A novel route towards neutral (anti-)matter. *Phys. Rev. Lett.*, 84:3799–3802, 2000.

[14] G. Baur, G. Boero, S. Brauksiepe, A. Buzzo, W. Eyrich, R. Geyer, D. Grzonka, J. Hauffe, K. Kilian, M. LoVetere, M. Macri, M. Moosburger, R. Nellen, W. Oelert, S. Passagio, A. Pozzo, K. Röhrich, K. Sachs, G. Schepers, T. Sefzick, R. S. Simon, R. Stratmann, F. Stinzing, and M. Wolke. Production of antihydrogen. *Phys. Lett. B*, 368:251–258, 1996.

[15] G. Blanford, D. C. Christian, K. Gollwitzer, M. Mandelkern, C. T. Munger, J. Schultz, and G. Zioulas. Observation of atomic antihydrogen. *Phys. Rev. Lett.*, 80:3037–3040, 1998.

[16] R. Bluhm, V. A. Kostelecký, and N. Russel. CPT and Lorentz tests in hydrogen and antihydrogen. *Phys. Rev. Lett.*, 82:2254–2257, 1999.

[17] G. Gabrielse. Trapped antihydrogen for spectroscopy and gravitation studies: Is it possible? *Hyperfine Interact.*, 44:349–356, 1988.

[18] T. D. Lee and C. N. Yang. Question of parity conservation in weak interactions. *Phys. Rev.*, 104:254–258, 1956.

[19] C. S. Wu, E. Ambler, R. W. Hayward, D. D. Hoppes, and R. P. Hudson. An experimental test of parity conservation in beta decay. *Phys. Rev.*, 105:1413–1415, 1957.

[20] L. D. Landau. On the conservation laws for weak interactions. *Nucl. Phys.*, 3:127–131, 1957.

[21] J. H. Christenson, J. W. Cronin, V. L. Fitch, and R. Turlay. Evidence for the 2π decay of the K_2^0 meson. *Phys. Rev. Lett.*, 13:138–140, 1964.

[22] T. W. Darling, F. Rossi, G. I. Opat, and G. F. Moorhead. The fall of charged particles under gravity: A study of experimental problems. *Rev. Mod. Phys.*, 64:237–257, 1992.

[23] G. Gabrielse, X. Fei, L. A. Orozco, R. L. Tjoelker, J. Haas, H. Kalinowsky, T. A. Trainor, and W. Kells. Thousandfold improvement in the measured antiproton mass. *Phys. Rev. Lett.*, 65:1317–1320, 1990.

[24] D. Wineland, P. Ekstrom, and H. Dehmelt. Monoelectron osciallator. *Phys. Rev. Lett.*, 31:1279–1282, 1973.

[25] Lowell S. Brown and G. Gabrielse. Geonium theory: Physics of a single electron or ion in a Penning trap. *Rev. Mod. Phys.*, 58:233–311, 1986.

[26] R. VanDyck, D. Wineland, P. A. Ekstrom, and H. Dehmelt. High mass resolution with a new variable anharmonicity penning trap. *Appl. Phys. Lett.*, 28:446–448, 1976.

[27] G. Gabrielse, L. Haarsma, and S. L. Rolston. Open-endcap Penning traps for high precision experiments. *Int. J. Mass Spectrom. Ion Processes*, 88:319–332, 1989.

[28] Gerald Gabrielse and F. Colin MacKintosh. Cylindrical Penning traps with orthogonalized anharmonicity compensation. *Int. J. Mass Spectrom. Ion Processes*, 57:1–17, 1984.

[29] Wolfgang K. H. Panofsky and Melba Phillips. *Classical Electricity and Magnetism*. Addison-Wesley, Reading, MA, 1956.

[30] H. G. Dehmelt. Entropy reduction by motional sideband excitation. *Nature*, 262:777, 1976.

[31] David Forest Phillips. *A Precision Comparison of the Antiproton-Proton Charge-to-Mass Ratios*. PhD thesis, Harvard University, 1996.

[32] David Sumner Hall. *Positrons, Antiprotons, and Interactions for Cold Antihydrogen*. PhD thesis, Harvard University, 1997.

[33] Jörn Adomeit. *Teilchendiskriminierung durch Energieverlustberechnung am Crystal-Barrel-Detektor*. PhD thesis, Institut für Experimentalphysik, 1996.

[34] L. H. Haarsma, K. Abdullah, and G. Gabrielse. Extremely cold positrons accumulated electronically in ultrahigh vacuum. *Phys. Rev. Lett.*, 75:806–809, 1995.

[35] W. N. Cottingham and D. A. Greenwood. *An Introduction to Nuclear Physics*. Cambridge, Cambridge, 2001.

[36] Loren Dean Haarsma. *Accumulating Positrons in an Ion Trap*. PhD thesis, Harvard University, 1994.

[37] R. G. Musket, W. McLean, C. A. Colmenares, D. M. Makowiecki, and W. J. Siekhaus. Preparation of atomically clean surfaces of selected elements: a review. *Appl. Surf. Sci.*, 10:143–207, 1982.

[38] S. Maury. The antiproton decelerator: AD. In *CERN Report No. CERN/PS/96-17/AR (unpublished)*, 1996.

[39] P. Belochitskii, J. Bosser, J. Buttkus, C. Carli, F. Caspers, V. Chohan, D. Cornuet, T. Eriksson, A. Findlay, M. Giovannozzi, B. Holzer, R. Maccaferri, N. Madsen, M. Marchesotti, S. Maury, D. Möhl, S. Pasinelli, F. Pedersen, L. Søby,

J. Tan, and G. Tranquille. Commissioning and first operation of the antiproton decelerator (AD). In *CERN Report No. CERN/PS/2001-047/AE (unpublished)*, 2001.

[40] D. Grzonka. Atrap beam preparation. Unpublished.

[41] G. Gabrielse, X. Fei, L. A. Orzco, S. L. Rolston, R. L. Tjoelker, T. A. Trainor, J. Haas, H. Kalinowsky, and W. Kells. Barkas effect observed with antiprotons and protons. *Phys. Rev. A*, 40:481–484, 1989.

[42] C. Wesdorp, F. Robicheaux, and L. D. Noordam. Field-induced eletron-ion recombination, a novel route towards neutral (anti-)matter. *Phys. Rev. Lett.*, 84:3799, 2000.